

Hydrodynamic modeling of electron transport in silicon quantum wires



Tina Castiglione

Università degli Studi di Napoli Federico II
sede consorziata con
Università degli Studi di Catania

Dottorato di ricerca in Scienze Computazionali e Informatiche
XXVIII Ciclo
Tesi di Dottorato di Ricerca

TUTOR: Prof. Orazio Muscato

COORDINATORE:
Prof.ssa Gioconda Moscariello

Acknowledgements

I would like to express my sincere gratitude to my advisor, Professor Orazio Muscato, for his full and generous support on my research work throughout my Ph.D. study. Without his guidance over the last three years, this thesis would not have been possible.

I want to thank my Ph.D. colleagues for sharing this doctorate experience encouraging each other at the most difficult times.

I am grateful to my mother, my father, my sister and my brother-in-law for supporting me in every situation and for their encouragement. To them, I dedicate this thesis.

Table of contents

List of figures	v
List of Symbols	viii
1 Introduction	1
1.1 Nanostructures and nanodevices	3
1.2 Low-dimensional systems	4
1.3 Quantum wires	6
1.4 Properties of Silicon	8
1.5 Electronic band structure in SiNW	11
2 The Schrödinger effective mass equation	13
2.1 Quantum confinement	13
2.2 Infinitely deep rectangular wires	16
2.3 Finite rectangular wire	17
2.3.1 Finite difference scheme for the EMA	18
2.3.2 Solution of the EMA with a variational method	22
2.4 Results for the EMA equation	23
3 Carrier scattering	26
3.1 Introduction	26
3.2 The Electron-Phonon interaction	27
3.2.1 Non-polar Optical Phonons Scattering	29
3.2.2 Acoustic Phonon Scattering	32
3.3 Scattering with impurities	33
3.4 Surface roughness scattering	34
4 Transport model for SiNW	37
4.1 Kinetic transport equations	37

4.2	The Extended Hydrodynamic model	39
4.3	Maximum Entropy Principle	42
4.4	Closure relations for the production terms	44
5	Electron transport in infinitely deep SiNW having different cross-sections	52
5.1	Introduction	52
5.2	Simulation results for triangular and square SiNW	53
5.2.1	Applications to the case of bulk silicon	61
5.3	Electron mobility	63
6	Self-consistent Schrödinger-Poisson-hydrodynamic solver for SiNW transistors	68
6.1	Computational method	69
6.1.1	Iteration scheme	71
6.2	Ballistic transport	73
6.2.1	Simulation of a triple-gate SiNW transistor	75
6.3	Simulation of a GAA-SiNW Transistor	76
6.3.1	Low-field mobility	83
7	Conclusions	86
	Appendix A Evaluation of the transition rate	88
	Appendix B 3D Poisson Solver	91
	References	94

List of figures

1.1	Schematic of a generic nanoelectronic device consisting of source and drain contacts with a <i>gate</i> which controls the transfer characteristics of the active region.	4
1.2	Density of states in low-dimensional systems (quantum well, quantum wire and quantum dot respectively), compared with the 3D case (dashed lines).	5
1.3	Two different realizations of quantum wires by etching. Illustration from [1].	7
1.4	Diamond (left) and zinc-blende (right) structures.	8
1.5	Brillouin zone of the face centered cubic lattice with indication of the points and lines of high symmetry. The irreducible wedge is the polyhedron with vertices Γ , K, W, X, U, L.	9
1.6	Energy band structure of silicon.	10
1.7	Constant energy surface of the six valleys of the lowest conduction band in silicon.	10
1.8	Schematic view of a SiNW. Electron transport is assumed to be one-dimensional in the x -direction.	11
1.9	SiNW band structure calculated from the empirical tight-binding model ([11]).	12
2.1	The infinitely deep rectangular cross-section quantum wire.	16
2.2	The rectangular cross-section quantum wire with finite barriers.	18
2.3	The two-dimensional mesh for the finite difference approach to the quantum wire.	19
2.4	The subband energies ε_v , eq. (2.4) obtained with a finite difference solver, with N_g grid points in each axes.	24
2.5	The percentage error between the subband energies ε_v (2.4) obtained with a finite difference solver and the Variational Method.	24
2.6	Eigenfunctions obtained with a finite difference solver, with $N_1 = N_2 = 41$ mesh point.	25

3.1	Schematic illustrations of the atomic displacements in (a) longitudinal acoustic (LA) and (b) transverse acoustic (TA) phonon modes.	28
3.2	Schematic illustrations of the atomic displacements in (a) longitudinal optic (LO) and (b) transverse acoustic (TO) phonon modes.	28
3.3	Classification of electron-phonon transitions in silicon: intra and inter valley scattering (f-and g-type).	30
3.4	Schematic representation of the surface roughness function, including the rms height and autocovariance length.	36
5.1	Sketch of the oxidation process. The oxide is slowly removed and the triangular section can be further reduced in a controllable way.	53
5.2	55
5.3	The lowest four confinement energies for the square and equilateral triangle cross-sections.	55
5.4	The subband linear densities ρ^v and the total linear density (5.60) versus the simulation time, for an electric field of 10 kV/cm, and equilateral triangle cross-section.	63
5.5	Velocity versus time for some values of the electric field, with $L_x = L_y = 10$ nm.	63
5.6	Electron energy versus time for some values of the electric field, with $L_x = L_y = 10$ nm.	64
5.7	Electron energy-flux versus time for some values of the electric field, with $L_x = L_y = 10$ nm.	64
5.8	The asymptotic value of the average velocity $\langle V(\infty) \rangle$ (5.64) versus the electric field for the square and the equilateral triangle cross-sections.	66
5.9	The bulk mobility (5.65) versus the electric field for the square cross-section, and the mobility evaluated using the Caughey-Thomas formula (5.66).	67
5.10	The bulk mobility (5.65) versus the electric field for the equilateral triangle cross-section, and the mobility evaluated using the Caughey-Thomas formula (5.66).	67
6.1	Cross sections of a rectangular nanowire (left) and a rectangular nanowire transistor (right).	70
6.2	Flowchart of the self-consistent SP solver.	71
6.3	The current (6.17) versus the gate voltage V_{GS}	76
6.4	Cross sections of a Gate-All-Around SiNW transistor.	79

6.5	Charge density and total potential along the cross-section at $x = 48$ nm and $z = 0$ nm, under a 1V gate bias.	81
6.6	Electron density across the nanowire at $x = 48$ nm. When the gate bias value increase, the onset of volume inversion is evident. The drain-source voltage is fixed at $V_{DS} = 0.012$ V.	81
6.7	Linear density for the A and B valleys versus the simulation time.	82
6.8	The mean velocity and energy versus the simulation time, obtained with and without SRS mechanism.	83
6.9	The mean energy flux versus the simulation time, obtained with and without Surface Roughness Scattering mechanism.	83
6.10	Low-field mobility versus gate voltage, obtained with/without Surface Roughness Scattering mechanism.	85

List of Symbols

$D(E)$	one-dimensional density of states
D_0	zero-order deformation potential
D_1	first-order deformation potential
D_{ac}	acoustic deformation potential
D_{iv}	intervalley deformation potential
$E(\mathbf{k})$	kinetic energy as function of the wave vector
$E[\varphi], E_i^\mu, E(\psi), E_{vx}$	total energy
E^{eff}	effective field
E_{FS}, E_{FD}	source and drain Fermi levels
E_F	Fermi energy
E_c	energy at the conduction band minimum
E_g	band gap energy
E_x, E_y, E_z	components of electric field
F_i^μ, F^v	flux of electron energy flux
$G_{ll'}^{\mu\mu'}, G^{vv'}$	overlap factor
H	Hamiltonian
H_p	perturbation potential
I	current

K_q	deformation potential
$K(x)$	modified Bessel function
L	length of the triangle side
L_x, L_y, L_z	lengths of the device
M	sparse matrix
$N(k)$	number of states
N_A	acceptor density
N_D	donor density
S	mean energy flux
S_e	entropy density
S_i^μ, S^v	linear electron energy flux
$T(E)$	transmission coefficient
T_1, T_2	triangular domain
T_L	lattice temperature
$U(y, z)$	confining potential
U^v, R^v, G^v	higher-order fluxes
$V, \langle V \rangle$	mean velocity
V_{DS}	$V_D - V_S$
V_D, V_S, V_G	drain, source and gate voltage
V_c	crystal volume
V_i^μ, V^v	linear electron velocity
V_{tot}	total potential
W	mean energy
W_i^μ, W^v	linear electron energy

Z_0, Z_{iv}	number equivalent valleys
Δ_2	primed valley
Δ_4	unprimed valley
Δ_{sr}	rms height
ϵ_0	permittivity of the free space
ϵ_r	relative permittivity
α	non-parabolicity parameter of the kinetic energy
\mathbf{k}	electron wave vector
\mathbf{q}	phonon wave vector
$\chi, \chi_l^\mu(y, z), \chi_{lx}^\mu(y, z)$	normed transversal part of the wave function
$\chi_{p,q}$	eigenfunctions of triangular QWR
ϵ_s	static dielectric constant
\hat{f}, \hat{f}_v	maximum entropy distribution
\hbar	Planck's constant/ 2π
$\hbar\omega(\mathbf{q})$	phonon energy
λ_A	Lagrange multipliers
λ_{sr}	correlation length
\mathcal{C}_η	collision term of the η -th scattering
$\mathcal{C}_p, \mathcal{C}_V, \mathcal{C}_W, \mathcal{C}_S$	moments of the collision term
$\mathcal{E}, \mathcal{E}_x$	kinetic energy as function of the wave vector
$\mathcal{F}_{ll'}^{\mu\mu'}$	average surface field
\mathcal{H}	matrix Hamiltonian
μ	valley index
$\mu(E_x)$	electron mobility

μ^A, μ^B	valley mobility
μ^V	subband mobility
μ_0	low field bulk mobility
μ_C	Caughey-Thomas mobility
μ_E	chemical potential
μ_{low}	low-field mobility
$\omega(\mathbf{q}), \omega_{ac}, \omega_{op}, \omega_0$	phonon angular velocity
$\psi(x, y, z)$	normed electron wave function
ρ	mass density
$\rho^{1D}(E), \rho^{2D}(E), \rho^{3D}(E)$	density of states
ρ^A, ρ^B	total linear density for A and B valleys
ρ_μ^l, ρ^v	linear electron density
ρ_{tot}	total linear density
$\varepsilon, \varepsilon_{lx}^\mu, \varepsilon_v$	energy eigenvalue
$\varepsilon_A^0, \varepsilon_B^0$	A-B valley energy minimum
$\varepsilon_{p,q}$	energy eigenvalues of triangular QWR
φ	electrostatic potential
$\vec{M}_l^\mu, M_A(\mu, l)$	moment of the MBTE
$\vec{\Psi}_A(\mathbf{k})$	weight function
a_0	lattice parameter
e	electron charge
f, f_μ^l	electron distribution function
$f_M^v, f_v^{(eq)}, f_l^{\mu(eq)}$	Maxwellian distribution

$g(\mathbf{q})$	phonon distribution function
g_0	Bose-Einstein distribution
k_B	Boltzmann constant
k_x, k_y	electron wave vector components
l, ν	subband index
m^*	effective electron mass
$m_{\Delta_2}^*, m_B^*$	effective mass primed valley
$m_{\Delta_4}^*, m_A^*$	effective mass unprimed valley
m_{μ}^*	effective mass of the μ -th valley
m_e	electron mass
$n, n[\varphi]$	three-dimensional electron density
n_y, n_z	integer values (quantum numbers)
v_{μ}, v_x	electron group velocity
v_s	sound velocity
$w(\mathbf{k}, \mathbf{k}'), w_{\eta}$	transition rate

Acronyms / Abbreviations

SiO ₂	Silicon dioxide
0DEG	Zero-dimensional electron gas
1DEG	One-dimensional electron gas
2DEG	Two-dimensional electron gas
BTE	Boltzmann Transport Equation
BZ	Brillouin zone
CAD	Computer Aided Design
CMOS	Complementary metal-oxide-semiconductor

EMA	Effective Mass Approximation
FET	Field-Effect Transistor
FinFET	Fin Field Effect Transistor
GAA SNWT	Gate-All-Around SNWT
MBTE	Multisubband Boltzmann Transport Equation
MC	Monte Carlo model
MEP	Maximum Entropy Principle
MOSFET	Metal-oxide-semiconductor field-effect transistor
NEGF	Non-Equilibrium Green's Function
QW	Quantum well
QWR	Quantum wire
SiNW	Silicon Nanowire
Si	Silicon
SNWT	Silicon Nanowire Transistor
SP	Schrödinger-Poisson system
SRS	Surface Roughness Scattering
TB	Tight-binding method
VLS	Vapor-liquid-solid method

Chapter 1

Introduction

The study of carrier transport in semiconductor devices is of great interest for the design of modern electron devices. In order to describe charges transport phenomena, Monte Carlo or deterministic solver of the Boltzmann Transport equation (BTE) are widely applied, but they are very expensive, from a computational point of view, for Computer Aided Design (CAD) purposes. In engineering applications simpler models are routinely used. Consequently it can be convenient to substitute the BTE with macroscopic models like drift-diffusion or energy-transport ones. They give a less detailed description of the system, which is however adequate to describe the more relevant properties of transport phenomena.

However, for devices with nanometric dimensions they are not more valid because high electric field and high field-gradient conditions in the active region of the device drive the system out of local thermal equilibrium.

In order to provide a description of such non equilibrium effects without the overhead of large computational costs, hydrodynamic models can be used. They represent a good engineered-oriented approach to simulate submicron devices. These models are derived from the infinite hierarchy of the moment equations of the Boltzmann transport equation using a suitable truncation procedure. As a consequence, the so called *closure problem*, arises. A good, physically motivated way to obtain closure relations is by means of the Maximum Entropy Principle (MEP). It allows to close the system of balance equations arising as moment equations of the BTE. In fact, it gives a form of the distribution functions that makes the best use of the knowledge of a finite number of moments. These new functions correspond to the extremum of the total entropy density of the system, under the constraints that the moments of the new distribution functions, relative to the weight functions used to obtain the moment equations, are equal to the known moments. The advantage of this method is that such obtained model is free of any fitting parameters.

In this work a hydrodynamic modeling of electron transport in silicon quantum wires (QWR) is presented. In particular, hydrodynamic-like equations are derived to describe the non-equilibrium transport of electrons in quantum wire devices. This transport model includes necessarily the effective mass Schrödinger equation in the confining cross section and the three-dimensional Poisson equation, which have to be solved self-consistently.

The thesis is structured as follows. In **Chapter 1** an introduction to low-dimensional systems, with more focus on nanowires, is given. Additionally, a brief review to the fundamental elements of the silicon physics is presented, as well as the electronic band structure in silicon nanowire (SiNW), which is altered respect to the bulk silicon, is illustrated.

The **Chapter 2** is dedicated to a complete description of the quantum confinement in SiNW and to the solution of the 2-D Schrödinger equation, by using both a finite difference numerical scheme and a variational method.

Chapter 3 is concerned with quantum mechanical treatments of various scattering processes in SiNW: electron-phonon interaction, scattering with impurities and surface roughness scattering. The formulas for scattering rates are all derived starting from the Fermi's Golden Rule. In **Chapter 4** an extended hydrodynamic transport model for SiNW, by considering an appropriate electronic band structure presented in Chapter 1, is constructed starting from the BTE. Balance equations are obtained by choosing an 4-moments model and closure relations for the higher-order fluxes and the production terms (i.e the moments on the collisional operator) are obtained by using the maximum entropy distribution.

Chapter 5 focuses upon electron transport phenomena in infinitely deep SiNW having different cross-sections (rectangular and equilateral triangle). A non-parabolic approximation of the conduction band is used in order to setup the hydrodynamic model for the transport. Applications to the case of *bulk silicon* are presented. The drift velocity and the electron mobility are evaluated for square and equilateral triangle cross-sections of the wire.

Finally, the **Chapter 6** is devoted to simulation results for gated SiNW transistors. A detailed description of a self-consistent 3D Poisson-2D Schrödinger solver coupled with a hydrodynamic transport model, employed to model the electronic transport, is provided. By means of this coupled Poisson-Schrödinger-hydrodynamic solver the low-field mobility, which is one of the most important parameters for engineering applications, is computed.

In **Chapter 7** conclusions are drawn.

1.1 Nanostructures and nanodevices

In modern days, the increasing complexity of electronic systems is stimulating research in developing fabrication technologies for smaller and more efficient devices. Owing to the decrease of device dimensions, electrons are forced in spaces comparable with their wavelength and effects have begun to be investigated. This has also caused more interest in developing technologies for the realization of structures with dimensions in the nanometric range. In the last decades nanotechnologies made possible the production of innovative devices with promises of high density integration, for an exponential increasing of electronic systems complexity.

Nanostructures and nanotechnologies are reaching important breakthroughs in single molecule sensing and manipulation, with fundamental applications in biology and medicine. In particular, among these nanostructures, silicon nanowires are largely investigated for the central role assumed by Silicon in semiconductor industry.

The increasing miniaturisation of the devices caused that a new aspect attracted attention, the quantum mechanical discretisation. Consequently, there emerged in the recent years arising interest in the study of the charge transport in so-called low dimensional or mesoscopic systems. The reason for this was not only the advances in technology which made it possible to fabricate very small structures, but also the discovery of new molecules, like the nano-tubes. For this reason, the study of charge transport in semiconductors is of fundamental importance both from the point of view of basic physics and for its application to electronic devices. Historically, the term "semiconductor" has been used to denote solid materials whose conductivity is much larger than that of insulators but much smaller than that of metals, measured at room temperature. A modern and more precise definition is that a semiconductor is a solid with an energy gap larger than zero and smaller than a few electron volt (up to about 3 or 4 eV). Metals do not have an energy gap, whereas it is usually larger than a few electron volt in insulators. In order to give a meaning to the notion "energy gap", we shall review some topics about the crystal structure of solids in the section 1.4.

Nanostructures are generally regarded as ideal systems for the study of electronic transport [1]. A *nanodevice* is a functional structure with nanoscale dimensions which performs some useful operation, for example a nanoscale transistor. One can generically consider the prototypical nanodevice illustrated in Fig. 1.1. The "device" can be considered an active region coupled to two contacts, left and right, which serve as a source and sink (drain) for electrons. Here the contacts are drawn as metallic-like reservoirs, characterized by chemical potentials μ_S and μ_D , and are separated by an external bias, $qV_A = \mu_S - \mu_D$.

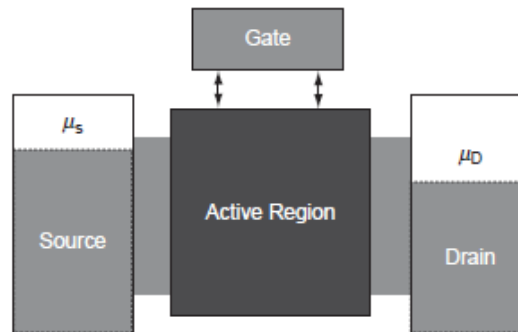


Fig. 1.1 Schematic of a generic nanoelectronic device consisting of source and drain contacts with a *gate* which controls the transfer characteristics of the active region.

The current flowing through the device is then a property of the chemical potential difference and the transmission properties of the active region itself. A separate gate electrode serves to change the transmission properties of the active region, and hence controls the current.

To fabricate nanodevices beyond current limits dictated by scaling, CMOS technology is rapidly moving towards quasi-3D structures such as dual-gate, tri-gate, and FinFET structures, in which the active channel is increasingly a nanowire or nanotube rather than bulk region.

1.2 Low-dimensional systems

When electronic processes are taking place in structures with sizes of the order of centimeters, or even microns, one can describe what is happening with the classical physics. By changing conditions very slightly, one can expect the results to show only very slight changes.

Instead, when the physical size of the system becomes smaller, quantum effects on electronic properties become important and then a description via quantum mechanics is required. These quantum effects arise in systems which confine electrons to regions comparable to their de Broglie wavelength. When such confinement occurs in one dimension only with free motion in the other ones, a "two-dimensional electron gas" (2DEG) is created. Confinement across two directions with free motion in the third gives a "one-dimensional electron gas" (1DEG) and confinement in all three-dimensions gives a "zero-dimensional electron gas" (0DEG) [2].

Artificially, confined structures are now routinely realized through advanced *epitaxial growth* which consists in the deposition of atoms that continue the crystal structure of a substrate and *lithography techniques* in which the relevant dimensions are smaller than the phase

coherence length of charge carriers.

It is instructive to make some considerations about *density of states* in this low-dimensional structures. The density of states is defined as the number of states per energy per unit volume of real space [3]:

$$\rho(E) = \frac{dN}{dE}. \quad (1.1)$$

In k -space, the total number of states N is equal to the volume of the sphere of radius k , divided by the volume occupied by one state and divided again by the volume of real space, i.e.

$$N^{3D} = 2 \frac{4\pi k^3}{3} \frac{1}{(2\pi/L)^3} \frac{1}{L^3} = 2 \frac{4\pi k^3}{3(2\pi)^3} \quad (1.2)$$

where the factor two accounts for the spin-degeneracy of the electrons. Then one has:

$$\rho^{3D}(E) = \frac{dN^{3D}}{dE} = \frac{dN^{3D}}{dk} \frac{dk}{dE}. \quad (1.3)$$

With the parabolic bands of effective mass theory (see sec.1.4) that gives us

$$E = \frac{\hbar^2 k^2}{2m^*}, \quad k = \frac{\sqrt{2m^*E}}{\hbar}, \quad dk = \frac{\sqrt{2m^*}}{\hbar} \frac{1}{2\sqrt{E}} dE, \quad (1.4)$$

the resulting density of states of a free-electron gas in three dimensions is:

$$\rho^{3D}(E) = \frac{1}{2\pi^2} \left(\frac{2m^*}{\hbar^2} \right)^{3/2} \sqrt{E}. \quad (1.5)$$

Thus the density of states is continual and proportional to the square root of the energy. This results from the fact that, in three dimensions, the surface of constant energy in k -space are spheres of radius $\sqrt{2m^*E}/\hbar$.

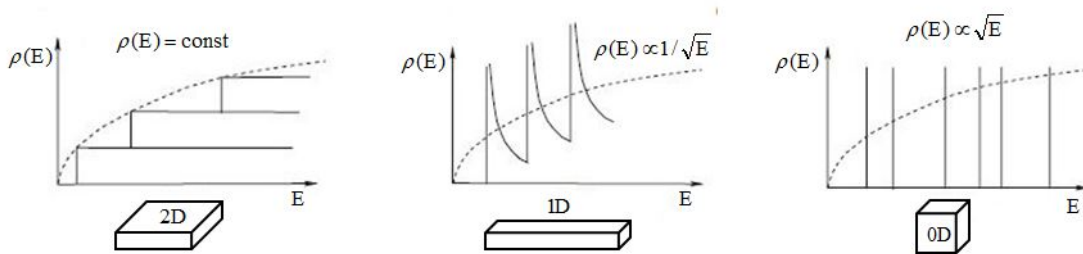


Fig. 1.2 Density of states in low-dimensional systems (quantum well, quantum wire and quantum dot respectively), compared with the 3D case (dashed lines).

If now we consider a *quantum well* (QW) system, which is referred to as a 2DEG structure, the density of states follows analogously; however this time, there are two degrees of freedom and hence the total number of states per unit cross-sectional area is given by the area of the circle of radius k , divided by the area occupied by each state, i.e.

$$N^{2D} = 2\pi k^2 \frac{1}{(2\pi/L)^2} \frac{1}{L^2} = 2 \frac{\pi k^2}{(2\pi)^2}. \quad (1.6)$$

With the reuse of eq. (1.3) and the relationship between E and k in (1.4), the density of states of a 2DEG in terms of the energy writes:

$$\rho^{2D}(E) = \frac{m^*}{\pi\hbar^2}. \quad (1.7)$$

Thus, for a 2DEG the density of states is a constant, i.e. independent of the energy (Fig. (1.2)). This is one of the fundamental features of electrons in nanoscale devices which make such structures useful for applications.

1.3 Quantum wires

With the use of nanoscale lithography techniques, many variety of structures can be envisioned. Assuming we start with a 2DEG heterostructures, confinement of the 2DEG in another direction, forms what is called a *quantum wire*, which corresponds to a quasi-one-dimensional system. Additional confinement in the remaining direction completely confines the motion of charge carriers, giving rise to system called *quantum dots*.

Among the emerging devices for the future nanoelectronic technology, semiconductor nanowires are playing a primary role not only for their transport characteristics or for more advanced nanodevice applications as resonant tunneling diodes, single electron transistors, and field-effect structures but also for the other application fields such as biological and nanomechanical sensors. Due to increasing technical difficulties in fabricating planar devices of sub-50 nm critical dimension, one-dimensional nanowire devices have been suggested as an alternative, to achieve a high stacking density.

Silicon nanowires can be used to fabricate vertical surrounding gate MOSFETs, resistors, and diodes which are the primary building blocks to form high-density circuits for several purpose. Their electrical transport properties are particularly important since controllable and predictable conductance is vital to many nanoscale electronics applications.

There are several methods to fabricate quantum wires, one of the major broad techniques is *vapor-phase synthesis*, in which nanowires are grown by starting from appropriate gaseous components. An extremely popular method for the fabrication of a variety of nanowires is the so-called *vapor-liquid-solid* (VLS) mechanism which uses metallic nanoparticles as seed sites to stimulate the self-assembled growth of nanowires. The desired semiconductor system is introduced in terms of its gaseous component and the entire assembly is heated to a temperature beyond the eutectic temperature of the metal/semiconductor system. Traditionally semiconductor technology is realized by a combination of high-resolution lithography and by etching a two-dimensional electron gas structure, as shown in Fig. 1.3.

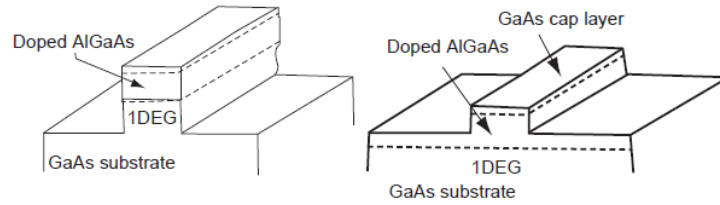


Fig. 1.3 Two different realizations of quantum wires by etching. Illustration from [1].

However we will omit the details of fabrication of this nanowires, since the main electron transport properties should be independent of the exact mechanism of fabrication.

The density of states in QWRs is obtained proceeding with the same argument in the previous section. The total number of states N is equal to the length of the line in k -space ($2k$), divided by the length occupied by one state ($2\pi/L$) and divided by the length in real space, i.e.

$$N^{1D} = 2 \times 2k \frac{1}{2\pi/L} \frac{1}{L} = \frac{4k}{2\pi}. \quad (1.8)$$

In analogy to both the bulk and quantum-well cases, let's define the density of states for a one-dimensional wire as:

$$\rho^{1D}(E) = \frac{dN^{1D}}{dE} = \frac{dN^{1D}}{dk} \frac{dk}{dE}. \quad (1.9)$$

If the energy along the axis is described with parabolic band, the relationships eqs.(1.4) can be reused. Finally, one obtains:

$$\rho^{1D}(E) = \frac{\sqrt{2m^*}}{\pi\hbar} \frac{1}{\sqrt{E}}. \quad (1.10)$$

This shows that the density of states of a 1DEG has a square-root singularity at the origin (see Fig. 1.2).

If there are many (n) confined states within the quantum wire with subband minima E_i , then the density of states at any particular energy is the sum over all the subbands below the point, which can be written as:

$$\rho^{1D}(E) = \sum_{i=1}^n \frac{\sqrt{2m^*}}{\pi\hbar} \frac{\delta(E - E_i)}{\sqrt{E - E_i}}. \quad (1.11)$$

where $\delta(x)$ is the Dirac delta-function.

There are many semiconductor material systems which would be suitable for fabrication of nanowires. Quite a few have been demonstrated successfully, including silicon, silicon-germanium, indium oxide, tin oxide, gallium-nitride. Among others and yet silicon stands out as a clear favorite to be a practical, versatile and dominant material in modern microelectronics.

1.4 Properties of Silicon

In this section general properties of bulk silicon should be discussed. The atomic structure of silicon (Si), which is like the diamond structure, is formed by a face centered cubic lattice with a basis composed by two identical atoms in the *primitive cell*, one at the corners of the cube and a second one along the diagonal of the cube at 1/4 of its length. In the cubic crystallographic axes, the coordinates of the atoms of the basis are $(0,0,0)$ and $(1/4,1/4,1/4)$. Thus, the crystal is formed by two face centered cubic interpenetrated structures at the distance of one fourth of the diagonal of the cube. If the two atoms in the primitive cell are different, the crystal structure is called zinc-blende structure, which has its name by the substance zinc-blende (ZnS). The most important materials for semiconductor physics have either diamond structure (Si, Ge) or zinc-blende structure (GaAs, GaP, AlAs, InAs, InSb). The two type structures are shown in Fig. 1.4.

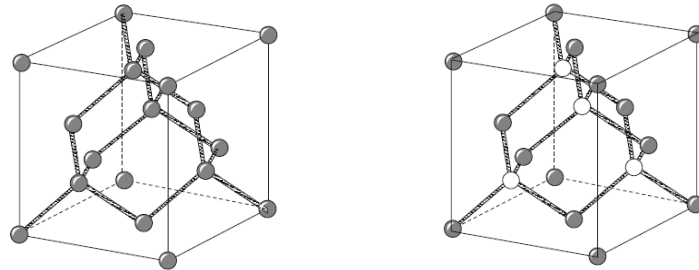


Fig. 1.4 Diamond (left) and zinc-blende (right) structures.

The reciprocal lattice of the face centred cubic lattice is the body centred cubic lattice. All points closer to one of the points of the reciprocal lattice than to any other form the *first Brillouin zone* (BZ). It is the analogous, in the reciprocal space, of the Wigner–Seitz cell of direct space. The whole BZ can be generated, through symmetry operations, by the points inside a polyhedron, called the *irreducible wedge*. All crystals which have a diamond or zinc-blende structure have a truncated octahedron-shaped first Brillouin-zone, as shown in Fig. 1.5.

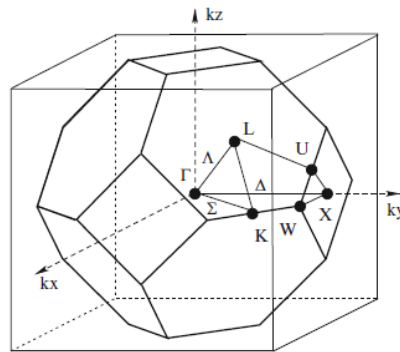


Fig. 1.5 Brillouin zone of the face centered cubic lattice with indication of the points and lines of high symmetry. The irreducible wedge is the polyhedron with vertices Γ , K , W , X , U , L .

Silicon band structure

The determination of the energy-wavevector relationship $E(\mathbf{k})$ of a moving electron, i.e. the energy band structure, is of great importance for the transport properties, because it determines both the velocity of each electron state, the density of states and electron scattering. In Fig. 1.6 the energy band structure of silicon is shown.

As one can see, there is an energy region where electronics states are not found. This is a forbidden energy region, which is termed the *band gap energy* E_g . Electronics states are permitted above and below this energy gap, where the bands above the energy gap are termed the *conduction bands* because are responsible for the electrical conduction property of the material, while the ones below are termed the *valence bands* because determine the chemical bindings.

Upon thermal or electrical excitation, electrons from the valence band can jump to the conduction band leaving behind holes. Therefore, the transport of charge is achieved through both negatively charged (electrons) and positively charged carriers (holes). In the sequel the hole motion will be neglected.

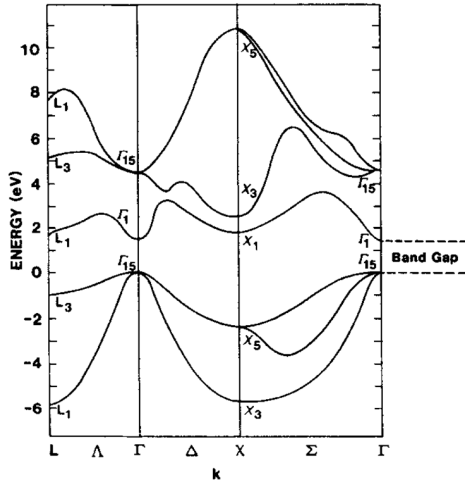


Fig. 1.6 Energy band structure of silicon.

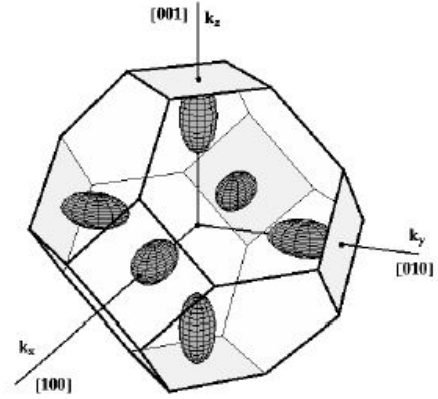


Fig. 1.7 Constant energy surface of the six valleys of the lowest conduction band in silicon.

The band structure of silicon is such that the electrons which contribute to charge transport, even at high electric fields, are those in the six equivalent ellipsoidal valleys near the X -points in the Brillouin zone (Fig. 1.7).

In the neighbourhood of the A -th valley, the function $E(k)$ may be approximated by a quadratic function of k , which may assume the following form:

$$E(k) = \frac{\hbar^2 |k|^2}{2m^*}, \quad k \text{ is assumed to vary in all } \mathbb{R}^3. \quad (1.12)$$

The scalar m^* denotes the *effective mass* of the electron in the conduction band, which is $0.32 m_e$ in Silicon. m_e is the free electron mass, whose value can be found in Tab. 2.1. Comparing this expression with the dispersion relation of a free-electron gas, $E(k) = \frac{\hbar^2 |k|^2}{2m}$ we infer that the energy of an electron near a band minimum (of an isotropic semiconductor) equals the energy of a free-electron in a vacuum where the electron rest mass m is replaced by the effective mass m^* .

Expression (1.12) is referred to as the *parabolic band approximation*; this simple model is appropriate for low applied fields for which the carriers are close to the conduction band minimum. For high applied fields, the energy of carriers may be far from a band edge, and then the $E(k)$ relation varies non-parabolically with k . In order to account for non parabolic effects, a more appropriate analytical fitting approximation in the sense of Kane is used:

$$E(k)(1 + \alpha E(k)) = \gamma = \frac{\hbar^2 |k|^2}{2m^*}, \quad (1.13)$$

where α is the non-parabolicity factor (e.g. for silicon $\alpha = 0.5 \text{ eV}^{-1}$ for each X -valley).

1.5 Electronic band structure in SiNW

As mentioned above, in bulk Silicon the lowest conduction band is formed by six equivalent valleys near the X -point of the Brillouin zone. In this case we have an indirect band-gap of 1.143 eV at $\pm 0.85 \frac{2\pi}{a_0}$ in the Δ direction with $m_t^* = 0.19$, $m_l^* = 0.98$ (units electron mass), and lattice parameter $a_0 = 5.43 \text{ \AA}$ [9].

However, due to strong manifestations of quantum effects, silicon properties in low dimensionality systems become different from those of the bulk material. For this reason, in silicon nanowires the band structure is altered with respect to the bulk case depending on the cross-section wire dimension, the atomic configuration, and the crystal orientation.

The Atomistic modeling is able to capture the nanowire band structure, including information about band coupling and mass variations as functions of quantization ([10–14]). Atomistic simulations are more appropriate for nanowires of a few nanometers cross-sectional sides, due to the high variability of the involved parameters.

However, for SiNW with cross-sections greater than 3 nm, Atomistic simulations using the *tight-binding* (TB) approach show that the band structure is more stable [11]. For a rectangular SiNW with longitudinal direction along the [100] crystal orientation, confined in the plane (y,z) , the 1-D Brillouin zone is $1/2$ as long as the length of the bulk Si Brillouin zone along the Δ line (i.e. π/a_0).

The behaviour of the electrons in the plane perpendicular to longitudinal extension of the wire is described by the effective mass equation. This leads to a split-up of the band structure in *subbands*. In SiNW the six equivalent Δ conduction valleys of the bulk Si are split into two groups because of the quantum confinement (see Fig. (1.8)).

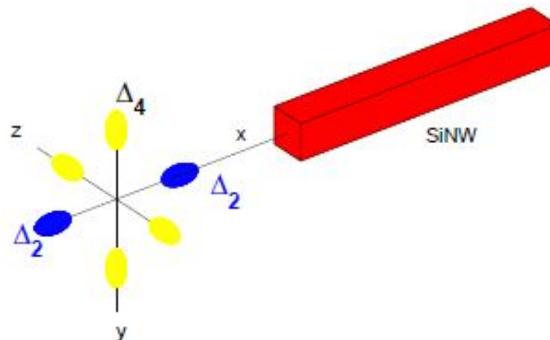


Fig. 1.8 Schematic view of a SiNW. Electron transport is assumed to be one-dimensional in the x -direction.

The subbands related to the four **unprimed** valleys Δ_4 ($[0 \pm 10]$ and $[00 \pm 1]$ orthogonal to the wire axis) are projected into a unique valley in the Γ point of the one-dimensional Brillouin zone. Therefore Si nanowire is a direct band-gap semiconductor.

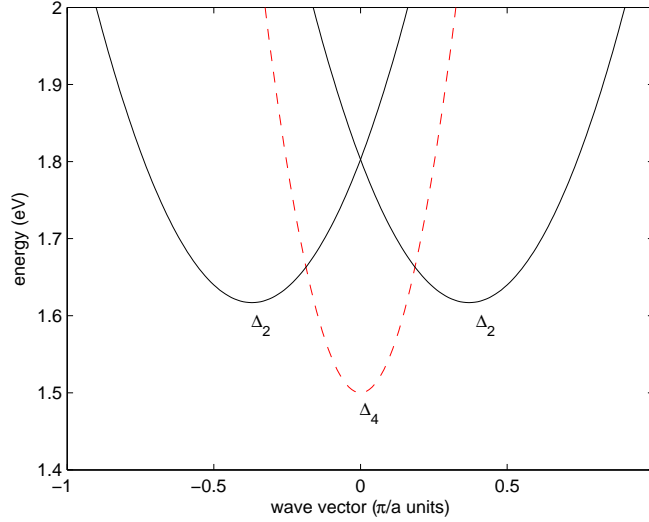


Fig. 1.9 SiNW band structure calculated from the empirical tight-binding model ([11]).

The subbands related to the **primed** valleys Δ_2 ($[\pm 100]$ along the wire axis) are found at higher energies and exhibit a minimum, located at $k_x = \pm 0.37\pi/a_0$ (see Fig. 1.9), and the energy gap between the Δ_4 and Δ_2 bottom valley is 117 meV. From the energy dispersion relation $E(k)$ obtained from the TB, one can evaluate the effective mass m^* in the parabolic spherical band approximation, i.e.

$$\frac{1}{m^*} = \frac{1}{\hbar^2} \frac{\partial^2 E}{\partial k^2} \quad (1.14)$$

obtaining $m_{\Delta_2}^* = 0.94$, $m_{\Delta_4}^* = 0.27$. Nonparabolic correction to eq. (1.14) can be introduced ([12, 15, 16]) but the fitting parameter depend heavily on the particular atomic configuration.

Chapter 2

The Schrödinger effective mass equation

In this chapter a large review is dedicated to the application of the Schrödinger equation in the effective mass approximation to the quantum wire where it is assumed that the electrons in the direction of the linear expansion of the wire are described by plane waves. The effective mass equation is solved using a finite difference numerical scheme and via a Variational Method, which has the main advantage to eliminate discretization errors as well as to cut down computational time with respect to a purely-numerical approach.

2.1 Quantum confinement

As already mentioned, silicon nanowires are quasi-one-dimensional structures in which electrons are spatially confined in two transverse directions and are free to move in one direction. The transport of charges occurs just in one dimension similar to a classical movement in one direction. In the two other dimensions the charges are confined in a quantum mechanical manner.

For a quantum wire with linear expansion in x -direction, and confined in the plane y - z , the normed electron wave function $\psi(x, y, z)$ can be written in the form [1]:

$$\psi(x, y, z) = \chi_l^\mu(y, z) \frac{e^{ik_x x}}{\sqrt{L_x}} \quad (2.1)$$

where μ is the valley index (one Δ_4 valley and two Δ_2 valleys), $l = 1, N_{sub}$ the subband index, $\chi_l^\mu(y, z)$ is the envelope function of the l -th subband and μ -th valley, and the term $e^{ik_x x} / \sqrt{L_x}$ describes an independent plane wave in x -direction confined to the normalization length, $x \in [0, L_x]$, with wave vector number k_x .

Let's consider a set of conduction electrons moving in the wire. Any one electron is subject to external confining potential $U(y, z)$, such as by a discontinuity in the band gap at an interface between two materials, and also to the presence of the other free electrons in the system in which it finds itself. The simplest approximation which takes into account the presence of many electrons, called *Hartree approximation*, is to assume that the electrons as whole produce an average electrostatic potential ϕ [2]. Then a given electron feels the resulting total potential V_{tot} , i.e.

$$V_{tot}(x, y, z) = U(x, y) - e\phi(x, y, z). \quad (2.2)$$

where e is the absolute value of the electric charge. The normed wave function satisfies the two-dimensional Schrödinger equation in the Effective Mass Approximation (EMA)

$$\left[E_c - \frac{\hbar^2}{2m_\mu^*} \Delta + V_{tot}(x, y, z) \right] \psi = E \psi \quad (2.3)$$

where E is the total energy, E_c the energy at the conduction band minimum, and m^* is the effective electron mass. By inserting (2.1) into (2.3), in each x -th cross section of the device, one obtains the following equation for the envelope function $\chi_{lx}^\mu(y, z)$

$$\left[-\frac{\hbar^2}{2m_\mu^*} \left(\frac{\partial^2}{\partial x^2} + \frac{\partial^2}{\partial y^2} \right) + V_{tot}(x, y, z) \right] \chi_{lx}^\mu = \varepsilon_{lx}^\mu \chi_{lx}^\mu, \quad E_{lx}^\mu = \varepsilon_{lx}^\mu + \frac{\hbar^2 k_x^2}{2m_\mu^*} + E_c \quad (2.4)$$

where ε_{lx}^μ is the kinetic energy associated with the confinement in the y - z plane, and $\mathcal{E}(k_x) = \frac{\hbar^2 k_x^2}{2m_\mu^*}$ is the energy along the x -direction in the parabolic band approximation. In a non-parabolic ansatz this term has to be replaced by the Kane dispersion relation eq. (1.13).

We note that, the solution of the effective mass equation (2.4) for a quantum wire in each x -cross section of the wire, can be reduced to the solution of the following eigenvalue equation

$$H\chi(y, z) = \varepsilon\chi(y, z) \quad (2.5)$$

for the Hamiltonian Operator

$$H = \left[-\frac{\hbar^2}{2m_\mu^*} \left(\frac{\partial^2}{\partial y^2} + \frac{\partial^2}{\partial z^2} \right) + U - e\phi \right]. \quad (2.6)$$

We underline that for nanowires with diameter smaller than 4 nm, a full band treatment or atomistic simulations are required, since the effective mass approximation is largely out of its range of validity and is not able to provide accurate estimates of energy gaps and dispersion

Table 2.1 Physical constants

Planck's constant/ 2π	\hbar	$6.58203 \cdot 10^{-16}$	eV s
Boltzmann constant	k_B	$8.61722 \cdot 10^{-5}$	eV K ⁻¹
electron mass	m_e	$5.68555 \cdot 10^{-30}$	eV s ² nm ⁻²
electron charge	e	-1	eV V ⁻¹
absolute dielectric constant	ϵ_0	$8.854 \cdot 10^{-12}$	e/(Vm)
relative dielectric constant of Si	ϵ_{rSi}	11.7	
relative dielectric constant of SiO ₂	ϵ_{rSiO_2}	3.9	

relations in the longitudinal direction. However, as far as an exploration of the design space is concerned, such approach is still too computationally demanding.

By solving the eq. (2.5) one finds a countable set of eigen-pairs $\chi_l^\mu, \epsilon_l^\mu$, while V is obtained from the Poisson equation

$$\nabla \cdot [\epsilon_0 \epsilon_r \nabla \phi(x, y, z)] = -e(N_D - N_A - n) \quad (2.7)$$

where ϵ_0 is the absolute dielectric constants, ϵ_r is the relative dielectric constant and N_D, N_A are the assigned doping profiles (due to donors and acceptors). All physical constants can be found in Tab. 2.1.

The term $n(t, x)$ is the *total electron density*, which depends on χ_{lx}^μ :

$$n(t, x) = \sum_{\mu} \sum_l \rho_l^\mu(x, t) |\chi_{lx}^\mu(y, z, t)|^2, \quad (2.8)$$

where $\rho_l^\mu(x, t)$ is the *linear density* in the μ -valley and l -subband

$$\rho_l^\mu(x, t) = \frac{2}{2\pi} \int f_l^\mu(x, k_x, t) dk_x, \quad (2.9)$$

f_l^μ being the electron *distribution function*, which must be evaluated by the transport model in the free movement direction, described in Chapter 4.

Hence one have to solve a coupled problem formed by eqs. (2.4),(2.7) to find $\epsilon_{\alpha z}, \chi_{\alpha z}$ in each cross-section. An adaptive numerical scheme was been performed and it will be discussed in Chapter 6.

2.2 Infinitely deep rectangular wires

The simplest quantum wire geometry would be a rectangular cross-section (with lengths L_y , L_z) and an infinite potential outside of the region defining the wire. This is illustrated schematically in Fig. 2.1 and can be considered to be the two-dimensional analogy to the one-dimensional confinement potential of the standard infinitely deep quantum well [2, 3]. Within the quantum wire, the confining potential energy U is zero, while outside the wire it

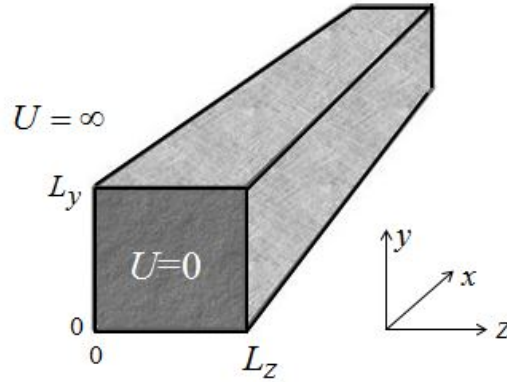


Fig. 2.1 The infinitely deep rectangular cross-section quantum wire.

is infinite; thus in the latter case the wave function is zero. Hence, the Schrödinger equation is only defined within the wire for the motion in the two confined y - z directions, i.e. equation (2.4) (with $\varphi = 0$) becomes (we omit the indices μ and l):

$$\left[-\frac{\hbar^2}{2m^*} \left(\frac{\partial^2 \chi(y,z)}{\partial y^2} + \frac{\partial^2 \chi(y,z)}{\partial z^2} \right) \right] = \varepsilon_{y,z} \chi(y,z). \quad (2.10)$$

The form of the potential in the Schrödinger equation allows the motions to be decoupled further, writing [3]:

$$\chi(y,z) = \chi(y)\chi(z) \quad (2.11)$$

and then:

$$-\frac{\hbar^2}{2m^*} \chi(z) \frac{\partial^2 \chi(y)}{\partial y^2} - \frac{\hbar^2}{2m^*} \chi(y) \frac{\partial^2 \chi(z)}{\partial z^2} = \varepsilon_{y,z} \chi(y)\chi(z). \quad (2.12)$$

Moreover, it is possible to separate the energy terms on the left-hand side of the eq. (2.12) in two energy components $\varepsilon_{y,z} = \varepsilon_y + \varepsilon_z$, then:

$$-\frac{\hbar^2}{2m^*} \chi(z) \frac{\partial^2 \chi(y)}{\partial y^2} - \frac{\hbar^2}{2m^*} \chi(y) \frac{\partial^2 \chi(z)}{\partial z^2} = \chi(z) \varepsilon_y \chi(y) + \chi(y) \varepsilon_z \chi(z). \quad (2.13)$$

Therefore it has to solve the following equations:

$$-\frac{\hbar^2}{2m^*}\chi(z)\frac{\partial^2\chi(y)}{\partial y^2}=\chi(z)\varepsilon_y\chi(y), \quad (2.14)$$

$$-\frac{\hbar^2}{2m^*}\chi(y)\frac{\partial^2\chi(z)}{\partial z^2}=\chi(y)\varepsilon_z\chi(z). \quad (2.15)$$

Dividing the first of this pair of equations by $\chi(z)$ and the second by $\chi(y)$ gives:

$$-\frac{\hbar^2}{2m^*}\frac{\partial^2\chi(y)}{\partial y^2}=\varepsilon_y\chi(y) \quad (2.16)$$

$$-\frac{\hbar^2}{2m^*}\frac{\partial^2\chi(z)}{\partial z^2}=\varepsilon_z\chi(z). \quad (2.17)$$

Given that the potential outside the wire is infinite, standard boundary conditions in the wave function holds, i.e. both $\chi(y)$ and $\chi(z)$ are zero at the edges of the wire.

In this way analytical solutions for the confinement energies $\varepsilon_{y,z}$ and envelope functions $\chi(y,z)$ are obtained:

$$\chi_l^\mu = \sqrt{\frac{2}{L_y}} \sin\left(\frac{n_y\pi y}{L_y}\right) \sqrt{\frac{2}{L_z}} \sin\left(\frac{n_z\pi z}{L_z}\right), \quad (2.18)$$

$$\varepsilon_l^\mu = \frac{\hbar^2\pi^2}{2m_\mu^*} \left(\frac{n_y^2}{L_y^2} + \frac{n_z^2}{L_z^2} \right), \quad l = (n_y, n_z) \quad (2.19)$$

where L_y and L_z are the dimensions of the wire and the origin of the coordinate system has been placed at one corner of the wire. The positive integer values n_y, n_z (quantum numbers) specify the (n_y, n_z) subband, and the ε_l^μ are the subband minima energies. We notice that the wave functions fulfill the normalization condition, i.e.

$$\int_0^{L_y} \int_0^{L_z} |\chi_l^\mu(y,z)|^2 dy dz = 1. \quad (2.20)$$

2.3 Finite rectangular wire

More relevant to real devices would be a rectangular cross-sectional quantum wire, but with finite height barriers (Fig. 2.2). With this configuration it is not possible to separate the y and z motions. Therefore, it is necessary to undertake other ways in order to solve the EMA equation.

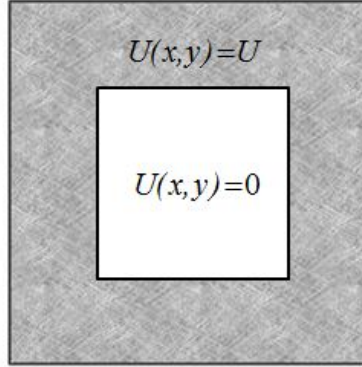


Fig. 2.2 The rectangular cross-section quantum wire with finite barriers.

For a fixed total potential $V_{tot}(x, y, z)$ in each cross-section (with $x = \text{const.}$) one has to solve the eigenvalues problem (2.4). This can be achieved or by using a finite difference numerical scheme, or by means of a Variational Method. In the next sections it will be presented both approaches.

2.3.1 Finite difference scheme for the EMA

We derive a discretization scheme of the two dimensional Schrödinger equation using a finite difference scheme. It is well known that the Finite Difference Methods are used to approximate derivatives to solve differential equations numerically. In particular the derivatives are replaced with finite difference approximations on a discretized domain. For this reason we make use of a central finite difference formula to approximate the second-order derivative in the EMA equation and to linearize the problem. By doing so, we convert the finite well problem to a simple eigenvalue problem.

In general the first derivative of a function f at a point x , with a small value δx , can be defined by

$$\frac{df}{dx} = \frac{f(x + \delta x) - f(x - \delta x)}{2\delta x} + O(\delta x^2) \quad (2.21)$$

i.e. the centered difference formula has an error of the second order. By using the above finite difference form for $f'(x + \delta x)$ and $f'(x - \delta x)$ and applying a central difference formula for the derivative of f' at x :

$$\frac{d^2 f}{dx^2} \approx \frac{\frac{df}{dx}|_{x+\delta x} - \frac{df}{dx}|_{x-\delta x}}{2\delta x}, \quad (2.22)$$

we obtain the central difference approximation (of second order) of the second derivative of f :

$$\frac{d^2 f}{dx^2} \approx \frac{f(x+2\delta x) - 2f(x) + f(x-2\delta x)}{(2\delta x)^2}. \quad (2.23)$$

Expanding the two derivatives in terms of finite differences using this form in the original Schrödinger equation and substituting the undefined small step δx for $2\delta x$, we get :

$$\begin{aligned} & -\frac{\hbar^2}{2m^*} \left[\frac{\chi(y+\delta y, z) - 2\chi(y, z) + \chi(y-\delta y, z)}{(\delta y)^2} \right. \\ & \left. + \frac{\chi(y, z+\delta z) - 2\chi(y, z) + \chi(y, z-\delta z)}{(\delta z)^2} \right] + U(y, z)\chi(y, z) = \epsilon_{y,z}\chi(y, z). \end{aligned} \quad (2.24)$$

Thus the wave function at the general point $\chi(y, z)$ depends upon the values at 4 neighbouring points (see Fig. (2.3)). A 2D spatial mesh with the equidistant grid points $x_i = i \cdot dx$, $i = 0, \dots, N_1 + 1$ and $y_j = j \cdot dy$, $j = 0, \dots, N_2 + 1$ is then introduced.

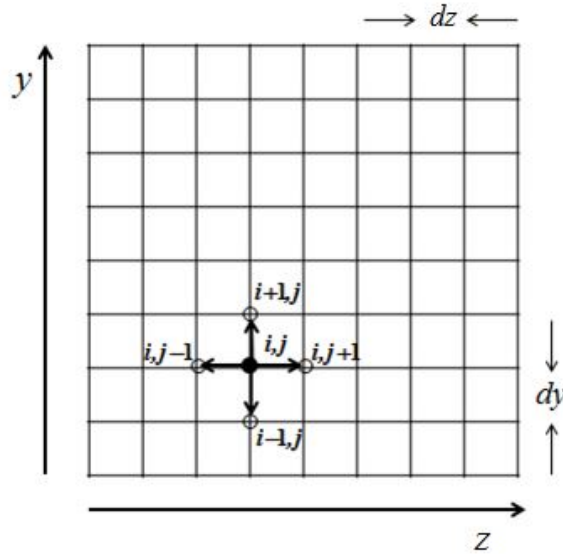


Fig. 2.3 The two-dimensional mesh for the finite different approach to the quantum wire.

Equation (2.24) can be written more compactly in terms of the indices given in Fig. 2.3 (*five-point finite difference scheme*):

$$-\frac{\hbar^2}{2m^*} \left[\frac{\chi(i+1, j) - 2\chi(i, j) + \chi(i-1, j)}{dy^2} + \frac{\chi(i, j+1) - 2\chi(i, j) + \chi(i, j-1)}{dz^2} \right] + U(i, j)\chi(i, j) = \varepsilon_{y,z}\chi(i, j) \quad , \quad i = 1, \dots, N_1, j = 1, \dots, N_2 \quad (2.25)$$

which can finally be written as:

$$\frac{\beta}{dy^2}\chi(i+1, j) - \left(\frac{2\beta}{dy^2} + \frac{2\beta}{dz^2} - U(i, j) \right)\chi(i, j) + \frac{\beta}{dy^2}\chi(i-1, j) + \frac{\beta}{dz^2}\left(\chi(i, j+1) + \chi(i, j-1)\right) = \varepsilon_{y,z}\chi(i, j) \quad , \quad i = 1, \dots, N_1, j = 1, \dots, N_2. \quad (2.26)$$

where $\beta = -\frac{\hbar^2}{2m^*}$. If we assume zero Dirichlet boundary conditions (i.e. $\chi(x=0, y) = \chi(x, y=0) = 0$ and $\chi(x=N_1+1, y) = \chi(x, y=N_2+1) = 0$) and considering each of the points of the domain, we get a system of $N = N_1N_2$ equations:

$$\begin{aligned} & -\frac{\beta}{dy^2}\chi(2, 1) - \left(\frac{2\beta}{dy^2} + \frac{2\beta}{dz^2} - U(1, 1) \right)\chi(1, 1) - \frac{\beta}{dz^2}\chi(1, 2) = \varepsilon_{y,z}\chi(1, 1) \\ & -\frac{\beta}{dy^2}\chi(2, 2) - \left(\frac{2\beta}{dy^2} + \frac{2\beta}{dz^2} - U(1, 2) \right)\chi(1, 2) - \frac{\beta}{dz^2}\left(\chi(1, 3) + \chi(1, 1)\right) = \varepsilon_{y,z}\chi(1, 2) \\ & \dots\dots \\ & \dots\dots \\ & -\frac{\beta}{dy^2}\chi(N_1, N_2) - \left(\frac{2\beta}{dy^2} + \frac{2\beta}{dz^2} - U(N_1, N_2 - 1) \right)\chi(N_1, N_2 - 1) - \\ & \quad \frac{\beta}{dz^2}\left(\chi(N_1, N_2) + \chi(N_1, N_2 - 2)\right) = \varepsilon_{y,z}\chi(N_1, N_2 - 1) \\ & -\frac{\beta}{dy^2}\chi(N_1 - 1, N_2) - \left(\frac{2\beta}{dy^2} + \frac{2\beta}{dz^2} - U(N_1, N_2) \right)\chi(N_1, N_2) - \frac{\beta}{dz^2}\chi(N_1, N_2 - 1) = \varepsilon_{y,z}\chi(N_1, N_2). \end{aligned}$$

The above linear system can be easily rewritten by arranged conveniently the internal mesh nodes $\{(x_i, y_j), i = 1, \dots, N_1, j = 1, \dots, N_2\}$ as a column vector $\mathbf{r}(k), k = 1, \dots, N$ such that:

$$\begin{cases} k = n - 1 + (m - 2)(N_1 - 2) \\ n = 2, \dots, N_1 - 1 \\ m = 2, \dots, N_2 - 1 \end{cases}$$

The equation (2.26), in term of the vector \mathbf{r} , writes:

$$\begin{aligned} \frac{\beta}{dy^2} \chi(r+1) - \left(\frac{2\beta}{dy^2} + \frac{2\beta}{dz^2} - U(r) \right) \chi(r) + \frac{\beta}{dz^2} \chi(r-1) \\ + \frac{\beta}{dz^2} \left(\chi(r + (N_1 - 2)) + \chi(r - (N_1 - 2)) \right) = \varepsilon_{y,z} \chi(r). \end{aligned} \quad (2.27)$$

In this way our linear system of $N = N_1 N_2$ equations, that approximate the problem in question, can be written in this matrix form:

$$M \chi(k) = \varepsilon_{y,z} \chi(k), \quad k = 1, \dots, N \quad (2.28)$$

where $M \in \mathbb{R}^{N \times N}$ is the following sparse matrix:

$$M = \begin{pmatrix} r(1) & -\frac{\beta}{dz^2} & 0 & \dots & -\frac{\beta}{dy^2} & 0 & \dots & 0 \\ -\frac{\beta}{dz^2} & r(2) & -\frac{\beta}{dz^2} & 0 & \dots & -\frac{\beta}{dy^2} & 0 & \vdots \\ 0 & -\frac{\beta}{dz^2} & r(3) & \ddots & 0 & \dots & -\frac{\beta}{dy^2} & 0 \\ \vdots & 0 & \ddots & \ddots & 0 & 0 & \dots & -\frac{\beta}{dy^2} \\ -\frac{\beta}{dy^2} & \vdots & 0 & 0 & \ddots & \ddots & 0 & \vdots \\ 0 & -\frac{\beta}{dy^2} & \vdots & 0 & \ddots & \ddots & -\frac{\beta}{dz^2} & 0 \\ \vdots & 0 & -\frac{\beta}{dy^2} & \vdots & 0 & -\frac{\beta}{dz^2} & r(N-1) & -\frac{\beta}{dz^2} \\ 0 & \dots & 0 & -\frac{\beta}{dy^2} & \dots & 0 & -\frac{\beta}{dz^2} & r(N) \end{pmatrix} \quad (2.29)$$

Solving the differential equation EMA means now to calculate the eigenvalues of the symmetric matrix M to find the energy subbands $\varepsilon_{y,z}$ and their corresponding eigenfunctions $\chi(x, y)$ represented by the eigenvectors of the same matrix.

2.3.2 Solution of the EMA with a variational method

With the Variational Method [17], the eigenvalue problem of the Hamilton operator H is approximated by the eigenvalue problem of the matrix \mathcal{H}

$$\mathcal{H}\mathbf{v} = \lambda\mathbf{v}, \quad \mathcal{H}_{\{i\}\{j\}} = \langle \Psi_{\{i\}} | H | \Psi_{\{j\}} \rangle, \quad \mathbf{v} = (v^1, v^2, \dots) \quad (2.30)$$

where the matrix elements $\mathcal{H}_{\{i\}\{j\}}$ are expectation values of the Hamilton operator H with respect to a set of orthonormal functions $\{|\Psi_{\{1\}}\rangle, |\Psi_{\{2\}}\rangle, \dots\}$ which span the Hilbert space of H . Then the v -th approximated eigenvalue of the Hamilton operator H is the v -th eigenvalue of the matrix \mathcal{H} i.e. $\varepsilon_v \simeq \lambda_v$, and the v -th eigenfunction χ_v of the Hamilton operator H is approximates as

$$\chi_v \simeq \sum_{\{i\}} v_v^{\{i\}} |\Psi_{\{i\}}\rangle. \quad (2.31)$$

We observe that the number of the orthonormal functions that span the Hilbert space of H is infinite. Since the number of used orthonormal functions is finite, the solutions of \mathcal{H} span in general is a subspace of H . Hence the variational method is only an advantage if the set of orthonormal functions is chosen appropriately so that the matrix elements $\mathcal{H}_{\{i\}\{j\}}$ are easily calculable and the accuracy of the approximation can be ensured for a small number of orthonormal functions. A good choice for a set of orthonormal functions are the eigenstates of the two-dimensional anisotropic harmonic oscillator which are given by

$$|\Psi_{j_y, j_z}\rangle = \frac{(ab)^{\frac{1}{4}}}{\sqrt{\pi 2^{j_y+j_z} j_y! j_z!}} \exp\left(-\frac{ay^2}{2} - \frac{bz^2}{2}\right) H_{j_y}(\sqrt{a}y) H_{j_z}(\sqrt{a}z) \quad (2.32)$$

$$a = \frac{m^* \omega_y}{\hbar}, \quad b = \frac{m^* \omega_z}{\hbar}, \quad \{j\} = (j_y, j_z) \in \mathbb{N} \times \mathbb{N} \quad (2.33)$$

where j_y, j_z are the quantum numbers, $H_{j_y}(\sqrt{a}y)$ is the Hermite polynomial of order j_y and ω the angular velocity. Then, the elements of the matrix $\mathcal{H}_{\{i\}\{j\}}$ are formed by two contributions:

$$\mathcal{H}_{\{i\}\{j\}} = \mathcal{H}_{\{i\}\{j\}}^{(1)} + \mathcal{H}_{\{i\}\{j\}}^{(2)} = \langle \Psi_{\{i\}} | \left[-\frac{\hbar^2}{2m^*} \left(\frac{\partial^2}{\partial y^2} + \frac{\partial^2}{\partial z^2} \right) | \Psi_{\{j\}} \rangle + \langle \Psi_i | V_{tot} | \Psi_j \rangle. \quad (2.34)$$

The first term can be evaluated as:

$$\begin{aligned} \mathcal{H}_{\{i\}\{j\}}^{(1)} = & \frac{\hbar\omega_y}{4} \delta_{i_z, j_z} [(2j_y + 1) \delta_{i_y, j_y} - \sqrt{j_y^2 - j_y} \delta_{i_y, j_y - 2} - \sqrt{i_y^2 - i_y} \delta_{i_y - 2, j_y}] + \\ & \frac{\hbar\omega_y}{4} \delta_{i_y, j_y} [(2j_z + 1) \delta_{i_z, j_z} - \sqrt{j_z^2 - j_z} \delta_{i_z, j_z - 2} - \sqrt{i_z^2 - i_z} \delta_{i_z - 2, j_z}] \end{aligned} \quad (2.35)$$

The second term depends on $V_{tot}(x, y, z)$. Let us suppose that this term reduces to a two-dimensional finite rectangular potential well $U(y, z)$, i.e.

$$U(y, z) = \begin{cases} 0 & \forall (y, z) \in [-L_y/2, L_y/2] \times [-L_z/2, L_z/2] \\ U_0 & \text{otherwise} \end{cases} \quad (2.36)$$

where the depth of the potential well is usually taken $U_0 = -4.05$ eV (the work function of Si) and L_y and L_z are the lengths of the well in y and z direction respectively. In this case, after some calculations, we have

$$\begin{aligned} \mathcal{H}_{\{i\}\{j\}}^{(2)} = & \frac{U_0}{\pi} \sqrt{\frac{1}{2^{i_y+i_z+j_y+j_z} i_y! i_z! j_y! j_z!}} \exp \left[-\frac{1}{4} (aL_y^2 + bL_z^2) \right] \times \\ & \left\{ \sum_{k=0}^{\min(i_y, j_y)} 2^k k! \binom{i_y}{k} \binom{j_y}{k} [H_{i_y+j_y-2k-1}(-\sqrt{a}L_y/2) - H_{i_y+j_y-2k-1}(\sqrt{a}L_y/2)] \right\} \times \\ & \left\{ \sum_{k=0}^{\min(i_z, j_z)} 2^k k! \binom{i_z}{k} \binom{j_z}{k} [H_{i_z+j_z-2k-1}(-\sqrt{a}L_z/2) - H_{i_z+j_z-2k-1}(\sqrt{a}L_z/2)] \right\} \end{aligned} \quad (2.37)$$

If $j_y = 0, 1, \dots, N_y$ and $j_z = 0, 1, \dots, N_z$ then the matrix \mathcal{H} has $(N_x + 1)(N_y + 1)$ rows and columns. In the next section results for the solution of the EMA equation will be presented.

2.4 Results for the EMA equation

Just to have a comparison between the two methods solving the Schrödinger equation in the effective mass approximation, we have taken a SiNW with cross-section $L_y = L_z = 10$ nm, and we have evaluated the eigenvalues with the two methods [52]. In figure 2.4 we plot the first ten eigenvalues ε_ν obtained with the finite difference scheme, by increasing the grid points $N_g = N_1 = N_2$ (six equivalent valleys have been considered with a single effective mass $m^* = 0.32 m_e$).

From this figure we can clearly see that the convergence is reached for $N_g = 141$. In such a case, the matrix dimension is 19881×19881 and the CPU time was $\simeq 19000$ sec (using MATLAB and an AMD Phenom II X6 1090T processor).

If we want to obtain a similar result with the Variational Method, we have to take into account $N_y = N_z = 16$ quantum numbers. In this case the matrix dimension is 289×289 and the CPU time was $\simeq 163$ sec.

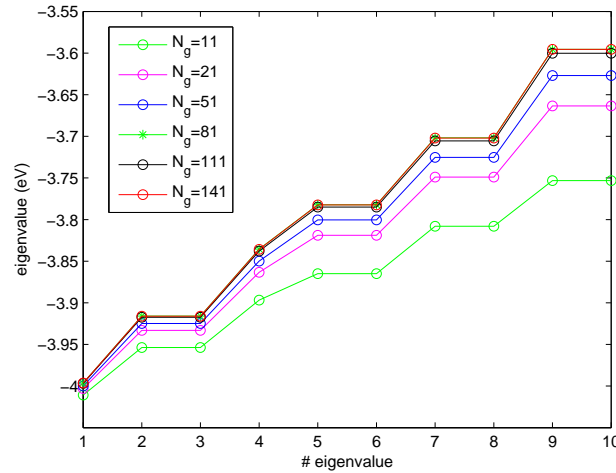


Fig. 2.4 The subband energies ε_ν , eq. (2.4) obtained with a finite difference solver, with N_g grid points in each axes.

The percentage error between the two methods is shown in figure 2.5.

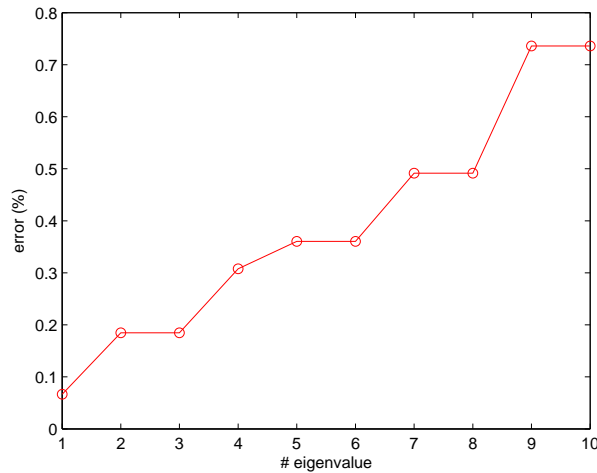


Fig. 2.5 The percentage error between the subband energies ε_ν (2.4) obtained with a finite difference solver and the Variational Method.

In Fig. 2.6 eigenfunctions associated to the first four eigenvalues obtained with finite difference method are plotted. Similar figures are get via variational method. The main advantage of the Variational Method is that no discretization error is introduced, as in the

finite difference case [18, 19], and the convergence of the results depends only on how many quantum numbers are taken.

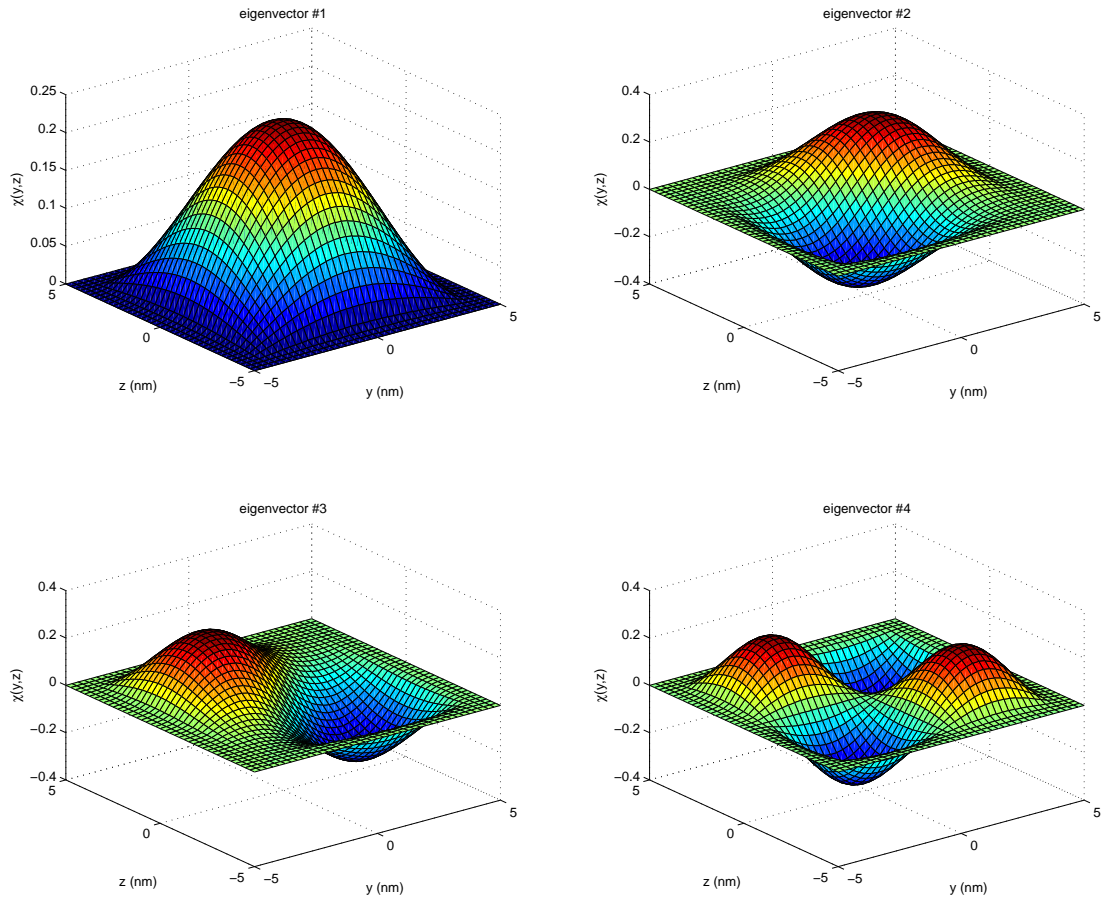


Fig. 2.6 Eigenfunctions obtained with a finite difference solver, with $N_1 = N_2 = 41$ mesh point.

Chapter 3

Carrier scattering

3.1 Introduction

The transport of charged particles, as electrons, within the body of a perfect crystal lattice, is caused by external electric or magnetic field forces and is attenuated by scattering. Therefore, carrier scattering is one of the most important processes in the transport of the carriers through the semiconductor. In this chapter, a description of carrier scattering which take into account the presence of phonons, and their interactions with the electrons is presented. In particular we distinguish between acoustic and optical electron-phonon scattering mechanisms, which are both caused by deformation potentials. Nonlattice dynamic scattering processes are also dealt with. These include ionized impurity and surface roughness scattering (SRS).

Quantum mechanical scattering is usually summarized in terms of *Fermi's Golden Rule*, which is derived from the time-dependent perturbation theory of the first order. It gives the *transition probability* between two eigenstates, which are the solutions of Schrödinger wave equation for the perturbation potential H_p . The transition rate $w(k, k')$, which is essential for the description of any particle transport with a semiclassical approach, represents the probability that an electron with wave number vector k , due to a scattering, passes into a state with wave number vector k' in the unit time [4, 5, 7].

In the case of quantum wires, one has

$$w(\mathbf{k}, \mathbf{k}') = w(k_x, \mu, l, k'_x, \mu', l') = w(k_x, k'_x)$$

representing the probability per unit time that the state ψ becomes the state ψ'

$$\psi(x, y, z) = \chi_l^\mu(y, z) \frac{e^{ik_x x}}{\sqrt{L_x}} \longrightarrow \psi'(x, y, z) = \chi_{l'}^{\mu'}(y, z) \frac{e^{ik'_x x}}{\sqrt{L_x}} \quad (3.1)$$

where the indexes μ and μ' indicate different valleys, l and l' different subbands. The transitions rate fulfill the Fermi's Golden rule, i.e.

$$w(k_x, k'_x) = \frac{2\pi}{\hbar} |\langle \psi' | H_p | \psi \rangle|^2 \delta(E(\psi') - E(\psi) \mp \hbar\omega_q) \quad (3.2)$$

where δ stands for the Dirac Delta which shows that (3.2) differs from zero only if the argument of the δ -function is zero, a condition that express the conservation of energy. The term $\pm \hbar\omega_q$ enables it that a particle of wave vector q is involved in the scattering process (the upper sign corresponds to the absorption and the lower sign for emission).

The term $E(\psi)$ express the energy given by eq. (2.4) and includes thus the possibility of intervalley and intersubband scattering processes. The expression $|\langle \psi' | H_p | \psi \rangle|^2$ is the square of the absolute value of the matrix element of the perturbation potential H_p .

Equation (3.2) is the basic result of the scattering theory, which we apply to the scattering calculation of carriers in the next sections.

3.2 The Electron-Phonon interaction

In a crystal electrons are scattered by lattice vibrations propagating in the crystal because the periodicity of the crystal potential may be disturbed for various reasons. Because of the difficulty of knowing the crystal potential itself, this deviation from the periodicity is expressed in a rather phenomenological way, such as the *deformation potential method*. Since the wave nature of the lattice vibrations can be quantized as *phonons*, the influence of lattice vibrations on electron motions can be expressed by a quantum process that is termed the *electron-phonon interaction*.

The electron-phonon interaction is one of the dominant scattering processes in submicron semiconductor devices. Carriers in such small-sized devices can acquire high energy levels from the high electric field applied; hence, scatterings based on the spontaneous emission of phonons take place even though there are only a few phonons present at low temperature.

Although the electrons in a quantum wire are confined in two dimensions and act only in one dimension as a classical particle, we treat the phonons as bulk phonons.

The main lattice vibrations are due to acoustic and non-polar optical branches. The acoustic modes shown in Fig. 3.1 are characterised by the neighboring atoms being in phase. In the longitudinal mode the atomic displacements are in the same direction as the direction of energy transfer, while in the transverse mode the atomic displacements are perpendicular to this direction.

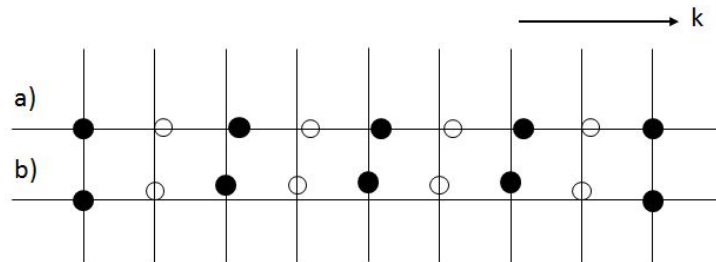


Fig. 3.1 Schematic illustrations of the atomic displacements in (a) longitudinal acoustic (LA) and (b) transverse acoustic (TA) phonon modes.

The longitudinal and transverse definitions also apply to the two types of optic phonon modes as illustrated in Fig. 3.2. However, in this type of lattice vibration the displacement of neighbouring atoms are in opposite phase [3].

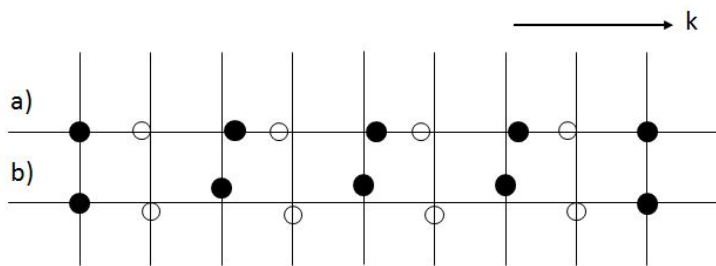


Fig. 3.2 Schematic illustrations of the atomic displacements in (a) longitudinal optic (LO) and (b) transverse optic (TO) phonon modes.

In the sequel we shall consider the acoustic phonons in the Debye approximation, where the dispersion relation, near the center of the Brillouin zone, is

$$\omega_{ac}(\mathbf{q}) = v_s |\mathbf{q}| \quad (3.3)$$

where v_s is the sound speed. The optical phonon scattering will be treated in the Einstein approximation, i.e.

$$\omega_{op}(\mathbf{q}) = \omega_0 = \text{const.} \quad (3.4)$$

The perturbation potential H_p for both these electron-phonon scattering, caused by a deformation potential, writes [5]

$$H_p = \sum_{\mathbf{q}} K_{\mathbf{q}} e^{\pm i\mathbf{q}\cdot\mathbf{x}} \sqrt{\frac{\hbar}{2\rho V_c \omega_{\mathbf{q}}}} \left[g(\mathbf{q}) + \frac{1}{2} \mp \frac{1}{2} \right] \quad (3.5)$$

where ρ is the mass density, V_c the crystal volume, $g(\mathbf{q})$ is the phonon distribution function involved in the scattering, $\hbar\omega(\mathbf{q})$ the phonon energy obtained from the phonon dispersion relation for Si, and

$$K_{\mathbf{q}} = |\mathbf{q}|D_1 : \text{First order Deformation Potential} \quad ,$$

$$K_{\mathbf{q}} = D_0 : \text{Zero order Deformation Potential} \quad .$$

By knowing the interaction potential H_p , the squared matrix element for the deformation potential scattering can be evaluated and then, after some algebra, the transition rate is obtained through the golden rule (3.2) (see Appendix A):

$$w(\mathbf{k}, \mathbf{k}') = \frac{2\pi}{\hbar} \sum_{\mathbf{q}} |G_{ll'}^{\mu\mu'\pm}(q_y, q_z)|^2 \frac{\hbar K_{\mathbf{q}}^2}{2\rho V_c \omega_{\mathbf{q}}} \left[g(\mathbf{q}) + \frac{1}{2} \mp \frac{1}{2} \right] \delta_{\mathbf{k}' \mp \mathbf{k}, \mathbf{q}} \delta(E(\psi') - E(\psi) \mp \hbar\omega_{\mathbf{q}}) . \quad (3.6)$$

The scattering mechanism can drive one electron in the same valley (intravalley) or in a different valley (intervalley). In bulk Silicon, the **intravalley** scattering involves only acoustic phonons (two types LA and TA) and they are evaluated using the First order approximation (with the Debey approximation (3.3)) [9]. The **intervalley** scattering is due to six types of phonons: three of g-type, when electrons scatter between valleys on the same axis, or of f-type when the scattering occurs between valleys on perpendicular axes, as shown in Fig. 3.3. The last ones are evaluated in the Zero order approximation (using the Einstein approximation (3.4)).

3.2.1 Non-polar Optical Phonons Scattering

In Si, the non-polar optical deformation potential is the predominant interaction of carriers with optical phonons. This may occur through intravalley scattering, or via intervalley scattering between equivalent minima.

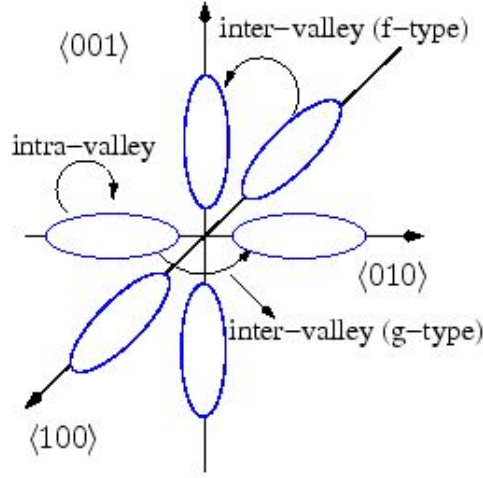


Fig. 3.3 Classification of electron-phonon transitions in silicon: intra and inter valley scattering (f-and g-type).

These phonons lead to *inelastic scattering processes*, since there is a significant gain or loss of energy by the carrier during the scattering process. As known, the transport mechanism starts by applying an external bias voltage. The electrons are accelerated by the produced electric field, thanks to which they gain energy. We need the optical phonons to relax the energy obtained from the electric field.

The eq. (3.6) for the optical phonons writes

$$w_0(\mathbf{k}, \mathbf{k}') = s_0 \left[g_0 + \frac{1}{2} \mp \frac{1}{2} \right] \sum_{\mathbf{q}} |G_{ll'}^{\mu\mu'\pm}(q_y, q_z)|^2 \delta_{\mathbf{k}_x \pm \mathbf{q}_x, \mathbf{k}'_x} \delta(E(\psi') - E(\psi) \mp \hbar\omega_0), \quad (3.7)$$

$$s_0 = \frac{\pi D_0^2}{\rho V_c \omega_0}.$$

In the following we shall consider the optical phonons in thermal equilibrium, then g_0 is the Bose-Einstein distribution, i.e.

$$g_0 = \frac{1}{\exp\left(\frac{\hbar\omega_0}{k_B T_L}\right) - 1} \quad (3.8)$$

We evaluate

$$\begin{aligned} \sum_{\mathbf{q}} |G_{ll'}^{\mu\mu'\pm}(q_y, q_z)|^2 &= \sum_{\mathbf{q}} \left| \int (\chi_{l'}^{\mu'})^*(y, z) \chi_l^{\mu}(y, z) e^{\pm i(q_y y + q_z z)} dy dz \right|^2 = \\ &= \sum_{\mathbf{q}} \int (\chi_{l'}^{\mu'})^*(y, z) \chi_l^{\mu}(y, z) e^{\pm i(q_y y + q_z z)} dy dz \int (\chi_{l'}^{\mu'})^*(y', z') \chi_l^{\mu}(y', z') e^{\mp i(q_y y' + q_z z')} dy' dz'; \end{aligned}$$

and by transforming the summation into integral

$$\sum_{\mathbf{q}} \rightarrow \sum_{q_x} \frac{V_c}{(2\pi)^2 L_x} \int dq_y dq_z,$$

one obtains

$$\begin{aligned} \frac{V_c}{(2\pi)^2 L_x} \sum_{q_x} \int (\chi_{l'}^{\mu'})^*(y, z) \chi_l^{\mu}(y, z) (\chi_{l'}^{\mu'})^*(y', z') \chi_l^{\mu}(y', z') e^{\pm i q_y (y - y')} \times \\ e^{\pm i q_z (z - z')} dy dz dy' dz' dq_y dq_z. \end{aligned}$$

Since

$$\int_{-\infty}^{+\infty} e^{iqx} dq = 2\pi \delta(x) \quad (3.9)$$

one get

$$\begin{aligned} \frac{V_c}{L_x} \sum_{q_x} \int \delta(y - y') \delta(z - z') (\chi_{l'}^{\mu'})^*(y, z) \chi_l^{\mu}(y, z) (\chi_{l'}^{\mu'})^*(y', z') \chi_l^{\mu}(y', z') dy dz dy' dz' \\ = \frac{V_c}{L_x} \sum_{q_x} \int (\chi_{l'}^{\mu'})^*(y, z) \chi_l^{\mu}(y, z) (\chi_{l'}^{\mu'})^*(y', z') \chi_l^{\mu}(y', z') dy dz \\ = \frac{V_c}{L_x} \sum_{q_x} \int |\chi_{l'}^{\mu'}(y, z)|^2 |\chi_l^{\mu}(y, z)|^2 dy dz = \frac{V_c}{L_x} \sum_{q_x} G_{ll'}^{\mu\mu'} \end{aligned} \quad (3.10)$$

where

$$G_{ll'}^{\mu\mu'} = \int |\chi_{l'}^{\mu'}(y, z)|^2 |\chi_l^{\mu}(y, z)|^2 dy dz \quad (3.11)$$

is the *overlap factor*. It determines which transitions from one valley to another are allowed and which are forbidden.

By inserting eq. (3.10) into (3.7), observing that the sum over q_x vanishes due to the delta function, we finally obtain

$$w_0(k, k') = s_0 \left[g_0 + \frac{1}{2} \mp \frac{1}{2} \right] G_{ll'}^{\mu\mu'} \delta(E_{l'}^{\mu'} - E_l^{\mu} \mp \hbar \omega_0), \quad s_0 = \frac{\pi D_0^2}{\rho \omega_0 L_x}. \quad (3.12)$$

Actually, the above expression is referred to the intravalley processes and then $\mu = \mu'$. The interaction potential for intervalley scattering has a form similar to (3.12):

$$w_{iv}(\mathbf{k}, \mathbf{k}') = s_{iv} \left[g_{iv} + \frac{1}{2} \mp \frac{1}{2} \right] G_{l'l'}^{\mu\mu'} \delta \left(E_{l'}^{\mu'} - E_l^\mu - \Delta_{\mu\mu'} \mp \hbar\omega_{iv} \right), \quad (3.13)$$

$$s_{iv} = \frac{\pi D_{iv}^2}{\rho \omega_{iv} L_x} Z_{iv}, \quad \Delta_{\mu\mu'} = \varepsilon_\mu^0 - \varepsilon_{\mu'}^0.$$

where ε_μ^0 is the bottom of the energy valley, Z_{iv} is the the number of possible final equivalent valleys for the type of intervalley scattering under consideration. In practice, for the zero-order intervalley scattering rate, ω_0 has to be replaced by ω_{iv} , D_0 has to be replaced by D_{iv} and obviously $\mu \neq \mu'$.

3.2.2 Acoustic Phonon Scattering

The results is similar to eq. (3.7), supposing to change

$$D_0 \rightarrow |\mathbf{q}|D_1, \quad \omega_0 \rightarrow \omega_{ac} = v_s|\mathbf{q}|$$

$$w_{ac}(\mathbf{k}, \mathbf{k}') = s_a \sum_{\mathbf{q}} |G_{l'l'}^{\mu\mu'}(q_y, q_z)|^2 |\mathbf{q}| \left[g_{ac}(\mathbf{q}) + \frac{1}{2} \mp \frac{1}{2} \right] \delta_{k_x \pm q_x, k'_x} \delta \left(E(\psi') - E(\psi) \mp \hbar v_s |\mathbf{q}| \right) \quad (3.14)$$

where

$$s_a = \frac{\pi D_1^2}{\rho v_s V_c}. \quad (3.15)$$

We take into account that the acoustic phonon energy $\hbar v_s |\mathbf{q}|$ is much smaller than the electron energy on the order of $k_B T_L$ (which is true at room temperature). Hence, acoustic deformation potential scattering can be considered elastic. Furthermore, we assume an equipartitioned equilibrium (Bose-Einstein) acoustic phonon distribution, thus $g_{ac}(\mathbf{q})$ can be approximated as

$$g_{ac}(\mathbf{q}) \simeq g_{ac}(\mathbf{q}) + 1 \simeq \frac{k_B T_L}{\hbar v_s |\mathbf{q}|} \quad (3.16)$$

with the Boltzmann constant k_B and the lattice temperature T_L . Then eq. (3.14) writes:

$$w_{ac}(\mathbf{k}, \mathbf{k}') = \frac{2\pi D_1^2 k_B T_L}{\rho \hbar v_s^2 V_c} \sum_{\mathbf{q}} |G_{l'l'}^{\mu\mu'\pm}(q_y, q_z)|^2 \delta_{k_x \pm q_x, k'_x} \delta \left(E_{l'}^{\mu'} - E_l^\mu \right). \quad (3.17)$$

Again the sum over q_x vanishes due to the Kronecker delta (because there is no dependence on q_x). Moreover, since w_{ac} describes intravalley processes, it is imperative that $\mu = \mu'$.

By using eqs.(3.11) we finally get the acoustic intravalley transition rate:

$$w_{ac}(k, k') = s_{ac} G_{ll'}^{\mu\mu} \delta(E_{l'}^{\mu} - E_l^{\mu}), \quad s_{ac} = \frac{2\pi D_1^2 k_B T_L}{\rho \hbar v_s^2 L_x}. \quad (3.18)$$

We observe that $G_{ll'}^{\mu\mu'} = G_{l'l}^{\mu'\mu}$ but

$$w(k, k') \neq w(k', k).$$

A possible relation between these quantities is given by the *Detailed Balance Principle*:

$$w(k_x, \mu, l, k'_x, \mu', l') = w(k'_x, \mu', l', k_x, \mu, l) \exp\left(-\frac{E_l^{\mu} - E_{l'}^{\mu'}}{k_B T_L}\right). \quad (3.19)$$

3.3 Scattering with impurities

Carriers in a semiconductor device are usually supplied or removed through heavily doped regions regarded as carrier reservoirs. In such heavily doped regions, the carrier motion is disturbed by scattering due to ionized impurities distributed randomly. This is evidenced by two observations. One is that carriers do not acquire high energy levels from low electric fields in heavily doped regions, and the other is that the impurity scattering is pronounced for low-energy carriers.

For an impurity located in the position $x_i = (x_i, y_i, z_i)$, with charge $Z_i e$, in the unscreened case we have

$$H_p = \frac{Z_i e^2}{4\pi \epsilon_s r}, \quad r^2 = (x - x_i)^2 + (y - y_i)^2 + (z - z_i)^2, \quad (3.20)$$

where ϵ_s is the static dielectric constant ($9.7 \epsilon_0$). One obtains [1]

$$\langle \psi' | H_p | \psi \rangle = \frac{Z_i e^2}{2\pi \epsilon_s L_x} e^{-iq_x x_i} \int dz \int dy (\chi_{l'}^{\mu})^* \chi_l^{\mu} K_0\left(|q_x| \sqrt{(y - y_i)^2 + (z - z_i)^2}\right) \quad (3.21)$$

where $q_x = k_x - k'_x$, and $K_0(x)$ is the modified Bessel function. Since this process is elastic and intravalley, from eq. (3.2) for the i -th impurity we get

$$w_i(k, k') = \frac{2\pi}{\hbar} \left(\frac{Z_i e^2}{2\pi \epsilon_s L_x}\right)^2 |H_{imp}(k_x - k'_x, y_i, z_i)|^2 \delta(E_{l'}^{\mu} - E_l^{\mu}) \quad (3.22)$$

where

$$H_{imp}(k_x - k'_x, y_i, z_i) = \int dz \int dy (\chi_{l'}^\mu)^* \chi_l^\mu K_0 \left(|k_x - k'_x| \sqrt{(y - y_i)^2 + (z - z_i)^2} \right) \quad (3.23)$$

In the parabolic band approximation one has:

$$E_{l'}^{\mu'} - E_l^\mu = \frac{\hbar^2}{2m^*} \left[k_x'^2 - k_x^2 + \frac{2m^*}{\hbar^2} (\epsilon_{l'}^{\mu'} - \epsilon_l^\mu) \right] \quad (3.24)$$

$$\delta(E_{l'}^{\mu'} - E_l^\mu) = \frac{2m^*}{\hbar^2} \delta \left[k_x'^2 - k_x^2 + \frac{2m^*}{\hbar^2} (\epsilon_{l'}^{\mu'} - \epsilon_l^\mu) \right] = \frac{2m^*}{\hbar^2} \delta[f(k'_x)], \quad (3.25)$$

and then

$$\delta(E_{l'}^{\mu'} - E_l^\mu) = \frac{2m^*}{\hbar^2} \frac{H(a)}{2\sqrt{a}} [\delta(k'_x - \sqrt{a}) + \delta(k'_x + \sqrt{a})], \quad a = k_x^2 + \frac{2m^*}{\hbar^2} (\epsilon_l^\mu - \epsilon_{l'}^{\mu'}) \quad (3.26)$$

where $H(a)$ is the Heaviside function. The eq. (3.22) reduces

$$w_i(k, k') = \frac{Z_i^2 e^4 m^*}{2\pi \epsilon_s L_x^2 \hbar^3} |H_{imp}(k_x - k'_x, x_i, y_i)|^2 \frac{H(a)}{\sqrt{a}} [\delta(k'_x - \sqrt{a}) + \delta(k'_x + \sqrt{a})] \quad (3.27)$$

$$a = k_x^2 + \frac{2m^*}{\hbar^2} (\epsilon_l^\mu - \epsilon_{l'}^{\mu'}).$$

If we have N_{imp} impurities in the wire, then

$$w_{imp}(k, k') = \sum_{i=1}^{N_{imp}} \frac{Z_i^2 e^4 m^*}{2\pi \epsilon_s L_x^2 \hbar^3} |H_{imp}(k_x - k'_x, x_i, y_i)|^2 \frac{H(a)}{\sqrt{a}} [\delta(k'_x - \sqrt{a}) + \delta(k'_x + \sqrt{a})]. \quad (3.28)$$

For the sake of simplicity, we shall assume that the impurities are distributed uniformly along the wire, i.e. they are located in $(x, 0, 0) \forall x \in [-L_x/2, L_x/2]$, then eq. (3.28) reduces

$$w_{imp}(k, k') = \frac{Z^2 e^4 n_i m^*}{2\pi \epsilon_s^2 L_x^2 \hbar^3} |H_{imp}(k_x - k'_x, 0, 0)|^2 \frac{H(a)}{\sqrt{a}} [\delta(k'_x - \sqrt{a}) + \delta(k'_x + \sqrt{a})]. \quad (3.29)$$

where n_i is the impurities number per unit length.

3.4 Surface roughness scattering

Surface roughness is a term generically applied to the random fluctuations of the boundaries that nominally form the confining potential to low-dimensional systems.

On a microscopic level, roughness appears as atomic layer steps in the interface between two

differing materials [1]. The fact that the interface is not abrupt on the atomic level, but that variation in the actual position of the interfacial plane can extend over one or two atomic layers along the surface, affects the transport.

In self-assembled semiconductor nanowires, roughness may be considerably more pronounced than in an epitaxially grown interface. As a consequence, while roughness scattering may be relatively weak in heterojunction 2DEG systems, in 1D wires it is a dominant effect. In the case of perfectly smooth Si-SiO₂ interface, the electron wavefunctions and energy level of each subband are obtained by solving the EMA eq. (2.4) in each x -cross section, with

$$V_{tot} = V_{eff} + U(x, y), \quad V_{eff} = -e\phi(x, y, z) + V_{im}(x, y) + V_{sc}(x, y)$$

where U is the confining potential, V_{eff} the effective potential composed by the electrostatic potential energy ϕ (satisfying the Poisson equation), V_{im} the image potential due to the mismatch of the dielectric constants between Si and SiO₂, V_{sc} the exchange-correlation energy due to the electron-electron interaction. But practically, one must take into account the roughness surface.

Usual models of roughness scattering rely on a semiclassical approach in which a phenomenological surface roughness is parameterized in terms of its height and the correlation length. Let us consider the wire interface along the y - z plane (whose normal is the x direction). The most treatments of SRS assume that the fluctuations of the interface from its ideal flat boundary are described by a two-dimensional roughness function $\Delta(y, z)$. This fluctuation changes directly the barrier potential U , and it induces a change in the other potentials. Therefore, the subband wave functions and energy bands depend explicitly from x .

For the 1D confinement (e.g. the quantum well), the first order complete theory can be found in [22]. In the case of infinite confining potential, the main results is that for silicon thickness greater than 8 nm the SRS mobility converges to the SRS bulk mobility and moreover the contribution of V_{im} , V_{sc} can be neglected.

Following [1, 26] we shall consider a simpler SRS model, where

- V_{im} , V_{sc} are neglected (which of course is true for silicon thickness greater than 8 nm);
- SRS accounts for deformations only for the potential V_{eff} (not the wave functions);
- fluctuation depends only on z , i.e. $\Delta(z)$;
- the perturbation in the potential is only in the y -variable, i.e. $V_{eff}[x, y + \Delta(x), z]$.

If we expand the potential in the y variable (with x, z constants), up to the first order in $\Delta(x)$

$$V_{eff}[x, y + \Delta(x), z] = V_{eff}[x, y + \Delta(x), z]|_{\Delta=0} + \frac{\partial V_{eff}(x, y, z)}{\partial y} \Delta(x) + \mathcal{O}(2)$$

Then the SRS matrix element is

$$H_{sr} = V_{eff}[x, y + \Delta(x), z] - V_{eff}(x, y, z) = eE_y(x, y, z)\Delta(x), \quad (3.30)$$

$$E_y(x, y, z) = \frac{1}{e} \frac{\partial V_{eff}}{\partial y} = -\frac{\partial \phi}{\partial y}. \quad (3.31)$$

Assuming exponentially correlated surface roughness, in the parabolic band approximation, one obtains [26]

$$w_{sr}(k, k', E_y) = \frac{4\sqrt{2}e^2 m_\mu^* H(a)}{\hbar^3 L_x \sqrt{a}} [\mathcal{F}_{ll'}^{\mu\mu}(E_y)]^2 \frac{\lambda_{sr} \Delta_{sr}^2}{(k_x - k'_x)^2 \lambda_{sr}^2 + 2} [\delta(k'_x - \sqrt{a}) + \delta(k'_x + \sqrt{a})], \quad (3.32)$$

$$a = k_x^2 + \frac{2m_\mu^*}{\hbar} (\epsilon_l^\mu - \epsilon_{l'}^\mu).$$

The dominant term in eq. (3.32) is the *average surface field* $\mathcal{F}_{ll'}^{\mu\mu}$

$$\mathcal{F}_{ll'}^{\mu\mu}(E_y) = \int (\chi_l^\mu)^*(y, z) E_y(x, y, z) \chi_{l'}^\mu(y, z) dy dz \quad (3.33)$$

which depends on the field perpendicular to the interface. The quantity Δ_{sr} is the the rms (root mean square) height of the roughness fluctuations and λ_{sr} is the correlation length for the fluctuations. It may be interpreted as the average distance between "bumps" at the Si-SiO₂ interface as shown in Fig. 3.4.



Fig. 3.4 Schematic representation of the surface roughness function, including the rms height and autocovariance length.

Chapter 4

Transport model for SiNW

In a purely quantum approach, the most advanced transport model for the simulation of SiNW is given by Non-Equilibrium Green's Function formalism. Another way is in the framework of quantum kinetic theory via the Wigner function. However, in structures like SiNW transistors having characteristic length of the order of a few tens of nanometers, the transport of electrons along the axis of the wire can be treated semiclassically within a good approximation. In this context, a good engineering-oriented approach is based on hydrodynamic models formulated starting from the BTE.

The purpose of this chapter is to set up a consistent hydrodynamic model for SiNW. In particular, evolution equations for macroscopic variables like density, energy, velocity and energy-flux are obtained by taking the moments equations of the Boltzmann equation and closure relations for the higher-order fluxes as well as the production terms are deduced by using the Maximum Entropy Principle of Extended Thermodynamics.

4.1 Kinetic transport equations

In low-dimensional systems, we consider the lattice with perfectly smooth boundaries, free of impurities or other random inhomogeneities. In such ideal system the energy levels due to disorder are small, so that crystal momentum conservation is approximately preserved. In this framework, we can then construct a kinetic equation in which the distribution function evolves in time under the streaming motion of external forces and spatial gradients, and the randomizing influence of nearly point-like (in space-time) scattering events.

For the charge transport in conductors and mainly semiconductors the quantum mechanical description became an indispensable all purpose tool. For this reason, one combines the classical Boltzmann equation, which is originally reserved for diluted gasses, and quantum

mechanics to establish a semiclassical description of the charge transport in semiconductors. As concern QWRs, since the main quantum transport phenomena in SiNW transistors, at room temperature, become significant only when the longitudinal length of these devices are smaller than 10 nm [23], for longer channels, which is the case we are going to simulate, the transport of electrons in the unconstrained direction can be described with semiclassical formulations based on the 1-D Multisubband Boltzmann Transport Equation (MBTE).

As known, semiclassical transport theory is founded on the assumption that a single carrier distribution function $f(\mathbf{r}, \mathbf{k}, t)$ may be used to compute the statistical expectation value of macroscopic quantity. In this concept, the carriers are treated as independent classical particles. The dynamics of an ensemble of electrons belonging to the same energy band is a rather complicated many-body problem. For this reason a kinetic description is employed. The distribution function for the electrons in a quantum wire, with linear expansion in x -direction, depends on the x -direction in real space, the wave vector in x -direction k_x and the time t , i.e.

$$f_l^\mu = f_l^\mu(x, k_x, t),$$

for the valley μ and subband l . The MBTE reads [1]

$$\frac{\partial f_l^\mu}{\partial t} + v_\mu(k_x) \frac{\partial f_l^\mu}{\partial x} - \frac{e}{\hbar} E^{eff}(x, t, \mu, l) \frac{\partial f_l^\mu}{\partial k_x} = \sum_\eta \sum_{l'} \mathcal{C}_\eta[f_l^\mu, f_{l'}^\mu] + \sum_\eta \sum_{\mu' \neq \mu} \sum_{l'} \mathcal{C}_\eta[f_l^\mu, f_{l'}^{\mu'}] \quad (4.1)$$

where \hbar is the Planck constant divided by 2π , v_μ the electron group velocity, and E^{eff} the effective field

$$v_\mu = \frac{1}{\hbar} \frac{\partial E_l^\mu}{\partial k_x}, \quad E^{eff}(x, t, \mu, l) = \frac{1}{e} \frac{\partial \varepsilon_l^\mu}{\partial x}. \quad (4.2)$$

In the case of parabolic band we get, apart from a normalization factor for the electron mass, the classical relation between velocity and momentum:

$$v_\mu = \frac{\hbar k_x}{m_\mu^*}, \quad (4.3)$$

while in the case of the Kane dispersion relation one finds

$$v_\mu = \frac{\hbar k_x}{m_\mu^* (1 + 2\alpha \mathcal{E}(k_x))}. \quad (4.4)$$

The RHS of eq. (4.1) is the *collisional operator* representing the effects due to scattering with phonons, impurities and with other electrons. It is split into two terms modeling respectively

intravalley (with $\mu = \mu'$) and intervalley transitions (with $\mu \neq \mu'$).

The main scattering mechanisms in a semiconductor are the electron-phonon interaction, the interaction with impurities, the electron-electron scatterings and the interaction with stationary imperfections of the crystal as vacancies, external and internal crystal boundaries. In many situations the electron-electron collision term can be neglected since the electron density is not too high. However in the case of high doping, electron-electron collisions must be taken into account because they might produce sizable effects. Retaining the electron-electron collision term greatly increases the complexity of the collision operator on the RHS of the semiclassical Boltzmann equation. In fact the collision operator for the electron-electron scattering is a highly nonlinear one, being quartic in the distribution function.

In the low density approximation (not degenerate case), the collisional term for the η -th scattering rate writes

$$\mathcal{C}_\eta[f_l^\mu, f_l^{\mu'}] = \frac{L_x}{2\pi} \int dk'_x \left\{ w_\eta(k'_x, \mu', l', k_x, \mu, l) f_l^{\mu'}(x, k'_x, t) - w_\eta(k_x, \mu, l, k'_x, \mu', l') f_l^\mu(x, k_x, t) \right\}$$

where $\eta = \{ac, sr, o\}$ for the acoustic, SR, and inelastic (intravalley) scattering, $\eta = iv$ for the intervalley scattering.

4.2 The Extended Hydrodynamic model

The most advanced transport model for the simulation of SiNW is given by Non-Equilibrium Green's Function (NEGF) formalism, but it necessitates rather intensive computational efforts since it requires detailed information on the propagation of the electron wave packet injected in the device. Moreover, microscopic scattering mechanisms other than electron-phonon interactions are difficult to incorporate into the NEGF formalism because the corresponding self-energy terms are usually nonlocal functions of the spatial coordinate [20].

Another way is in the framework of quantum kinetic theory via the Wigner function, which gives the macroscopic physical quantities of interest as expectation values [6, 21]. The fundamental approach is to solve the BTE, but this is a daunting task, also from the numerical viewpoint, because it forms an integro differential system in two dimensions in phase-space and one in time, with a complicate collisional operator.

A crude approximation of the collisional operator can be obtained using the so called Relaxation Time Approximation, whose validity is limited when the scattering is elastic or isotropic (which happens for low fields) [5]. Moreover, the microscopic relaxation time is considered an adjustable parameter which is determined by fitting the solution to some

experimental or simulated data when available [22]. Hence, this parameter depends strongly on the particular set of data used for the calibration.

One of the most popular approaches is to solve the BTE in a stochastic sense by Monte Carlo (MC) methods [24, 25, 27] or by using deterministic numerical solvers [27, 26, 29]. However, the extensive computations required by both methods as well as the noisy results obtained with MC simulations, make them impractical for device design on a regular basis.

Another alternative is to obtain from the MBTE hydrodynamic models that are a good engineering-oriented approach. This can be achieved by obtaining a set of balance equations by means the so called *moment method*. The idea is to investigate only some moments of interest of the distribution function. The first step of the method is done by multiplying both sides terms of the MBTE equations by a set of k *weight functions* and integrating them in the k variation domain.

In this way, starting from the transport equation (4.1) one can obtain balance equations for macroscopic quantities associated to the flow. By multiplying the equation (4.1) by a weight function $\vec{\psi}_A(k_x)$ and integrating over $2/(2\pi)dk_x$, one finds:

$$\begin{aligned} & \frac{\partial \vec{M}_l^\mu}{\partial t} + \frac{2}{(2\pi)} \int_{\mathbb{R}} \vec{\psi}_A v_\mu \frac{\partial f_l^\mu}{\partial x} dk_x - \frac{2}{(2\pi)} \frac{e}{\hbar} E^{eff} \int_{\mathbb{R}} \vec{\psi}_A \frac{\partial f_l^\mu}{\partial k_x} dk_x = \\ & \frac{2}{(2\pi)} \sum_{\eta, l'} \int_{\mathbb{R}} \vec{\psi}_A(k_z) \mathcal{C}_\eta[f_l^\mu, f_{l'}^\mu] dk_x + \frac{2}{(2\pi)} \sum_{\eta, \mu \neq \mu', l'} \int_{\mathbb{R}} \vec{\psi}_A(k_z) \mathcal{C}_\eta[f_l^\mu, f_{l'}^{\mu'}] dk_x \end{aligned} \quad (4.5)$$

where

$$\vec{M}_l^\mu = \frac{2}{(2\pi)} \int_{\mathbb{R}} \vec{\psi}_A(k_x) f_l^\mu(x, k_x, t) dk_x \quad (4.6)$$

are the moments relative to the weight functions $\vec{\psi}_A$. By integrating by parts, and supposing that f tends to zero sufficiently fast as $k \rightarrow \infty$, we obtain

$$\begin{aligned} & \frac{\partial \vec{M}_l^\mu}{\partial t} + \frac{2}{(2\pi)} \frac{\partial}{\partial x} \int_{\mathbb{R}} \vec{\psi}_A v_\mu f_l^\mu dk_x + \frac{2}{(2\pi)} \frac{e}{\hbar} E^{eff} \int_{\mathbb{R}} f_l^\mu \frac{\partial \vec{\psi}_A(k_x)}{\partial k_x} dk_x = \\ & \frac{2}{(2\pi)} \sum_{\eta, l'} \int_{\mathbb{R}} \vec{\psi}_A(k_z) \mathcal{C}_\eta[f_l^\mu, f_{l'}^\mu] dk_x + \frac{2}{(2\pi)} \sum_{\eta, \mu \neq \mu', l'} \int_{\mathbb{R}} \vec{\psi}_A(k_z) \mathcal{C}_\eta[f_l^\mu, f_{l'}^{\mu'}] dk_x \end{aligned} \quad (4.7)$$

We have chosen a 4-moments model with

$$\vec{\psi}_A = (1, v_\mu, \mathcal{E}, \mathcal{E} v_\mu) \quad , \quad \mathcal{E} = \frac{\hbar^2 k_x^2}{2m_\mu^*} \quad , \quad v_\mu = \frac{\hbar k_x}{m_\mu^*} .$$

In this way one obtains, from eq. (4.7), the following balance equations in the unknown $(\rho_l^\mu, V_l^\mu, W_l^\mu, S_l^\mu)$

$$\frac{\partial \rho_l^\mu}{\partial t} + \frac{\partial(\rho_l^\mu V_l^\mu)}{\partial x} = \rho_l^\mu \sum_{l'} \mathcal{C}_\rho(\mu, l, \mu, l') + \rho_l^\mu \sum_{l', \mu' \neq \mu} \mathcal{C}_\rho(\mu, l, \mu', l') \quad (4.8)$$

$$\frac{\partial(\rho_l^\mu V_l^\mu)}{\partial t} + \frac{2}{m_\mu^*} \frac{\partial(\rho_l^\mu W_l^\mu)}{\partial x} + \frac{e}{m_\mu^*} \rho_l^\mu E^{eff} = \rho_l^\mu \sum_{l'} \mathcal{C}_V(\mu, l, \mu, l') + \rho_l^\mu \sum_{l', \mu' \neq \mu} \mathcal{C}_V(\mu, l, \mu', l') \quad (4.9)$$

$$\frac{\partial(\rho_l^\mu W_l^\mu)}{\partial t} + \frac{\partial(\rho_l^\mu S_l^\mu)}{\partial x} + \rho_l^\mu e E^{eff} V_l^\mu = \rho_l^\mu \sum_{l'} \mathcal{C}_W(\mu, l, \mu, l') + \rho_l^\mu \sum_{l', \mu' \neq \mu} \mathcal{C}_W(\mu, l, \mu', l') \quad (4.10)$$

$$\frac{\partial(\rho_l^\mu S_l^\mu)}{\partial t} + \frac{\partial(\rho_l^\mu F_l^\mu)}{\partial x} + 3 \frac{e}{m_\mu^*} \rho_l^\mu E^{eff} W_l^\mu = \rho_l^\mu \sum_{l'} \mathcal{C}_S(\mu, l, \mu, l') + \rho_l^\mu \sum_{l', \mu' \neq \mu} \mathcal{C}_S(\mu, l, \mu', l') \quad (4.11)$$

where

$$\rho_l^\mu = \frac{2}{(2\pi)} \int_{\mathbb{R}} f_l^\mu(x, k_x, t) dk_x \quad \text{linear electron density,} \quad (4.12)$$

$$V_l^\mu = \frac{2}{(2\pi)} \frac{1}{\rho_l^\mu} \int_{\mathbb{R}} f_l^\mu(x, k_x, t) v_\mu dk_x \quad \text{linear electron velocity,} \quad (4.13)$$

$$W_l^\mu = \frac{2}{(2\pi)} \frac{1}{\rho_l^\mu} \int_{\mathbb{R}} f_l^\mu(x, k_x, t) \mathcal{E} dk_x \quad \text{linear electron energy,} \quad (4.14)$$

$$S_l^\mu = \frac{2}{(2\pi)} \frac{1}{\rho_l^\mu} \int_{\mathbb{R}} f_l^\mu(x, k_x, t) \mathcal{E} v_\mu dk_x \quad \text{linear electron energy flux,} \quad (4.15)$$

$$F_l^\mu = \frac{2}{(2\pi)} \frac{1}{\rho_l^\mu} \int_{\mathbb{R}} f_l^\mu(x, k_x, t) v_\mu^2 \mathcal{E} dk_x \quad \text{flux of electron energy flux,} \quad (4.16)$$

while

$$\mathcal{E}_\rho(\mu, l, \mu', l') = \frac{2}{(2\pi)} \frac{1}{\rho_l^\mu} \int_{\mathbb{R}} \mathcal{E}_\eta[f_l^\mu, f_{l'}^{\mu'}] dk_x, \quad (4.17)$$

$$\mathcal{E}_V(\mu, l, \mu', l') = \frac{2}{(2\pi)} \frac{1}{\rho_l^\mu} \int_{\mathbb{R}} \mathcal{E}_\eta[f_l^\mu, f_{l'}^{\mu'}] v_\mu dk_x, \quad (4.18)$$

$$\mathcal{E}_W(\mu, l, \mu', l') = \frac{2}{(2\pi)} \frac{1}{\rho_l^\mu} \int_{\mathbb{R}} \mathcal{E}_\eta[f_l^\mu, f_{l'}^{\mu'}] \mathcal{E} dk_x, \quad (4.19)$$

$$\mathcal{E}_S(\mu, l, \mu', l') = \frac{2}{(2\pi)} \frac{1}{\rho_l^\mu} \int_{\mathbb{R}} \mathcal{E}_\eta[f_l^\mu, f_{l'}^{\mu'}] \mathcal{E} v_\mu dk_x \quad (4.20)$$

are the moments of the collision term.

In the previous expressions $\eta = \{ac, sr, o\}$ with $\mu = \mu'$ for intravalley scattering, $\eta = iv$ with $\mu \neq \mu'$ for intervalley scattering.

4.3 Maximum Entropy Principle

The PDEs system (4.8)-(4.11) is of hyperbolic type and it is not closed because the number of unknowns exceeds the number of equations. Therefore closure relations must be introduced. The closure problem consists in finding constitutive relations in terms of the fundamental variables for the extra fluxes and the production terms.

The determination and validity of the closure relations just in the 3D bulk case, have given rise a large debate during these years (see [30] for an overview), especially for the description of the hot-carrier effects. In this context, the production terms have been usually approximated with macroscopic relaxation terms, where a separate macroscopic relaxation time is introduced for every moment of the scattering operator. The key point is the determination of these relaxation times, which can be obtained or by fitting with homogeneous field measurements (when available) or MC simulations. As these parameters are extracted from homogeneous data, their validity for realistic devices is still an open issue. Regarding to the higher-order moments, they have been determined or by heuristic considerations or by suitable assumptions on the distribution function, which need a fitting with MC data.

Another way to tackle these problems is by means of the Maximum Entropy Principle of Extended Thermodynamics [31–33], in which the distribution function used to calculate the higher-order moments and the production terms is assumed to be that which maximizes the entropy under the constraints of the given set of moments.

The MEP leads to a systematic way for obtaining constitutive relations on the basis of the *information theory* [59, 60], as already proved successfully for 2D nanoscale structures

[34, 35], and for simulating the 3D electron transport in sub-micrometric devices, in the case in which the lattice is a thermal bath with constant temperature [36–39] or when the phonons are off-equilibrium [40–43].

Recently, a hydrodynamic modeling for silicon quantum wires has been developed and for a review the reader is referred to [44–46].

We underline that the distribution function obtained with the MEP is an approximation of the real one but, from the other side, this distribution is useful to determine analytically without any fitting procedure the higher-order moments and the production terms. In this way a consistent model with a physical basis is obtained, whose validity must be assessed with experimental data or MC simulations.

In a semiconductor electrons interact with phonons describing the thermal vibrations of the ions placed at the points of the crystal lattice. We assume that the electron gas is sufficiently dilute, then the entropy density can be taken as the classical limit of the expression arising in the Fermi statistics, i.e.

$$S_e(\mu, l) = -\frac{2}{(2\pi)}k_B \sum_{\mu, l} |\chi_l^\mu(y, z, t)|^2 \int_{\mathbb{R}} (f_l^\mu \log f_l^\mu - f_l^\mu) dk_x. \quad (4.21)$$

The proposed expression of the entropy combines quantum effects and semiclassical transport along the longitudinal direction, by weighting the contribution of each f_l^μ with the square modulus of the $\chi_l^\mu(y, z, t)$ arising from the Schrödinger-Poisson subsystem. According to the MEP, if a given number of moments $M_A(\mu, l)$ are known, the distribution functions \hat{f}_l^μ , which can be used to evaluate the unknown moments, correspond to the extremum of the total entropy density under the constraint that they yield the known moments, i.e.

$$\frac{2}{(2\pi)} \int_{\mathbb{R}} \psi_A(k_x) \hat{f}_l^\mu dk_x = M_A(\mu, l). \quad (4.22)$$

If we introduce a set of Lagrange multipliers λ_A , the problem to maximize S_e under the constraints (4.22) is equivalent to maximize

$$S' = S_e - \sum_{\mu, l} \sum_A \lambda_A |\chi_l^\mu(y, z, t)|^2 \left[\frac{2}{(2\pi)} \int_{\mathbb{R}} \psi_A \hat{f}_l^\mu dk_x - M_A(\mu, l) \right]. \quad (4.23)$$

So doing we shall obtain the following distribution function:

$$\hat{f}_l^\mu = \exp(-\Sigma) \quad , \quad \Sigma = \frac{1}{k_B} \sum_A \psi_A \lambda_A \quad (4.24)$$

$$\psi_A = (1, v_\mu, \mathcal{E}, \mathcal{E}v_\mu) \quad , \quad \lambda_A = (\lambda_l^\mu, k_B \lambda_{lV}^\mu, k_B \lambda_{lW}^\mu, k_B \lambda_{lS}^\mu) \quad (4.25)$$

By inserting the previous equations in (4.22), we obtain

$$M_A = M_A(\lambda_A) \quad (4.26)$$

which define implicitly the Lagrange multipliers. In order to invert the above relations, we shall perform an expansion around the local thermal equilibrium. In fact, at local equilibrium, \hat{f} must reduce to the Maxwellian. This means

$$\lambda_{lV}^\mu|_E = \lambda_{lS}^\mu|_E = 0, \quad \lambda_{lW}^\mu|_E = \frac{1}{k_B T_L}. \quad (4.27)$$

Then we consider the vanishing Lagrange multipliers of higher order respect to equilibrium, by introducing the smallness parameter τ :

$$\lambda_{lV}^\mu = \tau \hat{\lambda}_{lV}^\mu \quad , \quad \lambda_{lS}^\mu = \tau \hat{\lambda}_{lS}^\mu \quad . \quad (4.28)$$

The inversion problem (4.26) has been tackled for the first time in [55] obtaining, up to the first order in τ (for simplicity we shall omit the indexes μ, l):

$$\hat{f} = \exp\left(-\frac{\lambda}{k_B} - \lambda_W \mathcal{E}\right) \left\{ 1 - \tau \left(\hat{\lambda}_{lV} v + \hat{\lambda}_{lS} v \mathcal{E} \right) \right\} + \mathcal{O}(\tau^2) \quad . \quad (4.29)$$

The Lagrange multipliers are determined by imposing the constraint (4.22)

$$\frac{\lambda_l^\mu}{k_B} = -\log \frac{\rho_l^\mu \hbar \pi^{\frac{1}{2}}}{\sqrt{4m_\mu^* W_l^\mu}} \quad , \quad \lambda_{lW}^\mu = \frac{1}{2W_l^\mu} \quad (4.30)$$

$$\hat{\lambda}_{lV}^\mu = -\frac{5m_\mu^*}{4\tau W_l^\mu} V_l^\mu + \frac{m_\mu^*}{4\tau (W_l^\mu)^2} S_l^\mu \quad , \quad \hat{\lambda}_{lS}^\mu = \frac{m_\mu^*}{4\tau (W_l^\mu)^2} V_l^\mu a - \frac{m_\mu^*}{12\tau (W_l^\mu)^3} S_l^\mu \quad (4.31)$$

whereas the higher order flux is

$$F_l^\mu = \frac{6(W_l^\mu)^2}{m_\mu^*} \quad . \quad (4.32)$$

4.4 Closure relations for the production terms

In order to close the system we need functional relations for the production terms, which can be evaluated by using the MEP distribution function (4.29).

Closure for the electron number production

$$\mathcal{C}_\rho(\mu, l, \mu, l') = \mathcal{C}_\rho(\mu, l, \mu, l')(ac) + \mathcal{C}_\rho(\mu, l, \mu, l')(sr) + \mathcal{C}_\rho(\mu, l, \mu, l')(o) \quad (4.33)$$

where

$$\mathcal{C}_\rho(\mu, l, \mu, l')(\eta) = \frac{2}{(2\pi)} \int_{\mathbb{R}} \mathcal{C}_\eta[f_l^\mu, f_{l'}^\mu] dk_x \quad , \quad \eta = \{ac, sr, o\} \quad (4.34)$$

and

$$\mathcal{C}_\rho(\mu, l, \mu', l')(iv) = \frac{2}{(2\pi)} \int_{\mathbb{R}} \mathcal{C}_{iv}[f_l^\mu, f_{l'}^{\mu'}] dk_x \quad (4.35)$$

Evaluation of $\mathcal{C}_\rho(\mu, l, \mu, l')(o)$

This is an intravalley inelastic scattering mechanism, where the scattering rate is given by eq. (3.12). After long calculations, one obtains

$$\begin{aligned} \rho_l^\mu C_\rho(\mu, l, \mu, l')(o) = & \frac{s_{op}}{\pi} \frac{L_x}{2\pi} \left\{ g_0 G_{l'l}^{\mu\mu} A_{1l'l}^{+\mu\mu}(\Delta_{l'l}^{+\mu\mu}) + (g_0 + 1) G_{l'l}^{\mu\mu} A_{1l'l}^{-\mu\mu}(\Delta_{l'l}^{-\mu\mu}) - \right. \\ & \left. g_0 G_{l'l}^{\mu\mu} A_{2l'l}^{-\mu\mu}(\Delta_{l'l}^{-\mu\mu}) - (g_0 + 1) G_{l'l}^{\mu\mu} A_{2l'l}^{+\mu\mu}(\Delta_{l'l}^{+\mu\mu}) \right\} \quad (4.36) \end{aligned}$$

where

$$A_{1l'l}^{\pm\mu\mu}(\Delta) = \rho_{l'}^\mu \sqrt{\frac{2\pi}{W_{l'}^\mu}} \exp\left(\frac{\Delta}{2W_{l'}^\mu}\right) \int_0^{+\infty} \frac{H\left(\frac{\hbar^2(k_x)^2}{2m_\mu^*} - \Delta\right)}{\sqrt{\frac{\hbar^2 k_x^2}{2m_\mu^*} - \Delta}} \exp\left(-\frac{\hbar^2 k_x^2}{4m_\mu^* W_{l'}^\mu}\right) dk_x \quad (4.37)$$

$$A_{2l'l}^{\pm\mu\mu}(\Delta) = \rho_l^\mu \sqrt{\frac{2\pi}{W_l^\mu}} \int_0^{+\infty} \frac{H\left(\frac{\hbar^2(k_x)^2}{2m_\mu^*} - \Delta\right)}{\sqrt{\frac{\hbar^2(k_x)^2}{2m_\mu^*} - \Delta}} \exp\left(-\frac{\hbar^2 k_x^2}{4m_\mu^* W_l^\mu}\right) dk_x \quad (4.38)$$

and

$$\Delta_{l'l}^{\pm\mu\mu} = \varepsilon_{l'}^\mu - \varepsilon_l^\mu \pm \hbar\omega_0. \quad (4.39)$$

Evaluation of $\mathcal{C}_\rho(\mu, l, \mu, l')(ac)$

This is an intravalley elastic scattering mechanism, where the scattering rate is given by eq. (3.18). We obtain

$$\rho_l^\mu C_\rho(\mu, l, \mu, l')(ac) = \frac{s_{ac}}{\pi} \frac{L_x}{2\pi} \left\{ G_{l'l}^{\mu\mu} J_{1l'l}^{\mu\mu} - G_{l'l}^{\mu\mu} J_{2l'l}^{\mu\mu} \right\} \quad (4.40)$$

where

$$J_{1'l'}^{\mu\mu} = \rho_{l'}^{\mu} \sqrt{\frac{2\pi}{W_{l'}^{\mu}}} \exp\left(\frac{\Delta_{l'l'}^{\mu\mu}}{2W_{l'}^{\mu}}\right) \int_0^{+\infty} \frac{H\left(\frac{\hbar^2(k_x)^2}{2m_{\mu}^*} - \Delta_{l'l'}^{\mu\mu}\right)}{\sqrt{\frac{\hbar^2 k_x^2}{2m_{\mu}^*} - \Delta_{l'l'}^{\mu\mu}}} \exp\left(-\frac{\hbar^2 k_x^2}{4m_{\mu}^* W_{l'}^{\mu}}\right) dk_x \quad (4.41)$$

$$J_{2l'l'}^{\mu\mu} = \rho_l^{\mu} \sqrt{\frac{2\pi}{W_l^{\mu}}} \int_0^{+\infty} \frac{H\left(\frac{\hbar^2(k_x)^2}{2m_{\mu}^*} - \Delta_{l'l'}^{\mu\mu}\right)}{\sqrt{\frac{\hbar^2(k_x)^2}{2m_{\mu}^*} - \Delta_{l'l'}^{\mu\mu}}} \exp\left(-\frac{\hbar^2 k_x^2}{4m_{\mu}^* W_l^{\mu}}\right) dk_x \quad (4.42)$$

and

$$\Delta_{l'l'}^{\mu\mu} = \varepsilon_{l'}^{\mu} - \varepsilon_l^{\mu}. \quad (4.43)$$

Evaluation of $\mathcal{C}_{\rho}(\mu, l, \mu, l')(sr)$

This is an intravalley elastic scattering mechanism, where the scattering rate is given by eq. (3.32). We get

$$\rho_l^{\mu} \mathcal{C}_{\rho}(\mu, l, \mu, l')(sr) = \frac{4e^2 \lambda_{sr} \Delta_{sr}^2 \sqrt{m_{\mu}^*}}{\hbar^2 \sqrt{2\pi W_l^{\mu}}} \times \{ |\mathcal{F}_{l'l'}^{\mu\mu}|^2 \rho_{l'}^{\mu} [I_s^-(\Delta_{l'l'}^{\mu\mu}, W_{l'}^{\mu}) + I_s^+(\Delta_{l'l'}^{\mu\mu}, W_{l'}^{\mu})] - |\mathcal{F}_{l'l'}^{\mu\mu}|^2 \rho_l^{\mu} [I_s^-(\Delta_{l'l'}^{\mu\mu}, W_l^{\mu}) + I_s^+(\Delta_{l'l'}^{\mu\mu}, W_l^{\mu})] \} \quad (4.44)$$

where

$$I_s^{\pm}(\Delta_{l'l'}^{\mu\mu}, W_l^{\mu}) = \int_0^{+\infty} \frac{H\left(\mathcal{E} + \Delta_{l'l'}^{\mu\mu}\right)}{\frac{2m_{\mu}^* \lambda_{sr}^2}{\hbar^2} \left[\sqrt{\mathcal{E}} \pm \sqrt{\mathcal{E} + \Delta_{l'l'}^{\mu\mu}}\right]^2 + 2} \frac{\exp\left(-\frac{\mathcal{E}}{2m_{\mu}^* W_l^{\mu}}\right)}{\sqrt{\mathcal{E}[\mathcal{E} + \Delta_{l'l'}^{\mu\mu}]}} d\mathcal{E} \quad (4.45)$$

Evaluation of $\mathcal{C}_{\rho}(\mu, l, \mu', l')(iv)$

This is an **intervalley inelastic** scattering, where the scattering rate is given by eq. (6.23). The result is similar to the eq. (4.36) (obtained for an intravalley, inelastic scattering) with $\mu \neq \mu'$ but supposing to change eq. (4.39) into

$$\tilde{\Delta}_{l'l'}^{\pm\mu\mu'} = \varepsilon_{l'}^{\mu'} - \varepsilon_l^{\mu} \pm \hbar\omega_{iv} + \Delta_{\mu'\mu} \quad (4.46)$$

where $\Delta_{\mu\mu'}$ is given in eq. (6.23). Then we obtain

$$\rho_l^\mu C_\rho(\mu, l, \mu', l')(iv) = \frac{s_{iv} L_x}{\pi 2\pi} \left\{ g_0 G_{l'l}^{\mu'\mu} A_{1'l}^{+\mu'\mu} (\tilde{\Delta}_{l'l}^{+\mu\mu'}) + (g_0 + 1) G_{l'l}^{\mu'\mu} A_{1'l}^{-\mu'\mu} (\tilde{\Delta}_{l'l}^{-\mu\mu'}) - g_0 G_{l'l}^{\mu\mu'} A_{2l'l}^{-\mu\mu'} (\Delta_{l'l}^{-\mu\mu'}) - (g_0 + 1) G_{l'l}^{\mu\mu'} A_{2l'l}^{+\mu\mu'} (\tilde{\Delta}_{l'l}^{+\mu\mu'}) \right\} \quad (4.47)$$

$$A_{1'l}^{\pm\mu'\mu}(\Delta) = \rho_l^{\mu'} \sqrt{\frac{2\pi}{W_{l'}^{\mu'}}} \exp\left(\frac{\Delta}{2W_{l'}^{\mu'}}\right) \int_0^{+\infty} \frac{H\left(\frac{\hbar^2(k_x)^2}{2m_{\mu'}^*} - \Delta\right)}{\sqrt{\frac{\hbar^2 k_x^2}{2m_{\mu'}^*} - \Delta}} \exp\left(-\frac{\hbar^2 k_x^2}{4m_{\mu'}^* W_{l'}^{\mu'}}\right) dk_x$$

$$A_{2l'l}^{\pm\mu\mu'}(\Delta) = \rho_l^\mu \sqrt{\frac{2\pi}{W_l^\mu}} \int_0^{+\infty} \frac{H\left(\frac{\hbar^2(k_x)^2}{2m_\mu^*} - \Delta\right)}{\sqrt{\frac{\hbar^2(k_x)^2}{2m_\mu^*} - \Delta}} \exp\left(-\frac{\hbar^2 k_x^2}{4m_\mu^* W_l^\mu}\right) dk_x$$

Closure for the production of electron energy

$$\mathcal{E}_W(\mu, l, \mu, l') = \mathcal{E}_W(\mu, l, \mu, l')(ac) + \mathcal{E}_W(\mu, l, \mu, l')(sr) + \mathcal{E}_W(\mu, l, \mu, l')(o) \quad (4.48)$$

where

$$\mathcal{E}_W(\mu, l, \mu, l')(\eta) = \frac{2}{(2\pi)} \int_{\mathbb{R}} \mathcal{E} \mathcal{E}_\eta [f_l^\mu, f_{l'}^{\mu'}] dk_x \quad , \quad \eta = \{ac, sr, o\} \quad (4.49)$$

and

$$\mathcal{E}_W(\mu, l, \mu', l')(iv) = \frac{2}{(2\pi)} \int_{\mathbb{R}} \mathcal{E} \mathcal{E}_{iv} [f_l^\mu, f_{l'}^{\mu'}] dk_x \quad (4.50)$$

We observe that, with respect to eqs. (4.34)-(4.35), there is an extra \mathcal{E} , and by multiplying all the previous integrals by \mathcal{E} , similar results hold.

Closure for the production of electron crystal momentum

$$\mathcal{E}_V(\mu, l, \mu, l') = \mathcal{E}_V(\mu, l, \mu, l')(ac) + \mathcal{E}_V(\mu, l, \mu, l')(sr) + \mathcal{E}_V(\mu, l, \mu, l')(o) \quad (4.51)$$

where

$$\mathcal{E}_V(\mu, l, \mu, l')(\eta) = \frac{2}{(2\pi)} \int_{\mathbb{R}} \frac{\hbar k_x}{m_\mu^*} \mathcal{E}_\eta [f_l^\mu, f_{l'}^{\mu'}] dk_x \quad , \quad \eta = \{ac, sr, o\} \quad (4.52)$$

and

$$\mathcal{E}_V(\mu, l, \mu', l')(iv) = \frac{2}{(2\pi)} \int_{\mathbb{R}} \frac{\hbar k_x}{m_\mu^*} \mathcal{E}_{iv} [f_l^\mu, f_{l'}^{\mu'}] dk_x \quad (4.53)$$

Evaluation of $\mathcal{C}_V(\mu, l, \mu, l')(o)$

For this production term, the scattering rate is given by eq. (3.12). We get

$$\rho_l^\mu \mathcal{C}_V(\mu, l, \mu, l')(o) = \Omega_{1l'l'}^{\mu\mu'}(W_l^\mu) \rho_l^\mu V_l^\mu + \Omega_{2l'l'}^{\mu\mu'}(W_l^\mu) \rho_l^\mu S_l^\mu \quad (4.54)$$

where

$$\Omega_{1l'l'}^{\mu\mu'}(W_l^\mu) = \frac{s_{op}}{\pi} \frac{L_x}{2\pi} \hbar G_{l'l'}^{\mu\mu} \left[-\frac{5}{4W_l^\mu} (I_{Vl'l'}^{-\mu\mu} + I_{Vl'l'}^{+\mu\mu}) + \frac{1}{4(W_l^\mu)^2} (I_{Sl'l'}^{-\mu\mu} + I_{Sl'l'}^{+\mu\mu}) \right] \quad (4.55)$$

$$\Omega_{2l'l'}^{\mu\mu'}(W_l^\mu) = \frac{s_{op}}{\pi} \frac{L_x}{2\pi} \hbar G_{l'l'}^{\mu\mu} \left[\frac{1}{4(W_l^\mu)^2} (I_{Vl'l'}^{-\mu\mu} + I_{Vl'l'}^{+\mu\mu}) - \frac{1}{12(W_l^\mu)^3} (I_{Sl'l'}^{-\mu\mu} + I_{Sl'l'}^{+\mu\mu}) \right] \quad (4.56)$$

$$I_{Vl'l'}^{\pm\mu\mu} = \frac{\hbar}{m_\mu^*} \sqrt{\frac{2\pi}{W_l^\mu}} \left(g_0 + \frac{1}{2} \pm \frac{1}{2} \right) \int_0^{+\infty} k_x^2 \frac{H\left(\frac{\hbar^2(k_x)^2}{2m_\mu^*} - \Delta_{l'l'}^{\pm\mu\mu}\right)}{\sqrt{\frac{\hbar^2(k_x)^2}{2m_\mu^*} - \Delta_{l'l'}^{\pm\mu\mu}}} \exp\left(-\frac{\hbar^2 k_x^2}{4m_\mu^* W_l^\mu}\right) dk_x$$

$$I_{Sl'l'}^{\pm\mu\mu} = \frac{\hbar^3}{2m_\mu^{*2}} \sqrt{\frac{2\pi}{W_l^\mu}} \left(g_0 + \frac{1}{2} \pm \frac{1}{2} \right) \int_0^{+\infty} k_x^4 \frac{H\left(\frac{\hbar^2(k_x)^2}{2m_\mu^*} - \Delta_{l'l'}^{\pm\mu\mu}\right)}{\sqrt{\frac{\hbar^2(k_x)^2}{2m_\mu^*} - \Delta_{l'l'}^{\pm\mu\mu}}} \exp\left(-\frac{\hbar^2 k_x^2}{4m_\mu^* W_l^\mu}\right) dk_x$$

Evaluation of $\mathcal{C}_V(\mu, l, \mu, l')(ac)$

This is an intravalley inelastic scattering process, where the scattering rate is given by eq. (3.18). We get

$$\rho_l^\mu \mathcal{C}_V(\mu, l, \mu, l')(ac) = \Delta_{1l'l'}^{\mu\mu'}(W_l^\mu) \rho_l^\mu V_l^\mu + \Delta_{2l'l'}^{\mu\mu'}(W_l^\mu) \rho_l^\mu S_l^\mu \quad (4.57)$$

where

$$\Delta_{1l'l'}^{\mu\mu'}(W_l^\mu) = \frac{s_{ac}}{\pi} \frac{\hbar L_x}{2\pi W_l^\mu} G_{l'l'}^{\mu\mu} \left[-\frac{5}{4} F_{l'l'}^{\mu\mu} + \frac{1}{4W_l^\mu} L_{l'l'}^{\mu\mu} \right] \quad (4.58)$$

$$\Delta_{2l'l'}^{\mu\mu'}(W_l^\mu) = \frac{s_{ac}}{\pi} \frac{\hbar L_x}{2\pi W_l^\mu} G_{l'l'}^{\mu\mu} \left[\frac{1}{4W_l^\mu} F_{l'l'}^{\mu\mu} - \frac{1}{12(W_l^\mu)^2} L_{l'l'}^{\mu\mu} \right] \quad (4.59)$$

$$F_{l'l'}^{\mu\mu'}(W_l^\mu) = \sqrt{\frac{2\pi}{W_l^\mu}} \int_0^{+\infty} \frac{H\left(\frac{\hbar^2(k_x)^2}{2m_\mu^*} - \Delta_{l'l'}^{\mu\mu}\right)}{\sqrt{\frac{\hbar^2(k_x)^2}{2m_\mu^*} - \Delta_{l'l'}^{\mu\mu}}} \exp\left(-\frac{\hbar^2 k_x^2}{4m_\mu^* W_l^\mu}\right) \frac{\hbar k_x^2}{m_\mu^*} dk_x \quad (4.60)$$

$$L_{ll'}^{\mu\mu}(W_l^\mu) = \sqrt{\frac{2\pi}{W_l^\mu}} \int_0^{+\infty} \frac{H\left(\frac{\hbar^2(k_x)^2}{2m_\mu^*} - \Delta_{ll'}^{\mu\mu}\right)}{\sqrt{\frac{\hbar^2(k_x)^2}{2m_\mu^*} - \Delta_{ll'}^{\mu\mu}}} \exp\left(-\frac{\hbar^2 k_x^2}{4m_\mu^* W_l^\mu}\right) \frac{\hbar^3 k_z^4}{2m_\mu^{*2}} dk_x \quad (4.61)$$

Evaluation of $\mathcal{C}_V(\mu, l, \mu, l')(sr)$

This is an intravalley elastic scattering process, and from eqs. (3.32) we get

$$\begin{aligned} \mathcal{C}_V(\mu, l, \mu, l')(sr) = & -\frac{\sqrt{m_\mu^*} e^2 \lambda_{sr} \Delta_{sr}^2}{6\hbar^2 \pi (W_l^\mu)^5} |\mathcal{F}_{ll'}^{\mu\mu}|^2 [\Omega_V V_l^\mu + \Omega_S S_l^\mu] - \\ & -\frac{\sqrt{m_\mu^*} e^2 \lambda_{sr} \Delta_{sr}^2}{6\hbar^2 \pi (W_{l'}^\mu)^5} |\mathcal{F}_{l'l}^{\mu\mu}|^2 [\tilde{\Omega}_V V_{l'}^\mu + \tilde{\Omega}_S S_{l'}^\mu] \end{aligned} \quad (4.62)$$

where

$$\begin{aligned} \Omega_V = & \frac{15}{8} \frac{\sqrt{\pi}}{(2W_l^\mu)^{\frac{7}{2}}} \left[I_{S_2}^-(\Delta_{ll'}^{\mu\mu}, W_l^\mu, j=0) + I_{S_2}^+(\Delta_{ll'}^{\mu\mu}, W_l^\mu, j=0) \right] - \\ & \frac{3}{4} \frac{\sqrt{\pi}}{(2W_l^\mu)^{\frac{5}{2}}} \left[I_{S_2}^-(\Delta_{ll'}^{\mu\mu}, W_l^\mu, j=1) + I_{S_2}^+(\Delta_{ll'}^{\mu\mu}, W_l^\mu, j=1) \right] \end{aligned} \quad (4.63)$$

$$\begin{aligned} \tilde{\Omega}_V = & \frac{15}{8} \frac{\sqrt{\pi}}{(2W_{l'}^\mu)^{\frac{7}{2}}} \left[-\tilde{I}_{S_2}^-(\Delta_{l'l}^{\mu\mu}, W_{l'}^\mu, j=0) + \tilde{I}_{S_2}^+(\Delta_{l'l}^{\mu\mu}, W_{l'}^\mu, j=0) \right] - \\ & \frac{3}{4} \frac{\sqrt{\pi}}{(2W_{l'}^\mu)^{\frac{5}{2}}} \left[-\tilde{I}_{S_2}^-(\Delta_{l'l}^{\mu\mu}, W_{l'}^\mu, j=1) + \tilde{I}_{S_2}^+(\Delta_{l'l}^{\mu\mu}, W_{l'}^\mu, j=1) \right] \end{aligned} \quad (4.64)$$

$$\begin{aligned} \Omega_S = & -\frac{3}{4} \frac{\sqrt{\pi}}{(2W_l^\mu)^{\frac{5}{2}}} \left[I_{S_2}^-(\Delta_{ll'}^{\mu\mu}, W_l^\mu, j=0) + I_{S_2}^+(\Delta_{ll'}^{\mu\mu}, W_l^\mu, j=0) \right] + \\ & \frac{\sqrt{\pi}}{2(2W_l^\mu)^{\frac{3}{2}}} \left[I_{S_2}^-(\Delta_{ll'}^{\mu\mu}, W_l^\mu, j=1) + I_{S_2}^+(\Delta_{ll'}^{\mu\mu}, W_l^\mu, j=1) \right] \end{aligned} \quad (4.65)$$

$$\begin{aligned} \tilde{\Omega}_S = & -\frac{3}{4} \frac{\sqrt{\pi}}{(2W_{l'}^\mu)^{\frac{5}{2}}} \left[-\tilde{I}_{S_2}^-(\Delta_{l'l}^{\mu\mu}, W_{l'}^\mu, j=0) + \tilde{I}_{S_2}^+(\Delta_{l'l}^{\mu\mu}, W_{l'}^\mu, j=0) \right] + \\ & \frac{\sqrt{\pi}}{2(2W_{l'}^\mu)^{\frac{3}{2}}} \left[-\tilde{I}_{S_2}^-(\Delta_{l'l}^{\mu\mu}, W_{l'}^\mu, j=1) + \tilde{I}_{S_2}^+(\Delta_{l'l}^{\mu\mu}, W_{l'}^\mu, j=1) \right] \end{aligned} \quad (4.66)$$

$$I_{S_2}^{\pm}(\Delta_{ll'}^{\mu\mu}, W_l^{\mu}, j) = \int_0^{+\infty} \frac{\mathcal{E}^{j+\frac{1}{2}} H(\mathcal{E} - \Delta_{ll'}^{\mu\mu})}{\frac{2m_{\mu}^* \lambda_{sr}^2}{\hbar^2} \left[\sqrt{\mathcal{E}} \pm \sqrt{\mathcal{E} - \Delta_{ll'}^{\mu\mu}} \right]^2 + 2} \frac{\exp\left(-\frac{\mathcal{E}}{2m_{\mu}^* W_l^{\mu}}\right)}{\sqrt{\mathcal{E} - \Delta_{ll'}^{\mu\mu}}} d\mathcal{E} \quad (4.67)$$

$$\tilde{I}_{S_2}^{\pm}(\Delta_{ll'}^{\mu\mu}, W_{l'}^{\mu}, j) = \int_0^{+\infty} \frac{\mathcal{E}^j H(\mathcal{E} - \Delta_{ll'}^{\mu\mu})}{\frac{2m_{\mu}^* \lambda_{sr}^2}{\hbar^2} \left[\sqrt{\mathcal{E}} \pm \sqrt{\mathcal{E} - \Delta_{ll'}^{\mu\mu}} \right]^2 + 2} \frac{\exp\left(-\frac{\mathcal{E}}{2m_{\mu}^* W_{l'}^{\mu}}\right)}{\sqrt{\mathcal{E} - \Delta_{ll'}^{\mu\mu}}} d\mathcal{E} \quad (4.68)$$

Evaluation of $\mathcal{C}_V(\mu, l, \mu', l')(iv)$

This term is similar to the eq. (4.54) (obtained for an intravalley inelastic scattering) but with $\mu \neq \mu'$ and supposing to change eq. (4.39) into

$$\tilde{\Delta}_{ll'}^{\pm\mu\mu'} = \varepsilon_{l'}^{\mu'} - \varepsilon_l^{\mu} \pm \hbar\omega_{iv} + \Delta_{\mu'\mu} \quad (4.69)$$

where $\Delta_{\mu\mu'}$ is given in eq. (6.23), we obtain

$$\rho_l^{\mu} C_V(\mu, l, \mu', l')(iv) = \Omega_{1l'}^{\mu\mu'}(W_l^{\mu}) \rho_l^{\mu} V_l^{\mu} + \Omega_{2l'}^{\mu\mu'}(W_l^{\mu}) \rho_l^{\mu} S_l^{\mu} \quad (4.70)$$

where

$$\Omega_{1l'}^{\mu\mu'}(W_l^{\mu}) = \frac{s_{op}}{\pi} \frac{L_x}{2\pi} \hbar G_{ll'}^{\mu\mu'} \left[-\frac{5}{4W_l^{\mu}} (I_{Vl'}^{-\mu\mu'} + I_{Vl'}^{+\mu\mu'}) + \frac{1}{4(W_l^{\mu})^2} (I_{Sl'}^{-\mu\mu'} + I_{Sl'}^{+\mu\mu'}) \right] \quad (4.71)$$

$$\Omega_{2l'}^{\mu\mu'}(W_l^{\mu}) = \frac{s_{op}}{\pi} \frac{L_x}{2\pi} \hbar G_{ll'}^{\mu\mu'} \left[\frac{1}{4(W_l^{\mu})^2} (I_{Vl'}^{-\mu\mu'} + I_{Vl'}^{+\mu\mu'}) - \frac{1}{12(W_l^{\mu})^3} (I_{Sl'}^{-\mu\mu'} + I_{Sl'}^{+\mu\mu'}) \right] \quad (4.72)$$

$$I_{Vl'}^{\pm\mu\mu'} = \frac{\hbar}{m_{\mu}^*} \sqrt{\frac{2\pi}{W_l^{\mu}}} \left(g_0 + \frac{1}{2} \pm \frac{1}{2} \right) \int_0^{+\infty} k_x^2 \frac{H\left(\frac{\hbar^2(k_x)^2}{2m_{\mu}^*} - \Delta_{ll'}^{\pm\mu\mu'}\right)}{\sqrt{\frac{\hbar^2(k_x)^2}{2m_{\mu}^*} - \Delta_{ll'}^{\pm\mu\mu'}}} \exp\left(-\frac{\hbar^2 k_x^2}{4m_{\mu}^* W_l^{\mu}}\right) dk_x$$

$$I_{Sl'}^{\pm\mu\mu'} = \frac{\hbar^3}{2m_{\mu}^*{}^2} \sqrt{\frac{2\pi}{W_l^{\mu}}} \left(g_0 + \frac{1}{2} \pm \frac{1}{2} \right) \int_0^{+\infty} k_x^4 \frac{H\left(\frac{\hbar^2(k_x)^2}{2m_{\mu}^*} - \Delta_{ll'}^{\pm\mu\mu'}\right)}{\sqrt{\frac{\hbar^2(k_x)^2}{2m_{\mu}^*} - \Delta_{ll'}^{\pm\mu\mu'}}} \exp\left(-\frac{\hbar^2 k_x^2}{4m_{\mu}^* W_l^{\mu}}\right) dk_x$$

Closure for the production of electron energy-flux

$$\mathcal{C}_S(\mu, l, \mu, l') = \mathcal{C}_S(\mu, l, \mu, l')(ac) + \mathcal{C}_S(\mu, l, \mu, l')(sr) + \mathcal{C}_S(\mu, l, \mu, l')(o) \quad (4.73)$$

where

$$\mathcal{C}_S(\mu, l, \mu, l')(\eta) = \frac{2}{(2\pi)} \int_{\mathbb{R}} v_{\mu} \mathcal{E} \mathcal{C}_{\eta}[f_l^{\mu}, f_{l'}^{\mu}] dk_x \quad , \quad \eta = \{ac, sr, o\} \quad (4.74)$$

and

$$\mathcal{C}_S(\mu, l, \mu', l')(iv) = \frac{2}{(2\pi)} \int_{\mathbb{R}} v_{\mu} \mathcal{E} \mathcal{C}_{iv}[f_l^{\mu}, f_{l'}^{\mu'}] dk_x \quad (4.75)$$

We observe that, with respect to eqs. (4.52)-(4.53), there is an extra \mathcal{E} , and by multiplying all the previous integrals by \mathcal{E} , similar results hold.

Chapter 5

Electron transport in infinitely deep SiNW having different cross-sections

5.1 Introduction

The aim proposed in this chapter is to investigate electron transport properties for SiNW having different cross-sections of the wire. We shall focus ourselves in the square and equilateral triangle shape of the wire. In particular quantum wires with equilateral triangle cross-sections have received lots of attention by researchers during the last decade [47–49] because they represent a step toward the employment of non planar structures for the realization of integrated circuits.

The triangular shape of the wire allows strong reduction of the wire dimensions by successive thermal oxidation steps, as confirmed also by numerical simulations [50, 51]. It has been shown that by starting from a trapezoidal section, obtained by silicon anisotropic etching, a lateral oxidation bring to a triangular section which is very suitable for further strong and well controlled reduction of the dimensions by silicon oxidation [51]. Moreover electrical simulation confirmed that the electric field is stronger on the corners of triangular section and that low doped wires can be easily driven in inversion state with an accumulation of carriers at the corners of the section [50].

Figure 5.1 shows a simulation of an oxidation process for a trapezoidal section. The oxide growth proceeds from the top and the sloping sides of the section. If the minor base and the thickness are correctly designed, a triangular silicon cross section is formed after a suitable oxidation time. A gate on top of the wire that wraps the device and a silicon substrate which behaves as a back gate, act on the triangular silicon core.

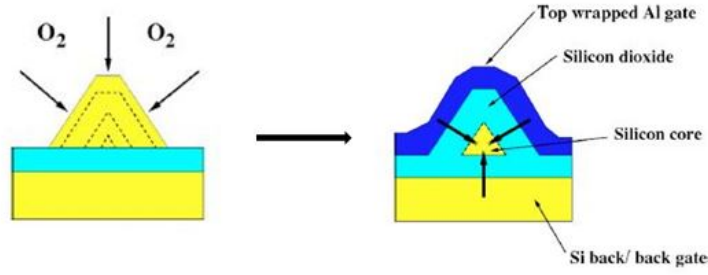


Fig. 5.1 Sketch of the oxidation process. The oxide is slowly removed and the triangular section can be further reduced in a controllable way.

5.2 Simulation results for triangular and square SiNW

In this section simulation results for infinitely deep SiNW with various cross-sections (triangular and rectangular) are presented [53]. These results have been obtained by assuming the six valleys (in the Brillouin zone) as equivalent and a *single valley model* is then employed (with single effective mass $m^* = 0.32 m_e$). Moreover for our applications we shall consider the so called *bulk case*.

We assume that the cross-section A of the wire is surrounded by an oxide which gives rise to an infinitely deep potential barrier,

$$U(y,z) = \begin{cases} 0 & (y,z) \in A \\ \infty & \text{otherwise.} \end{cases} \quad (5.1)$$

In such a case analytical relations for the confinement energies $\varepsilon_{\mu x}$ and envelope functions $\chi_{\mu x}$ can be obtained from eq. (2.4) (with $\varphi = 0$), according to the shape of the cross-section. In particular, in the case of rectangular cross-section they have been found in the section 2.2:

$$\varepsilon_{n_y, n_z} = \frac{\hbar^2 \pi^2}{2m^*} \left(\frac{n_y^2}{L_y^2} + \frac{n_z^2}{L_z^2} \right), \quad (5.2)$$

$$\chi_{n_y, n_z}(y,z) = \sqrt{\frac{2}{L_y}} \sin\left(\frac{n_y \pi}{L_y} y\right) \sqrt{\frac{2}{L_z}} \sin\left(\frac{n_z \pi}{L_z} z\right) \quad n_y, n_z \in \mathbb{N}. \quad (5.3)$$

The overlap factor $G^{vv'}$ is (by eq. (3.11)):

$$G^{vv'} = \frac{1}{L_y L_z} \left[1 + \frac{1 \sin((n_y - n'_y)\pi)}{2(n_y - n'_y)\pi} \right] \left[1 + \frac{1 \sin((n_z - n'_z)\pi)}{2(n_z - n'_z)\pi} \right], \quad (5.4)$$

being L_y, L_z the rectangle dimensions, and $\mathbf{v} = (n_y, n_z), \mathbf{v}' = (n'_y, n'_z)$.

By using group theory arguments [58], in the case of equilateral triangle cross-section, one obtains:

$$\chi_{p,0}(y,z) = \frac{\sqrt{8}}{3^{\frac{3}{4}}L} \left[\sin\left(\frac{4p\pi z}{\sqrt{3}L}\right) - 2 \sin\left(\frac{2p\pi z}{\sqrt{3}L}\right) \cos\left(\frac{2p\pi y}{L}\right) \right], \quad p = 1, 2, 3, \dots \quad (5.5)$$

$$\begin{aligned} \chi_{p,q}(y,z) = \frac{4}{3^{\frac{3}{4}}L} \left\{ \cos\left[\frac{2\pi yq}{L}\right] \sin\left[\frac{2\pi z(2p+q)}{\sqrt{3}L}\right] \right. \\ \left. - \cos\left[\frac{2\pi yp}{L}\right] \sin\left[\frac{2\pi z(2p+q)}{\sqrt{3}L}\right] - \cos\left[\frac{2\pi y(p+q)}{L}\right] \sin\left[\frac{2\pi z(p-q)}{\sqrt{3}L}\right] \right\} \\ q = 1, 2, 3, \dots, \quad p = q+1, q+2, q+3, \dots \quad (5.6) \end{aligned}$$

where L is the length of the triangle side. The above eigenfunctions fulfill the normalization condition, i.e.

$$\iint_T |\chi_{p,q}(y,z)|^2 dy dz = 1, \quad (5.7)$$

where $T = T_1 \cup T_2$ is the triangular domain (see Fig. 5.2):

$$T_1 = \{(y,z) \in \mathbb{R}^2 : 0 \leq y \leq L/2, 0 \leq z \leq \sqrt{3}y\},$$

$$T_2 = \{(y,z) \in \mathbb{R}^2 : L/2 \leq y \leq L, 0 \leq z \leq \sqrt{3}(L-y)\}.$$

The energy eigenvalues related to eqs (5.5) and (5.6) are given by

$$\varepsilon_{p,q} = \frac{8\hbar^2 \pi^2}{3m^* L^2} (p^2 + pq + q^2), \quad q = 0, 1, 2, \dots, \quad p = q+1, q+2, q+3, \dots \quad (5.8)$$

Let us define $\mathbf{v} = (p, q), \mathbf{v}' = (p', q')$; after long but straightforward calculations, one obtains:

- if $p \neq p'$ and $p' \neq 2p$ then $G^{\mathbf{v}\mathbf{v}'} = \frac{4}{3} \frac{\sqrt{3}}{L^2}$;
- if $p = p'$ then $G^{\mathbf{v}\mathbf{v}'} = \frac{10}{3} \frac{\sqrt{3}}{L^2}$;
- if $p' = 2p$ and the $G^{\mathbf{v}\mathbf{v}'} = \frac{16}{9} \frac{\sqrt{3}}{L^2}$.

We shall compare two SiNW having square and equilateral triangle cross-sections, in such a way both have the same area ($A = 100 \text{ nm}^2$) choosing $L_y = L_z = 10 \text{ nm}$ and $L = 20/\sqrt[4]{3} \simeq 15.19 \text{ nm}$.

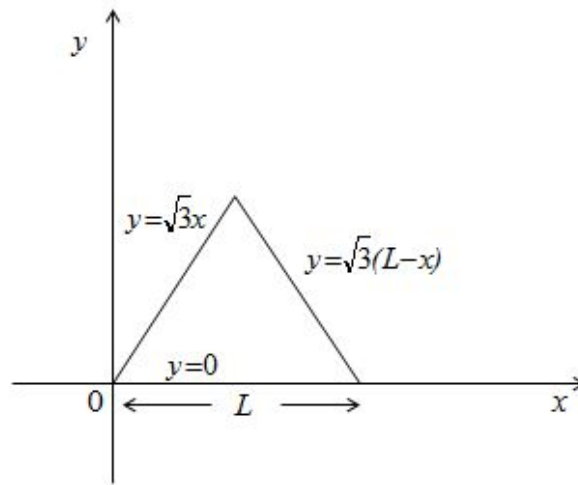


Fig. 5.2

In figure 5.3 we plot the lowest four confinement energies for the square and equilateral triangle cross-sections. We observe that the energy levels are higher in the triangular case [53].

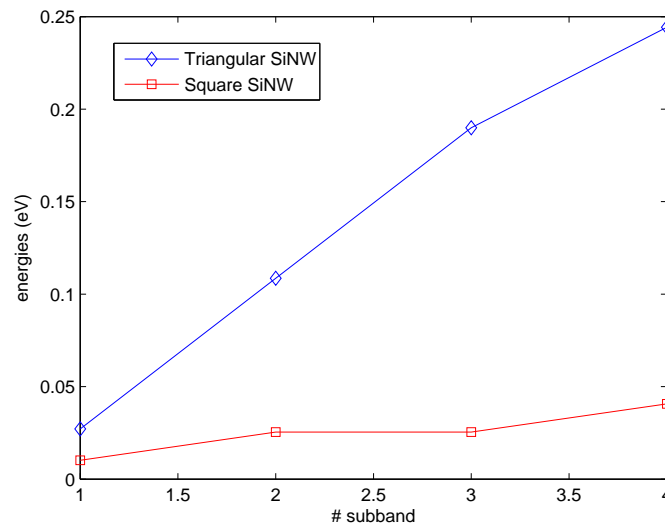


Fig. 5.3 The lowest four confinement energies for the square and equilateral triangle cross-sections.

As concern the description of the transport along the axis of the wire we have constructed an extended hydrodynamic model such as one presented in the previous chapter, including scattering of electrons with acoustic and non-polar optical phonons and by considering, this

time, a non-parabolic approximation for energy band [54]. It is well known that the parabolic band approximation of the conduction band is not fully adequate in order to describe high energy phenomena. A more accurate analytical approximation to the band structure is given by the Kane dispersion relation.

We propose a set of moment equations comprising the balance equations for ρ^v , V^v , W^v , S^v given by eqs. (4.13)-(4.16). By integrating the MBTE with respect to k_x and by choosing $\psi_A = (1, v_x, \mathcal{E}_x, v_x \mathcal{E}_x)$ (4-moments model), with \mathcal{E}_x given by eq. (1.13) and v_x given by eq. (4.4), one obtains the following moment system

$$\frac{\partial \rho^v}{\partial t} + \frac{(\rho^v V^v)}{\partial x} = \rho^v \sum_{v'} C_\rho^{vv'}, \quad (5.9)$$

$$\frac{\partial(\rho^v V^v)}{\partial t} + \frac{\partial(\rho^v U^v)}{\partial x} + \frac{e}{\hbar} \rho^v E_x R^v = \rho^v \sum_{v'} C_V^{vv'}, \quad (5.10)$$

$$\frac{\partial(\rho^v W^v)}{\partial t} + \frac{\partial(\rho^v S^v)}{\partial x} + \rho^v e E_x V^v = \rho^v \sum_{v'} C_W^{vv'}, \quad (5.11)$$

$$\frac{\partial(\rho^v S^v)}{\partial t} + \frac{\partial(\rho^v F^v)}{\partial x} + \frac{e}{\hbar} \rho^v E_x G^v = \rho^v \sum_{v'} C_S^{vv'}, \quad (5.12)$$

The terms U^v , R^v , G^v , F^v are the higher-order fluxes

$$U^v = \frac{2}{(2\pi)} \frac{1}{\rho^v} \int_{\mathbb{R}} f_v(x, k_x, t) v_x^2 dk_x, \quad (5.13)$$

$$R^v = \frac{2}{(2\pi)} \frac{1}{\rho^v} \int_{\mathbb{R}} f_v(x, k_x, t) \frac{\partial v_x}{\partial k_x} dk_x, \quad (5.14)$$

$$G^v = \frac{2}{(2\pi)} \frac{1}{\rho^v} \int_{\mathbb{R}} f_v(x, k_x, t) \frac{\partial(\mathcal{E}_x v_x)}{\partial k_x} dk_x, \quad (5.15)$$

$$F^v = \frac{2}{(2\pi)} \frac{1}{\rho^v} \int_{\mathbb{R}} f_v(x, k_x, t) v_x^2 \mathcal{E}_x dk_x, \quad (5.16)$$

while $C_\rho^{vv'}$, $C_V^{vv'}$, $C_W^{vv'}$, $C_S^{vv'}$ are the moments of the collision term of the MBTE equation.

In order to close the system of PDEs (5.9)-(5.12), we use the distribution function arising from the MEP, as in section 4.3:

$$\hat{f}_v = \exp\left(-\frac{\lambda^v}{k_B} - \lambda_W^v \mathcal{E}_x\right) \{1 - \tau(\hat{\lambda}_V^v v_x + \hat{\lambda}_S^v v_x \mathcal{E}_x)\}, \quad (5.17)$$

where the quantities $(\lambda^v, \lambda_W^v, \hat{\lambda}_V^v, \hat{\lambda}_S^v)$ are known functions of the moments $\{\rho^v, V^v, W^v, S^v\}$:

$$\frac{\lambda^v}{k_B} = -\log\left(\frac{\pi\hbar\rho^v}{\sqrt{2m^*d_0}}\right), \quad W^v = \frac{d_1}{d_0}, \quad (5.18)$$

$$\hat{\lambda}_V^v = \frac{m^*d_0}{2\tau(p_1^2 - p_0p_2)} \left(-p_1S^v + p_2V^v\right), \quad (5.19)$$

$$\hat{\lambda}_S^v = \frac{m^*d_0}{2\tau(p_1^2 - p_0p_2)} \left(-p_1V^v + p_0S^v\right), \quad (5.20)$$

d_n and p_n being

$$d_n = \int_0^{+\infty} \mathcal{E}_x^n \frac{1 + 2\alpha\mathcal{E}_x}{\sqrt{\mathcal{E}_x(1 + \alpha\mathcal{E}_x)}} \exp(-\lambda_W\mathcal{E}_x) d\mathcal{E}_x, \quad (5.21)$$

$$p_n = \int_0^{+\infty} \mathcal{E}_x^n \frac{\sqrt{\mathcal{E}_x(1 + \alpha\mathcal{E}_x)}}{1 + 2\alpha\mathcal{E}_x} \exp(-\lambda_W\mathcal{E}_x) d\mathcal{E}_x. \quad (5.22)$$

For the evaluation of the integrals we have expressed dk_x in terms of \mathcal{E}_x , i.e.

$$dk_x = \frac{\sqrt{2m^*}}{2\hbar} \frac{1 + 2\alpha\mathcal{E}_x}{\sqrt{\mathcal{E}_x(1 + \alpha\mathcal{E}_x)}} d\mathcal{E}_x. \quad (5.23)$$

By using the MEP distribution function (5.17) we evaluate the unknown functions appearing in the balance equations by integration. In this way the higher-order flux terms are determined

$$U^v(W) = \frac{2}{m^*} \frac{p_0}{d_0}, \quad R^v(W) = \frac{\hbar}{m^*} \frac{h_0}{d_0}, \quad F^v(W) = \frac{2}{m^*} \frac{p_1}{d_0}, \quad (5.24)$$

$$G^v(W) = \hbar U^v(W) + N^v(W), \quad N^v(W) = \frac{\hbar}{m^*} \frac{h_1}{d_0} \quad (5.25)$$

where

$$h_n = \int_0^{+\infty} \mathcal{E}_x^n \frac{\exp(-\lambda_W\mathcal{E}_x)}{(1 + 2\alpha\mathcal{E}_x)\sqrt{\mathcal{E}_x(1 + \alpha\mathcal{E}_x)}} d\mathcal{E}_x, \quad (5.26)$$

and also closure relations for the production terms are obtained.

Closures for the productions terms

- Production of electron number

In this case we have:

$$\rho^v C_\rho^{vv'} = \frac{2}{2\pi} \sum_\eta \int_{\mathbb{R}} \mathcal{E}_\eta^{ep} [\hat{f}_v, \hat{f}_{v'}] dk_x = \rho^v C_\rho^{vv'}(op) + \rho^v C_\rho^{vv'}(ac), \quad (5.27)$$

$$\rho^v C_{\rho}^{vv'}(op) = \frac{s_{op} L_x \sqrt{2m^*}}{2\pi\hbar} \left\{ G^{v'v} \frac{\rho^{v'}}{d_0} \left[g_0 I_{\rho}^0(\Delta_{vv'}^+, \lambda_W^{v'}) + (g_0 + 1) I_{\rho}^0(\Delta_{vv'}^-, \lambda_W^{v'}) \right] - G^{vv'} \frac{\rho^v}{d_0} \left[g_0 I_{\rho}^0(-\Delta_{vv'}^-, \lambda_W^v) + (g_0 + 1) I_{\rho}^0(-\Delta_{vv'}^+, \lambda_W^v) \right] \right\}, \quad (5.28)$$

$$\rho^v C_{\rho}^{vv'}(ac) = \frac{s_{ac} L_x \sqrt{2m^*}}{2\pi\hbar} \left\{ G^{v'v} \frac{\rho^{v'}}{d_0} I_{\rho}^0(\Delta_{vv'}, \lambda_W^{v'}) - G^{vv'} \frac{\rho^v}{d_0} I_{\rho}^0(-\Delta_{vv'}, \lambda_W^v) \right\}, \quad (5.29)$$

$$\Delta_{vv'}^{\pm} = \varepsilon_{v'} - \varepsilon_v \pm \hbar\omega_0, \quad \Delta_{vv'} = \varepsilon_{v'} - \varepsilon_v,$$

where

$$I_{\rho}^n(\Delta, \lambda_W) = \int_0^{+\infty} \mathcal{E}_x^n \frac{H(y_1(1 + \alpha y_1))}{\sqrt{\mathcal{E}_x + \Delta}} \frac{1 + 2\alpha(\mathcal{E}_x + \Delta)}{\sqrt{1 + \alpha(\mathcal{E}_x + \Delta)}} \frac{1 + 2\alpha\mathcal{E}_x}{\sqrt{\mathcal{E}_x(1 + \alpha\mathcal{E}_x)}} \exp(-\lambda_W \mathcal{E}_x) d\mathcal{E}_x.$$

with s_{op} and s_{ac} given by eqs. (3.12)₂, (3.18)₂ respectively. $H(x)$ is the Heaviside function and $y_1 = \mathcal{E}_x + \Delta$.

- Production of electron crystal momentum

$$\rho^v C_V^{vv'} = \frac{2}{2\pi} \sum_{\eta} \int_{\mathbb{R}} \mathcal{E}_{\eta} [\hat{f}_v, \hat{f}_{v'}] v_x dk_x = \rho^v C_V^{vv'}(op) + \rho^v C_V^{vv'}(ac), \quad (5.30)$$

$$\rho^v C_V^{vv'}(op) = \frac{\rho^v}{p_1^2 - p_0 p_2} \left(\Omega_1^{vv'} V^v + \Omega_2^{vv'} S^v \right), \quad (5.31)$$

$$\rho^v C_V^{vv'}(ac) = \frac{\rho^v}{p_1^2 - p_0 p_2} \left(\Delta_1^{vv'} V^v + \Delta_2^{vv'} S^v \right). \quad (5.32)$$

Finally (5.30) writes

$$\rho^v C_V^{vv'} = \frac{\rho^v}{p_1^2 - p_0 p_2} \left(\mathcal{A}^{vv'} V^v + \mathcal{B}^{vv'} S^v \right) \quad (5.33)$$

where

$$\mathcal{A}^{vv'} = \Omega_1^{vv'} + \Delta_1^{vv'}, \quad \mathcal{B}^{vv'} = \Omega_2^{vv'} + \Delta_2^{vv'}, \quad (5.34)$$

with

$$\Omega_1^{vv'} = \frac{s_{op} L_x \sqrt{2m^*}}{2\pi\hbar} G^{v'v} \left\{ p_2 \left[g_0 I_V^0(\Delta_{vv'}^-, \lambda_W^v) + (g_0 + 1) I_V^0(\Delta_{vv'}^+, \lambda_W^v) \right] - p_1 \left[g_0 I_V^1(\Delta_{vv'}^-, \lambda_W^v) + (g_0 + 1) I_V^1(\Delta_{vv'}^+, \lambda_W^v) \right] \right\}, \quad (5.35)$$

$$\Omega_2^{vv'} = \frac{s_{op} L_x \sqrt{2m^*}}{2\pi\hbar} G^{vv'} \left\{ -p_1 \left[g_0 I_V^0(\Delta_{vv'}^-, \lambda_W^v) + (g_0 + 1) I_V^0(\Delta_{vv'}^+, \lambda_W^v) \right] \right. \\ \left. + p_0 \left[g_0 I_V^1(\Delta_{vv'}^-, \lambda_W^v) + (g_0 + 1) I_V^1(\Delta_{vv'}^+, \lambda_W^v) \right] \right\}, \quad (5.36)$$

and

$$\Delta_1^{vv'} = \frac{s_{ac} L_x \sqrt{2m^*}}{2\pi\hbar} G^{vv'} \left[p_2 I_V^0(\Delta_{vv'}, \lambda_W^v) - p_1 I_V^1(\Delta_{vv'}, \lambda_W^v) \right], \quad (5.37)$$

$$\Delta_2^{vv'} = \frac{s_{ac} L_x \sqrt{2m^*}}{2\pi\hbar} G^{vv'} \left[-p_1 I_V^0(\Delta_{vv'}, \lambda_W^v) + p_0 I_V^1(\Delta_{vv'}, \lambda_W^v) \right], \quad (5.38)$$

where

$$I_V^n(\Delta, \lambda_W) = \int_0^{+\infty} \mathcal{E}_x^n H(y_0(1 + \alpha y_0)) \frac{1 + 2\alpha y_0}{\sqrt{y_0(1 + \alpha y_0)}} \frac{\sqrt{\mathcal{E}_x(1 + \alpha \mathcal{E}_x)}}{1 + 2\alpha \mathcal{E}_x} \exp(-\lambda_W \mathcal{E}_x) d\mathcal{E}_x, \quad (5.39)$$

$$y_0 = \mathcal{E}_x - \Delta.$$

- Production of electron energy

$$\rho^v C_W^{vv'} = \frac{2}{2\pi} \sum_{\eta} \int_{\mathbb{R}} \mathcal{E}_\eta^{ep} [\hat{f}_v, \hat{f}_{v'}] \mathcal{E}_x dk_x = \rho^v C_W^{vv'}(op) + \rho^v C_W^{vv'}(ac), \quad (5.40)$$

$$\rho^v C_W^{vv'}(op) = \frac{s_{op} L_x \sqrt{2m^*}}{2\pi\hbar} \left\{ G^{v'v} \frac{\rho^{v'}}{d_0} \left[g_0 I_W(\Delta_{vv'}^+, \lambda_W^{v'}) + (g_0 + 1) I_W(\Delta_{vv'}^-, \lambda_W^{v'}) \right] \right. \\ \left. - G^{vv'} \frac{\rho^v}{d_0} \left[g_0 I_\rho^1(-\Delta_{vv'}^-, \lambda_W^v) + (g_0 + 1) I_\rho^1(-\Delta_{vv'}^+, \lambda_W^v) \right] \right\}, \quad (5.41)$$

$$\rho^v C_W^{vv'}(ac) = \frac{s_{ac} L_x \sqrt{2m^*}}{2\pi\hbar} \left\{ G^{v'v} \frac{\rho^{v'}}{d_0} I_W(\Delta_{vv'}, \lambda_W^{v'}) - G^{vv'} \frac{\rho^v}{d_0} I_\rho^1(-\Delta_{vv'}, \lambda_W^v) \right\}. \quad (5.42)$$

where

$$I_W(\Delta, \lambda_W) = \int_0^{+\infty} H(y_1(1 + \alpha y_1)) \sqrt{\mathcal{E}_x + \Delta} \frac{1 + 2\alpha(\mathcal{E}_x + \Delta)}{\sqrt{1 + \alpha(\mathcal{E}_x + \Delta)}} \times \\ \frac{1 + 2\alpha \mathcal{E}_x}{\sqrt{\mathcal{E}_x(1 + \alpha \mathcal{E}_x)}} \exp(-\lambda_W \mathcal{E}_x) d\mathcal{E}_x. \quad (5.43)$$

- Production of electron energy-flux

$$\rho^v C_S^{vv'} = \frac{2}{2\pi} \sum_{\eta} \int_R \mathcal{E}_{\eta}[f_v, f_{v'}] \mathcal{E}_x v_x dk_x = \rho^v C_S^{vv'}(op) + \rho^v C_S^{vv'}(ac). \quad (5.44)$$

The results are similar to the production of crystal momentum (5.30), supposing to add the factor \mathcal{E}_x in the integrand function. Hence

$$\rho^v C_S^{vv'}(op) = \frac{\rho^v}{p_1^2 - p_0 p_2} \left(\Omega_1^{*vv'} V^v + \Omega_2^{*vv'} S^v \right), \quad (5.45)$$

$$\rho^v C_S^{vv'}(ac) = \frac{\rho^v}{p_1^2 - p_0 p_2} \left(\Delta_1^{*vv'} V^v + \Delta_2^{*vv'} S^v \right). \quad (5.46)$$

Finally (5.44) writes

$$\rho^v C_S^{vv'} = \frac{\rho^v}{p_1^2 - p_0 p_2} \left(\mathcal{A}^{*vv'} V^v + \mathcal{B}^{*vv'} S^v \right) \quad (5.47)$$

where

$$\mathcal{A}^{*vv'} = \Omega_1^{*vv'} + \Delta_1^{*vv'}, \quad \mathcal{B}^{*vv'} = \Omega_2^{*vv'} + \Delta_2^{*vv'}. \quad (5.48)$$

with

$$\Omega_1^{*vv'} = \frac{s_{op} L_x \sqrt{2m^*}}{2\pi\hbar} G^{vv'} \left\{ p_2 \left[g_0 I_V^1(\Delta_{vv'}^-, \lambda_W^v) + (g_0 + 1) I_V^1(\Delta_{vv'}^+, \lambda_W^v) \right] - p_1 \left[g_0 I_V^2(\Delta_{vv'}^-, \lambda_W^v) + (g_0 + 1) I_V^2(\Delta_{vv'}^+, \lambda_W^v) \right] \right\}, \quad (5.49)$$

$$\Omega_2^{*vv'} = \frac{s_{op} L_x \sqrt{2m^*}}{2\pi\hbar} G^{vv'} \left\{ -p_1 \left[g_0 I_V^1(\Delta_{vv'}^-, \lambda_W^v) + (g_0 + 1) I_V^1(\Delta_{vv'}^+, \lambda_W^v) \right] + p_0 \left[g_0 I_V^2(\Delta_{vv'}^-, \lambda_W^v) + (g_0 + 1) I_V^2(\Delta_{vv'}^+, \lambda_W^v) \right] \right\}, \quad (5.50)$$

and

$$\Delta_1^{*vv'} = \frac{s_{ac} L_x \sqrt{2m^*}}{2\pi\hbar} G^{vv'} \left[p_2 I_V^1(\Delta_{vv'}, \lambda_W^v) - p_1 I_V^2(\Delta_{vv'}, \lambda_W^v) \right], \quad (5.51)$$

$$\Delta_2^{*vv'} = \frac{s_{ac} L_x \sqrt{2m^*}}{2\pi\hbar} G^{vv'} \left[-p_1 I_V^1(\Delta_{vv'}, \lambda_W^v) + p_0 I_V^2(\Delta_{vv'}, \lambda_W^v) \right]. \quad (5.52)$$

5.2.1 Applications to the case of bulk silicon

The previous results will be now applied to test the model in the case of *bulk silicon*. As known the simulation of the bulk semiconductor constitutes the basic step in the analysis of semiconductors devices.

The physical situation is represented by a SiNW homogeneously doped to $N_D = 10^{18} \text{ cm}^{-3}$ (with $N_A = 0$) and sufficiently long in such a way the neutrality charge condition hold, i.e. $n - N_D + N_A = 0$. Then, by assuming Neumann boundary conditions at the oxide interface, and Dirichlet boundary conditions at the cathode and anode

$$\left. \frac{\partial \varphi}{\partial \mathbf{n}} \right|_{\partial A} = 0, \quad \varphi(0, y, z) = 0, \quad \varphi(L_x, y, z) = eV_b \quad (5.53)$$

where \mathbf{n} is the unit vector normal to ∂A , the Poisson equation (2.7) gives

$$\varphi(x, y, z) = \frac{eV_b}{L_x} x. \quad (5.54)$$

The EMA equation (2.4) with (6.3) and (5.54), gives

$$E_{vx} = \varepsilon_{vx} + \frac{eV_b}{L_x} x + \frac{\hbar^2 k_x^2}{2m^*} + E_c \quad (5.55)$$

where the confinement energies ε_{vx} and the envelope functions χ_{vx} are given by the previous formulas (5.2)-(5.6), and the force acting of the electrons (4.2)₂ reduces to the usual electric field

$$E_x = -\frac{1}{e} \frac{\partial E_{vx}}{\partial x} = -\frac{V_b}{L_x}. \quad (5.56)$$

We have performed a numerical integration of our hydrodynamic model in the stationary homogeneous case with a constant electric field E_x along the x direction. In this case the spatial dependence is dropped and then the unknowns (ρ^v , V^v , W^v , S^v) depend only on the time. Therefore the balance equations reduce to a set of ordinary differential equations.

The initial data are the equilibrium values obtained with a global Maxwellian i.e.

$$f_M^v(k_x) = \exp\left(-\frac{\frac{\hbar^2 k_x^2}{2m^*} + \varepsilon_{vx} + E_c - \mu_E}{k_B T_L}\right) \quad (5.57)$$

where μ_E is the equilibrium chemical potential and T_L the lattice temperature. By inserting the eq. (5.57) into (2.9), (4.14)-(4.16) after simple calculation we get

$$V^v(0) = 0, \quad W^v(0) = \frac{1}{2}k_B T_L, \quad S^v(0) = 0 \quad (5.58)$$

$$\rho^v(0) = AN_D \frac{\exp\left(\frac{-\varepsilon_v}{k_B T_L}\right)}{\sum_v \exp\left(\frac{-\varepsilon_v}{k_B T_L}\right)} \quad (5.59)$$

Let us define the following average quantities:

$$\rho_{tot} = \sum_v \rho^v \quad \text{total linear density,} \quad (5.60)$$

$$V = \frac{\sum_v \rho^v V^v}{\rho_{tot}} \quad \text{mean velocity,} \quad (5.61)$$

$$W = \frac{\sum_v \rho^v W^v}{\rho_{tot}} \quad \text{mean energy,} \quad (5.62)$$

$$S = \frac{\sum_v \rho^v S^v}{\rho_{tot}} \quad \text{mean energy flux.} \quad (5.63)$$

For the our applications we have considered $v = 1, 2, 3, 4$. In fact, the numerical experiments indicate that it is sufficient to take into account only the first four subbands since the other ones are very scarcely populated.

In figure 5.4 we plot the subband linear densities versus the simulation time for the equilateral triangle cross-section of the wire with an electric field of 10 kV/cm. The linear density in the forth subband is about 5% of the total linear density as a confirmation that the inclusion of further subbands has a negligible effects.

In the figures 5.5-5.7 the average values of velocity, energy, energy-flux, as function of simulation time are reported, for some values of the electric field and for a SiNW having a square cross-section. We can observe that the stationary regime is reached in a few picoseconds. Moreover during the transient period the average velocity overshoots its asymptotic value, that is the value attained in the stationary case (this effect is more evident by increasing the strength of the electric field). Similar results have been obtained also in the triangular case.

All constants and parameters which are used in the our simulation are listed in Tab.5.1.

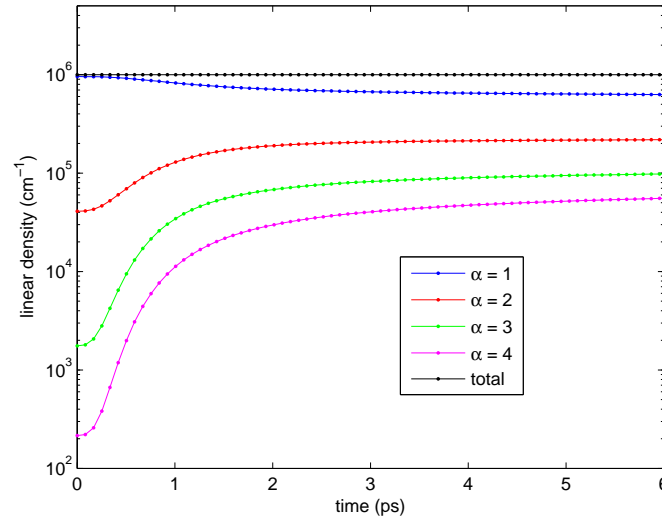


Fig. 5.4 The subband linear densities ρ^V and the total linear density (5.60) versus the simulation time, for an electric field of 10 kV/cm, and equilateral triangle cross-section.

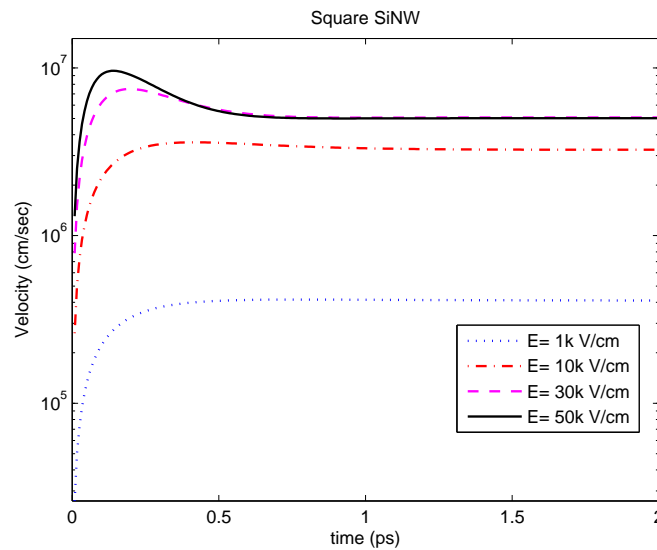


Fig. 5.5 Velocity versus time for some values of the electric field, with $L_x = L_y = 10$ nm.

5.3 Electron mobility

The mobility is one of the most important parameters that determine the performance of a field-effect transistor. In semiconductors, carriers are accelerated by the presence of an electric field and achieve an average velocity determined by the carrier scattering processes. At low electric field, the carrier drift velocity is proportional to the electric field strength, and

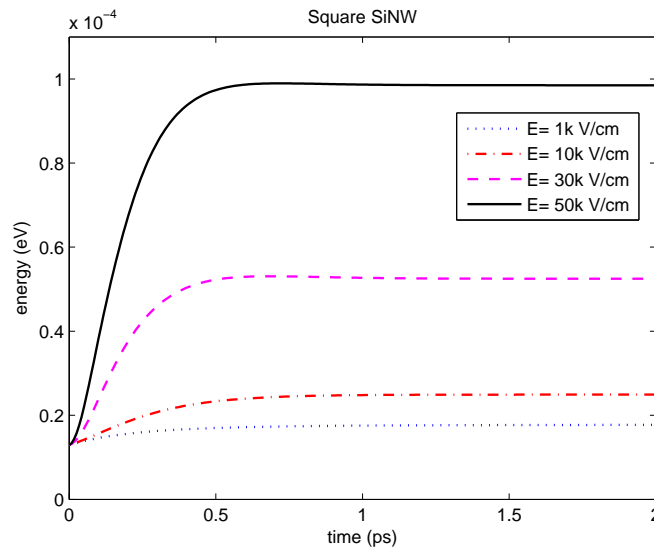


Fig. 5.6 Electron energy versus time for some values of the electric field, with $L_x = L_y = 10$ nm.

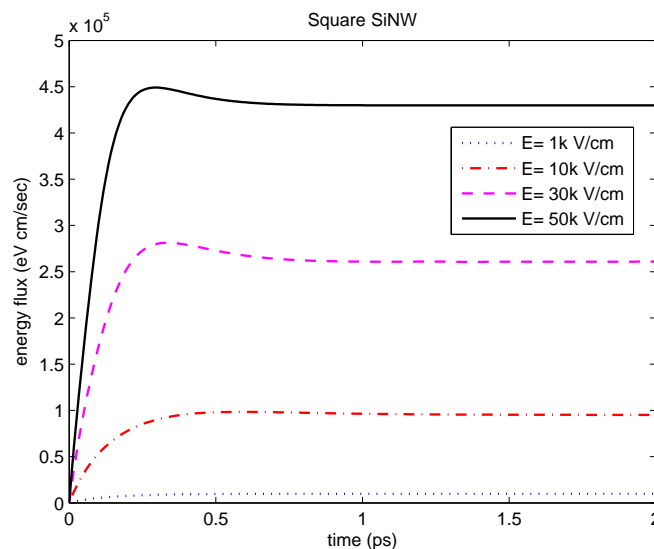


Fig. 5.7 Electron energy-flux versus time for some values of the electric field, with $L_x = L_y = 10$ nm.

the proportionality constant is defined as the mobility. Hence a higher mobility material is likely to have higher frequency response, because carriers take less time to travel through the device. When the fields are sufficiently large, non linearities in the mobility is observed and the velocity approaches a constant value known as the *saturated drift velocity*. In fact, the scattering of the carriers with the lattice, the impurities, and the surface is more active for

Table 5.1 Simulation parameters for single valley model

Quantity	Symbol	Value
non-parabolicity parameter	α	0.5 eV ⁻¹
effective mass	m^*	0.32 m_e
mass density	ρ	2.33 g/cm ³
mean sound velocity	v_s	6.96 10 ⁵ cm/s
lattice temperature	T_L	300 K
acoustic deformation potential	D_1	9 eV
non-polar optical deformation potential	D_0	11.4 10 ⁸ eV/cm
optical phonon energy	$\hbar\omega_0$	63 meV
donor doping	N_D	10 ¹⁸ cm ⁻³

higher fields, and the charges lose the energy gained by the electric field.

In figure 5.8 values for the drift velocity, obtained in the stationary regime, versus the electric field in the square and triangular case are shown. The average drift velocity is defined as

$$\langle V(t) \rangle = \frac{\sum_v \rho^v V^v}{\sum_v \rho^v}, \quad v = 1, \dots, 4. \quad (5.64)$$

As expected, by increasing the electric field, the velocity is no longer to increase in proportion to the electric field. It approaches a constant value of saturated drift velocity. For silicon the saturation velocity is about 10⁷ cm/sec.

We have investigated the *bulk mobility* in the non parabolic band case. It is defined as

$$\mu(E_x) = \frac{\sum_v \rho^v \mu^v}{\sum_v \rho^v}, \quad \mu^v = \frac{V^v(\infty)}{E_x}; \quad (5.65)$$

where μ^v is the subband mobility. In the figures 5.9 and 5.10 we plot the bulk mobility as function of the electric field for the triangular and square cross-sections. In the same figures, we have compared the mobility obtained by means of our hydrodynamic model, with the mobility given by the Caughey-Thomas formula [8]

$$\mu_C = \mu_0 \left[1 + \left(\frac{\mu_0 E_x}{v_s} \right)^2 \right]^{-\frac{1}{2}} \quad (5.66)$$

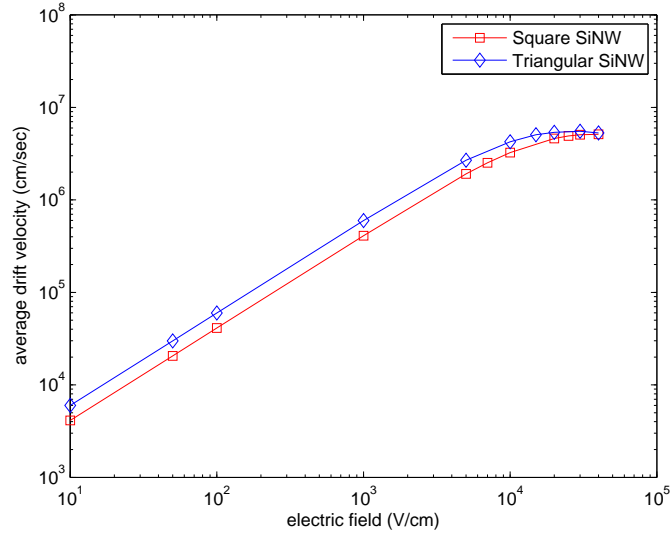


Fig. 5.8 The asymptotic value of the average velocity $\langle V(\infty) \rangle$ (5.64) versus the electric field for the square and the equilateral triangle cross-sections.

where $\mu_0 = \mu(E_x = 10 \text{ V/cm})$ and v_s is the average drift velocity for high fields. From the above figures we notice that, for low fields ($\leq 1000 \text{ V/cm}$), the mobility is constant whereas, for high fields, the mobility decreases because the scattering processes become more active. Similar results have been obtained, in the square case, using the more expensive MC simulations in [24]. We notice also that the value obtained for the low field mobility in the triangular cross-section case ($\mu_0 = 600 \text{ cm}^2 \text{ V/sec}$) is bigger than that obtained in the square case ($\mu_0 = 412 \text{ cm}^2 \text{ V/sec}$).

In order to explain this behaviour, we notice that the confinement factor $G^{vv'}$ is smaller in the triangular case with respect to the square case. Consequently the scattering rates (3.12), (3.18) are reduced and then one has an enhancement of the mobility [53].

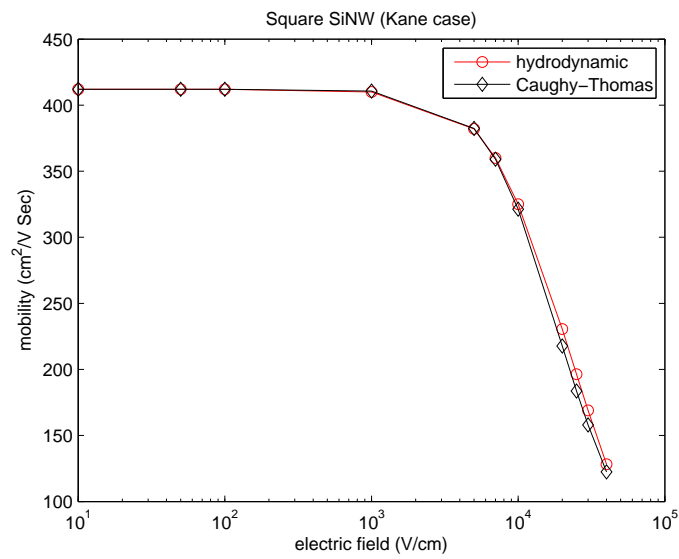


Fig. 5.9 The bulk mobility (5.65) versus the electric field for the square cross-section, and the mobility evaluated using the Caughey-Thomas formula (5.66).

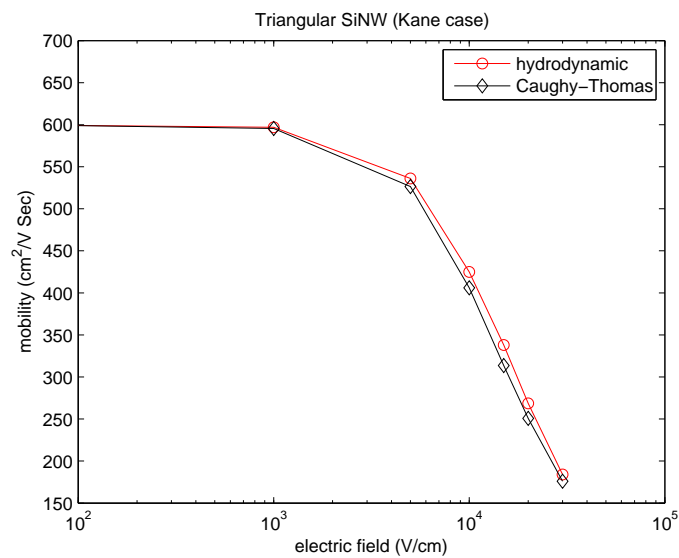


Fig. 5.10 The bulk mobility (5.65) versus the electric field for the equilateral triangle cross-section, and the mobility evaluated using the Caughey-Thomas formula (5.66).

Chapter 6

Self-consistent Schrödinger-Poisson-hydrodynamic solver for SiNW transistors

As already explained, the physical model used for the description of the two dimensional quantum confinement in the cross section of a quantum wire consists of a nonlinear Poisson equation coupled with an eigenvalue problem for Schrödinger's equation. The solution of the Schrödinger equation, in particular, provides subband energies and wave functions which are used to evaluate a three-dimensional charge density. This charge density influences the electric potential obtained as a solution of the Poisson equation, which in turn affects the EMA. Additionally, an appropriate transport model based on a hydrodynamic approach to the solution of semiclassical Boltzmann equation is taking into account.

Contrary to the case treated in the previous chapter, in which an infinite potential outside of the region defining the wire is considered, more realistic nanowire devices would be with a finite height barriers. In this case, analytical solutions of the EMA are not longer found and then a purely numerical approach is required.

Our intention in this chapter is to investigate electron transport phenomena in gated SiNW transistors with a quadratic cross section. For this purpose, a self-consistent solution method for the Schrödinger-Poisson system will be soon presented.

Precisely, in section 6.2 a triple-gate SiNW transistor will be simulated by assuming the charge transport in a ballistic regime [52]. Finally, in section 6.3 simulation results for a Gate-All-Around SiNW transistor are exposed by using an extended hydrodynamic model for the transport along the unbound direction of the wire [68, 70]. The low-field electron mobility, which is a fundamental parameter for engineering applications, will be also evaluated for this kind of device and the surface roughness effects on the mobility will be discussed.

The simulator developed to calculate the low-field mobility has two components: the first is a self-consistent 3D Poisson-2D Schrödinger solver and the second is a 1D hydrodynamic transport model.

6.1 Computational method

First of all, let us summarize the connections among the equations describing the quantum confinement for a nanowire and then we present a specific self-consistent solution algorithm. The spatial confinement for a quantum wire with linear expansion in x -direction is governed by the Schrödinger-Poisson system (SP)

$$\left\{ \begin{array}{l} H[\varphi] \chi_{lx}^{\mu}[\varphi] = \varepsilon_{lx}^{\mu}[\varphi] \chi_{lx}^{\mu}[\varphi] \\ H[\varphi] = -\frac{\hbar^2}{2m_{\mu}^*} \left(\frac{\partial^2}{\partial y^2} + \frac{\partial^2}{\partial z^2} \right) + V_{tot}(x, y, z) \\ \nabla \cdot [\epsilon \nabla \varphi(x, y, z)] = -e(N_D - N_A - n[\varphi]) \\ n[\varphi](x, y, z, t) = \sum_{\mu} \sum_l \rho_l^{\mu}(x, t) |\chi_{lx}^{\mu}[\varphi](y, z, t)|^2 \end{array} \right. \quad (6.1)$$

The eq. (6.1)₁ is the Schrödinger equation in the Effective Mass Approximation (EMA), which it has been proven adequate down to the 3 nm wire width [12]. Eq. (6.1)₃ is the Poisson equation, where ϵ is the permittivity and N_D, N_A are the donor and acceptor density. The electron density $n[\varphi]$ is given by eq. (6.1)₄, where $\rho_l^{\mu}(x, t)$ is the linear density in the μ -valley and l -subband which must be evaluated by the transport model (hydrodynamic/kinetic) in the free movement direction.

Simultaneous solutions of system (6.1) are usually found numerically in an iterative fashion [27, 61–63]. The solution gives the self-consistent electrostatic potential φ , as well as the eigenvalues (or subband energies) ε_{lx}^{μ} and the eigenvectors (or electron envelope wavefunctions) χ_{lx}^{μ} as a function of the unconfined x direction.

Finally, the total electron energy in the μ -valley and l -subband is

$$\left\{ \begin{array}{l} E_l^{\mu} = \varepsilon_{lx}^{\mu} + \mathcal{E}(k_x) + E_c \\ \mathcal{E}(k_x)[1 + \alpha \mathcal{E}(k_x)] = \frac{\hbar^2 k_x^2}{2m_{\mu}^*} \end{array} \right. \quad (6.2)$$

where E_c is the bottom of the conduction band, and α is the non-parabolicity factor (zero in the parabolic case).

For the our applications we shall consider a nanowire which is a silicon parallelepiped with rectangular cross section surrounded by a SiO_2 barrier. In a nanowire we have two contacts: catode and anode. A Silicon Nanowire transistor (SNWT) has a similar structure, but there are three contacts: source, gate, drain. As schematically plotted in Fig. 6.1, the nanowire transistor is a nanowire with an added gate.

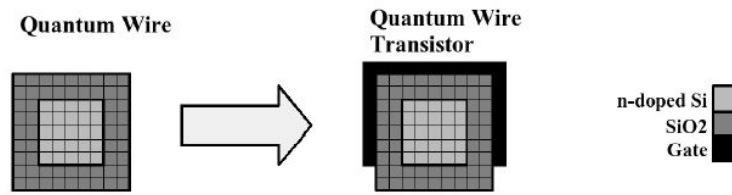


Fig. 6.1 Cross sections of a rectangular nanowire (left) and a rectangular nanowire transistor (right).

The descriptions of the wire and the wire transistor differ only in the boundary conditions of the Poisson equation. The boundary conditions of the wire are Neumann boundary conditions and the boundary conditions of the wire transistor at the gate are Dirichlet boundary conditions.

Let us consider the parallelepiped $\Pi = [a, b] \times [c, d] \times [e, f]$, where x is the free direction of the transport, then

$$L_x = (b - a) \quad , \quad L_y = (d - c) \quad , \quad L_z = (f - e).$$

The internal parallelepiped $\Pi_i = [a, b] \times [c_1, d_1] \times [e_1, f_1] \subset \Pi$ is filled by Si whereas the remaining part $C\Pi = \{\Pi - \Pi_i\}$ is filled by SiO_2 . The confining potential is so defined

$$U(y, z) = \begin{cases} U_0 & \forall (y, z) \in \{[c, d] \times [e, f]\} - \{[c_1, d_1] \times [e_1, f_1]\} \\ 0 & \text{otherwise.} \end{cases} \quad (6.3)$$

In Fig. 6.2 the flowchart of the our implemented algorithm for the solution of Schrödinger-Poisson system is shown. At beginning, we look for the thermal equilibrium solution, which is obtained when no voltage is applied to the contacts and no current flows. With the electron density and the electrostatic potential obtained at equilibrium, we solve the Poisson equation and then the Schrödinger equation with the new potential is solved in each cross section,

providing the subband energy $\varepsilon_{l_x}^\mu$ and the transverse wave function of each subband $\chi_{l_x}^\mu$ which are used to compute the electron density. The entire procedure is iterated until a stopping criterium is fulfilled.

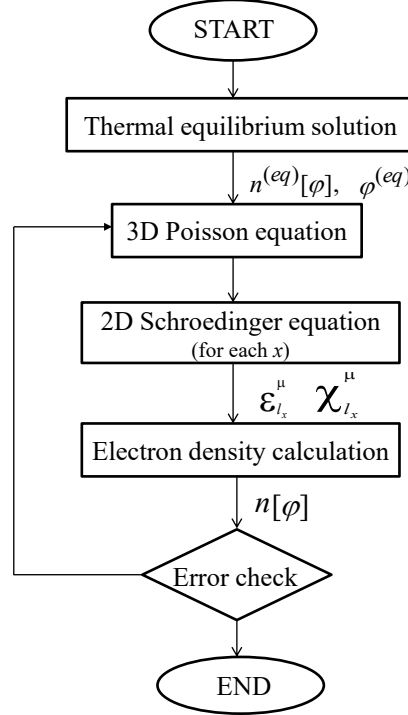


Fig. 6.2 Flowchart of the self-consistent SP solver.

6.1.1 Iteration scheme

The SP system (6.1) forms a coupled nonlinear PDEs, which it is usually solved by an iteration between Poisson and Schrödinger equations. Since in a simple iteration by itself does not converge, it is necessary to introduce an adaptive iteration method [61].

First of all, the parallelepiped $\Pi = [a, b] \times [c, d] \times [e, f]$ is discretized in the usual way, i.e.

$$x_i = a + (i - 1) * dx \quad , \quad i = 1 : N_x \quad , \quad dx = \frac{b - a}{N_x - 1}$$

$$y_j = c + (j - 1) * dy \quad , \quad j = 1 : N_y \quad , \quad dy = \frac{d - c}{N_y - 1}$$

$$z_k = e + (k - 1) * dz \quad , \quad k = 1 : N_z \quad , \quad dz = \frac{f - e}{N_z - 1}$$

The procedure start using the equilibrium solution, i.e

$$n^{(0)} = n^{(eq)} \quad , \quad \varphi^{(0)} = \varphi^{(eq)} .$$

1. **FOR** $m = 0$: **Niter**

solve Poisson equation with a predicted density \tilde{n}

$$\begin{cases} \nabla \cdot [\epsilon \nabla \varphi^{(m+1)}] = -e(N_D - N_A - \tilde{n}[\varphi^{(m+1)}, \varphi^{(m)}]) \\ \tilde{n}[\varphi^{(m+1)}, \varphi^{(m)}] = n^{(m)} \exp \left[\frac{e(\varphi^{(m+1)} - \varphi^{(m)})}{k_B T_L} \right] \end{cases} \quad (6.4)$$

and one obtains $\varphi^{(m+1)}(x, y, z)$.

2. For each x , solve eigenvalue problem for Schrödinger's equation (we omit the μ valley index to simplify the notation).

$$H[\varphi^{(m+1)}] \chi_{lx}^{(m+1)} = \varepsilon_{lx}^{(m+1)} \chi_{lx}^{(m+1)} \quad (6.5)$$

and find $\varepsilon_{lx}^{(m+1)}(y, z)$, $\chi_{lx}^{(m+1)}(y, z)$.

3. Evaluate the exact density

$$n^{(m+1)}(x, y, z) = \frac{N_D L_y L_z}{\mathcal{Z}^{(eq)}} \sum_l \exp \left[-\frac{\varepsilon_{lx}^{(m+1)}}{K_B T_L} \right] |\chi_{lx}^{(m+1)}|^2 \quad (6.6)$$

where

$$\mathcal{Z}^{(eq)} = \sum_l \exp \left[\frac{-\varepsilon_{lx}^{(eq)}}{k_B T_L} \right] \quad (6.7)$$

4. **IF**

$$\frac{\|n^{(l+1)} - n^{(l)}\|_{\infty}}{\|n^{(l+1)}\|_{\infty}} < \text{tol} \quad (6.8)$$

EXIT (end l loop) **ELSE continue**

5.

$$m \rightarrow m + 1 \quad , \quad \mathbf{GOTO} \quad 1$$

We remark that if

$$\left| \frac{e(\varphi^{(m+1)} - \varphi^{(m)})}{k_B T_L} \right| \ll 1$$

we can expand the exp function, and then the eq. (6.4)₂ writes

$$\nabla \cdot [\epsilon \nabla \varphi^{(m+1)}] = -e \left\{ N_D - N_A - n^{(m)} - \frac{e n^{(m)}}{k_B T_L} [\varphi^{(m+1)}, \varphi^{(m)}] \right\} \quad (6.9)$$

The Poisson equation is treated by a central finite difference scheme as well as the effective mass equation. Neumann boundary conditions for the non-contacted parts of the wire and Dirichlet boundary conditions for the source, drain and gate contacts, respectively have been considered. We develop a Poisson solver based on a finite difference scheme in Appendix B. A discretization scheme of the two dimensional EMA equation using central differencing has been already presented in the Chapter 2.

6.2 Ballistic transport

In the simplest case of transport in small structures, one may assume that the particles move through the active region without scattering. This transport is termed *ballistic transport*. If the channel size of the device is far larger than the scattering length, carriers undergo a large number of scattering processes which result in the diffusive carrier motion. If the channel device size is further decreased to less than the scattering length, ballistic carrier motion dominates the transport. The upper limit of the channel size to have a ballistic regime is an open question. Experimental results obtained in deeply scaled silicon MOSFETs [66] have shown that the carrier transport is near ballistic for channel sizes lesser than 50 nm.

For the our study, here we have considered a single valley model and the optimistic case of fully ballistic transport. The electrons are in equilibrium with their injecting reservoir (source or drain) which adsorbs and feed carriers into the channel without reflections. The charges are injected into the channel with unity probability, if their energy in the longitudinal direction is larger than the maximum subband energy ϵ_{vx} . Then the carriers are transferred from the source to the drain without being scattered, and by neglecting tunneling effects. The source to drain current I can be evaluated with use of the method proposed in Landauer's formula [67], which is expressed as a sum of many one-dimensional subband components. Each subband current component flowing in one direction is given by the product of the unit charge, the number of carriers flowing into the subband per unit time, the transmission coefficient of the subband, all integrated over the carrier energy. The number of carriers flowing into the subband is further expressed by the product of the input carrier group velocity, the density of states, and the probability that the state is occupied by the carrier. In the not-degenerate case, the probability of carrier occupancy is given by the Maxwellian

distribution function with the source Fermi level on the source side, and that with the drain Fermi level on the drain side of the subband. Both current directions, the one from the source to the drain and that in the opposite direction, should be considered. Then we have

$$I = e \sum_{\mathbf{v}} \int_0^{+\infty} v_x D(E_{\mathbf{v}}) \{f_{\mathbf{v}}^{(eq)}(E_{\mathbf{v}}, E_{FS}) - f_{\mathbf{v}}^{(eq)}(E_{\mathbf{v}}, E_{FD})\} T(E_{\mathbf{v}}) dE_{\mathbf{v}} \quad (6.10)$$

where $v_x = \hbar k_x / m^*$ is the group velocity, e the electron charge and $D_{\mathbf{v}}(E_{\mathbf{v}})$ is the one-dimensional density of state (1.11) coming out in the first chapter:

$$D(E_{\mathbf{v}}) = \frac{\sqrt{2m^*}}{\hbar\pi} \frac{\delta(E_{\mathbf{v}} - \varepsilon_{\mathbf{v}x})}{\sqrt{E_{\mathbf{v}} - \varepsilon_{\mathbf{v}x}}}. \quad (6.11)$$

$T(E_{\mathbf{v}})$ is the subband transmission coefficient which, in the ballistic transport, implies

$$T(E_{\mathbf{v}}) = \begin{cases} 1 & \text{if } E_{\mathbf{v}} \geq \varepsilon_{\mathbf{v}}^{Max} = \max_x \varepsilon_{\mathbf{v}x} \\ 0 & \text{otherwise} \end{cases} \quad (6.12)$$

In the not-degenerate case the equilibrium distribution function is the Maxwellian, i.e.

$$f_{\mathbf{v}}^{(eq)}(E_{\mathbf{v}}, E_F) \propto \exp\left(-\frac{E_{\mathbf{v}} - E_F}{k_B T_L}\right) \quad (6.13)$$

where E_F is the Fermi energy and T_L the lattice temperature. E_{FS} , E_{FD} are the source and the drain Fermi energies respectively. If V_D and V_S are the applied voltage biases at the drain and source respectively, $V_{DS} = V_D - V_S$ then $E_{FD} = E_{FS} - qV_{DS}$.

The Fermi energy is obtained by imposing charge neutrality along each cross-section of the device, i.e.

$$\int \int n^{(eq)}(x, y, z) dy dz = \int \int (N_D - N_A) dy dz \quad (6.14)$$

and, if we suppose that the doping depends only on the longitudinal dimension x , we obtain

$$E_F(x) = -k_B T_L \log \left\{ \frac{\sqrt{2m^* k_B T_L}}{\pi \hbar [N_D(x) - N_A(x)] L_y L_z} \sum_{\mathbf{v}} \exp\left(-\frac{\varepsilon_{\mathbf{v}x}}{k_B T_L}\right) \right\} \quad (6.15)$$

The equilibrium linear electron density (2.9) is evaluated using eqs. (6.11), (6.13), (6.15)

$$\rho_{\mathbf{v}}^{(eq)}(x) = \int D_{\mathbf{v}}(E_{\mathbf{v}x}) f_{\mathbf{v}}^{(eq)} dE_{\mathbf{v}x} = (N_D - N_A) L_y L_z \frac{\exp\left(-\frac{\varepsilon_{\mathbf{v}x}}{k_B T_L}\right)}{\sum_{\mathbf{v}} \exp\left(-\frac{\varepsilon_{\mathbf{v}x}}{k_B T_L}\right)} \quad (6.16)$$

Then by easy calculations eq. (6.10) reduces to

$$I = \frac{2e}{\hbar\pi} k_B T_L \sum_{\nu} \exp\left(-\frac{\varepsilon_{\nu x}^{Max}}{k_B T_L}\right) \left\{ \exp\left(\frac{E_{FS}}{k_B T_L}\right) - \exp\left(\frac{E_{FD}}{k_B T_L}\right) \right\}. \quad (6.17)$$

6.2.1 Simulation of a triple-gate SiNW transistor

We have considered a SiNW transistor with a parallelepiped shape, having square cross-section with dimension $L_y = L_z = 10$ nm and longitudinal dimension (i.e. the free transport direction) $L_x = 120$ nm. The device consists in an internal parallelepiped filled by Si (having dimension 8×8 nm²) surrounded by SiO₂ of 1 nm thickness, producing the confining potential (2.36). Its structure has three gate electrodes. In fact, in the last decades Multigate nanowires were studied to investigate the impact of increasing the number of gates on the control of the short channel effect which is important in nanoscale devices [71].

The silicon, in the internal parallelepiped, is doped in the n^+ region with $N_D^+ = 10^{18}$ cm⁻³ and in the n region with $N_D = 10^{16}$ cm⁻³, with a regularization at the two junctions given by a hyperbolic tangent profile, i.e.

$$N_D(x) = N_D^+ - \frac{N_D^+ - N_D^-}{2} \left[\tanh\left(\frac{x - x_1}{s}\right) - \tanh\left(\frac{x - x_2}{s}\right) \right] \quad (6.18)$$

where $s = 5$ nm and $x_1 = 10$ nm, $x_2 = 110$ nm. The bottom of the parallelepiped (for $x = 0$) is the source contact, and the top (for $x = 120$ nm) the drain contact. The triple-gate contact surrounds three faces of the parallelepiped with an extension $20 \leq x \leq 100$ nm. The applied biases are $V_S = 0$, $V_D = 0.5$ V and V_G is considered variable.

The simulation procedure here performed is similar than one described in the previous section. It is the following:

- the EMA equation (2.4) is solved with $V_{tot} = U$ in each cross-section ($x = \text{const.}$), obtaining the subband energies $\varepsilon_{\nu z}$ and envelope functions $\chi_{\nu z}$.
- These functions are used to evaluate the charge density (2.8) in equilibrium condition, i.e. with ρ_{ν} given by eq. (6.16).
- The Poisson equation (2.7) is solved leading to a new $V_{tot} = U - eV$.
- If the new V_{tot} does not coincide sufficiently well with the old one, we start a further loop by solving the EMA equation with the new confining potential until the maximum difference between these two quantities is smaller than a predetermined tolerance.

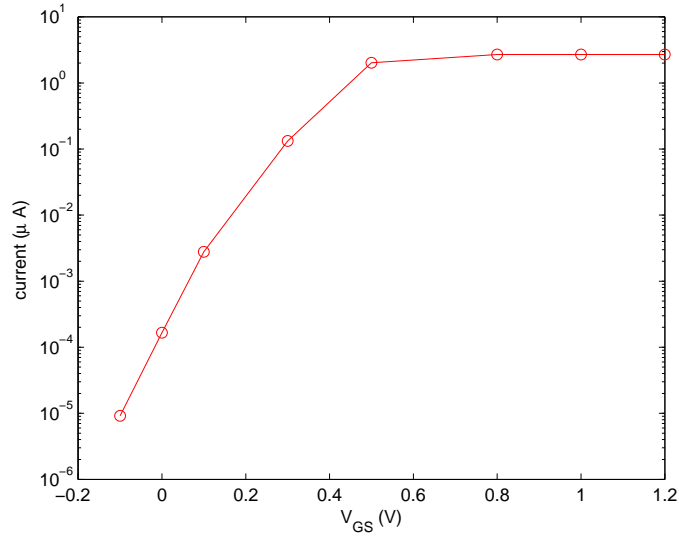


Fig. 6.3 The current (6.17) versus the gate voltage V_{GS}

- For each ν -th subband, we evaluate $\epsilon_V^{Max} = \max_x \epsilon_V$, and finally the current (6.17) is obtained.

The simulation results are shown in figure 6.3. This characteristic curve, obtained in the ballistic approximation, gives us an upper limit to the the performance of this device, and the chosen approximations ensure a very good trade off between accuracy and computational resources required.

6.3 Simulation of a GAA-SiNW Transistor

As integrating smaller sized high performance electronic devices have become a key point over the past decades, innovative transistor designs have emerged. Chip-to-wafer density has to remain high to be competitive so size reduction is still a burning issue and non-planar devices are part of these brand new products. As a consequence, multigate field-effect transistors (FET) have been developed. They are considered an interesting alternative to the conventional planar technology because of their improved gate control. In such new gate architecture, the Gate-All-Around (GAA) SNWT, where the gate encircles the nanowire channel, have recently emerged as a promising device to replace the conventional planar metal oxide semiconductor field effect transistors (MOSFETs) providing better electrostatic control with reduction of short channel effects and a higher current capability [64, 65].

In the model here considered, an appropriate electronic band structure for SiNW obtained by tight-binding simulations, presented in sec. 1.5, has been adopted. As already mentioned, in SiNW the six conduction valleys in the conduction band split up into two groups. The *unprimed* valley Δ_4 , resulting from the four degenerate valleys whose long axis is perpendicular to the x -direction, two *primed* valleys Δ_2, Δ'_2 resulting from the two degenerate valleys whose long axis is parallel to the SiNW. But the two valleys Δ_2, Δ'_2 are symmetric with the same mass (see figure 1.8), and then they can be considered equivalent. Hence, in the following, we shall deal with a two valley model, the valley $A = \Delta_4$ and the valley $B = \Delta_2 = \Delta'_2$. This equivalence in the valleys introduces the following scattering rules, i.e.

$$\text{valley } A \left\{ \begin{array}{l} \text{intravalley, acoustic, elastic } A \leftrightarrow A \\ \text{intravalley, inelastic } A \rightarrow A \quad (f - \text{scattering}, Z_{iv} = 2) \\ \text{intervalley, inelastic } A \rightarrow B \quad (f - \text{scattering}, Z_{iv} = 2) \end{array} \right. \quad (6.19)$$

$$\text{valley } B \left\{ \begin{array}{l} \text{intravalley, acoustic, elastic } B \leftrightarrow B \\ \text{intervalley, inelastic } B \rightarrow A \quad (f - \text{scattering}, Z_{iv} = 2) \\ \text{intravalley, inelastic } B \rightarrow B \quad (g - \text{scattering}, Z_0 = 1) \end{array} \right. \quad (6.20)$$

Scattering with intravalley acoustic and intervalley optical phonons, as well as with surface roughness have been accounted for in our simulations. Let us briefly summarize the scattering rates included in the model, widely discussed in the Chapter 3.

For intravalley elastic scattering (acoustic in the equipartioned case), one obtains:

$$w_{ac}(k_z, \mu, l, k'_z, \mu', l') = s_{ac} G_{ll'}^{\mu\mu'} \delta(E_{l'}^\mu - E_l^\mu), \quad s_{ac} = \frac{2\pi D_{ac}^2 k_B T_L}{\rho \hbar v_s^2 L_x}, \quad \mu = (A, B) \quad (6.21)$$

Supposing the phonons to be in thermal equilibrium, the intervalley scattering rate, writes

$$w_{iv}(k_x, \mu, l, k'_x, \mu', l') = s_{iv} \left[g_{iv} + \frac{1}{2} \mp \frac{1}{2} \right] G_{ll'}^{\mu\mu'} \delta(E_{l'}^{\mu'} - E_l^\mu - \Delta_{\mu\mu'} \mp \hbar \omega_{iv}) \quad (6.22)$$

$$s_{iv} = \frac{\pi D_{iv}^2}{\rho \omega_{iv} L_x} Z_{iv}, \quad \Delta_{\mu\mu'} = \epsilon_\mu^0 - \epsilon_{\mu'}^0, \quad \mu, \mu' = (A, B) \quad (6.23)$$

For intravalley inelastic scattering, the eq. (6.22) is still valid supposing to have $\mu = \mu'$, i.e.

$$w_0(k_x, \mu, l, k'_x, \mu, l') = s_0 \left[g_0 + \frac{1}{2} \mp \frac{1}{2} \right] G_{ll'}^{\mu\mu} \delta(E_{l'}^\mu - E_l^\mu \mp \hbar\omega_0), \quad s_0 = \frac{\pi D_0^2}{\rho \omega_0 L_x} Z_0. \quad (6.24)$$

The SRS is an intraband scattering mechanism and it depends on the electric field normal to the surface. Since the cross section of our wire is a rectangle, we have two contributions, one along to the y -direction and the other along to the z -direction. Hence

$$w_{sr}(k, k') = w_{sr}(k, k', E_y) + w_{sr}(k, k', E_z). \quad (6.25)$$

The SRS rate writes:

$$w_{sr}(k_x, \mu, l, k'_x, \mu, l') = s_{sr} \frac{\lambda_{sr} \Delta_{sr}^2}{(k_x - k'_x)^2 \lambda_{sr}^2 + 2} [\mathcal{F}_{ll'}^{\mu\mu}(E_y)]^2 \delta(E_{l'}^\mu - E_l^\mu), \quad s_{sr} = \frac{4\pi\sqrt{2}e^2}{\hbar L_x} \quad (6.26)$$

The contribution for $w_{sr}(k, k', E_z)$ is similar to eq. (6.26), supposing to change $E_y \rightarrow E_z$. All constants and parameters which are used in the simulation are listed in Tab. 6.2.

As case of study we consider a GAA-SiNW transistor whose structure is schematized in figure 6.4. The gate electrode, which encircle the nanowire channel, is assumed to be metallic, so that there is no potential drop inside the gate, and depletion effects are not considered. The channel of our device is homogeneously doped to $N_D = 3 \cdot 10^{15} \text{ cm}^{-3}$ and it is very long ($L_x = 120 \text{ nm}$) with respect to the transversal dimensions ($L_y = L_z = 10 \text{ nm}$). In such a case the moment system (4.8)-(4.11) reduces to a set of ordinary differential equations with the time as the only independent variable to be coupled to the SP system (6.1).

The wire is surrounded by a silicon oxide layer whose thickness t_{ox} is 1 nm and we assume that this oxide gives rise to a deep potential barrier:

$$U(y, z) = \begin{cases} 0 & \text{if } (y, z) \in \Omega \\ 3.1 \text{ eV} & \text{otherwise.} \end{cases} \quad (6.27)$$

where 3.1 is the height of the energy barrier at the Si-SiO₂ interface.

First of all let us consider the **thermal equilibrium** regime where no voltage is applied to the contacts, i.e. $V_S = V_D = V_G = 0$, and no current flows. In such a case the electron

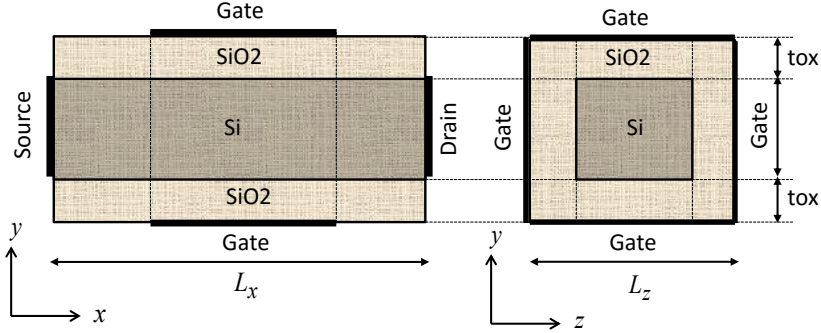


Fig. 6.4 Cross sections of a Gate-All-Around SiNW transistor.

distribution function is the Maxwellian

$$f_l^{\mu(eq)}(k_x) = N_0 \exp\left(-\frac{\hbar^2 k_x^2}{2m_\mu^*} + \varepsilon_l^\mu + \varepsilon_l^0 - \mu_E\right) \quad (6.28)$$

where μ_E is the Fermi level, ε_μ^0 is the valley energy minimum, T the electron temperature which we shall assume to be the same in each subband and equal to the lattice temperature. The condition of zero net current requires that the Fermi level must be constant throughout the sample, and it can be determined by imposing that total electron number equals to the total donor number in the wire. Then the linear electron density at equilibrium writes

$$\rho_l^{\mu(eq)}(x) = \frac{N_D L_y L_z}{Z^{(eq)}} \exp\left[\frac{-\varepsilon_{lx}^{\mu(eq)} - \varepsilon_\mu^0}{k_B T}\right], \quad Z^{(eq)} = \sum_{\mu,l} \sqrt{m_\mu^*} \exp\left[\frac{-\varepsilon_{lx}^{\mu(eq)} - \varepsilon_\mu^0}{k_B T}\right]. \quad (6.29)$$

The simulation procedure involves the following steps:

- SP system (6.1) is solved by using eq. (6.29) with $V_D = V_S = V_G = 0$ and $V_{tot} = U$. A spatial grid of $N_y = N_z = 41$ and $N_x = 11$ points has been adopted.
- Then, the **quasi-equilibrium** regime is considered, where a very small axial electric field frozen along the channel (1000 V/cm) is applied, and we turn on the gate. In such a case the system is still in local thermal equilibrium, the distribution function is the

Maxwellian, but some charge flows in the wire. The linear density writes

$$\rho_l^\mu(x) = \frac{N_D L_y L_z}{Z^{(eq)}} \exp\left[\frac{-\epsilon_{lx}^\mu - \epsilon_\mu^0}{k_B T}\right] \quad (6.30)$$

The iteration scheme described in section 6.1.1 starts using the equilibrium solution, i.e. $\epsilon_{lx}^{\mu(eq)}$, $n^{(eq)}$, $V^{(eq)}$, found in the previous step. The energy subbands ϵ_{lx}^μ in eq. (6.30) are now get by solving self-consistently SP system (6.1) with $V_S = 0.012$ V, $V_D = 0$ V, $V_G = V_g$.

- Repeat iteration until the new electron density does not coincide sufficiently well with the old one (see eq. (6.8)).
- Once the self-consistent global solution is reached, the following profiles from the Poisson-Schrödinger solver are exported into the hydrodynamic model:
 - (a) Potential profile (used in the calculation of SRS);
 - (b) Energies ϵ_{lx}^μ and wave functions χ_l^μ of each subband for both valleys (used in the calculation of all scattering rates);
 - (c) The linear density ρ_l^μ in each valley (used as initial condition for the hydrodynamic system).

Finally, the hydrodynamic ODEs system is solved with the following initial conditions

$$V_l^\mu = 0 \quad , \quad W_l^\mu = \frac{1}{2} k_B T \quad , \quad S_l^\mu = 0.$$

Figure 6.5 shows the distribution of charge density (6.1)₄ and the total potential (2.2) along the cross section at $x = 48$ nm and $z = 0$ nm. A surface inversion layer is formed, similar to a usual MOSFET channel with the electron density peak 1 nm from the oxide interface. The bandbending at the interface forms the quantum well for the electrons.

Figure 6.6 shows the variation of the electron density with increasing gate values V_g . When the gate value increase from 0.02 V to 1 V, a volume inversion layer occurs. For small voltage values carriers are located in the center of the Si body. For higher values of V_g the distance of the electrons from the gated parts of the wire increase and a volume inversion occurs. At high fields from the gate, the SR effects increase whereas the mobility decrease due to the onset of volume inversion.

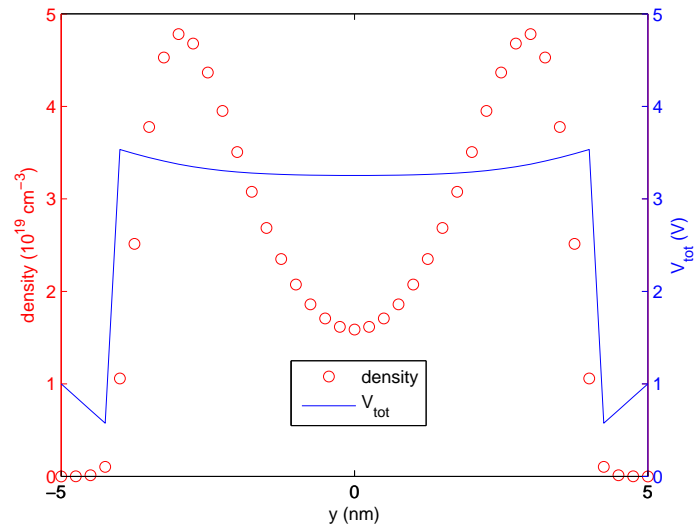


Fig. 6.5 Charge density and total potential along the cross-section at $x = 48$ nm and $z = 0$ nm, under a 1V gate bias.

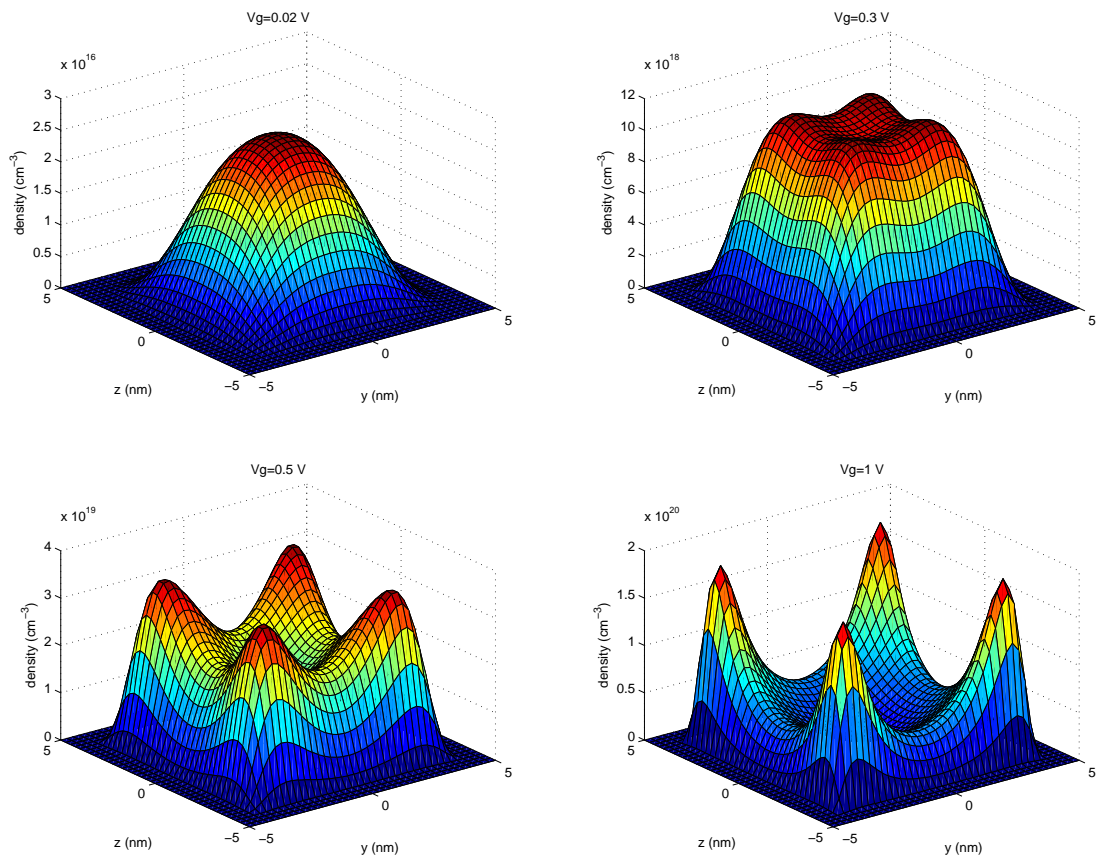


Fig. 6.6 Electron density across the nanowire at $x = 48$ nm. When the gate bias value increase, the onset of volume inversion is evident. The drain-source voltage is fixed at $V_{DS} = 0.012$ V.

In figure 6.7 the total linear density for the A and B valleys (i.e. $\rho^A = \sum_l \rho_l^A$, $\rho^B = \sum_l \rho_l^B$) versus the simulation time is plotted. One can note a depletion of the higher B valley. In fact the electrons change valley according to the intervalley scattering mechanism given by eq. (3.12). The scattering from A to B happens if the electron energy is greater than a certain threshold, whereas the converse is more probable. If we apply a small electric field (1000 V/cm) in the wire, the electrons, at the beginning of the simulation, cannot gain enough energy to jump from A to B , whereas it is more probable that the opposite will happen. As the simulation time increases, the electrons in A gain enough energy (i.e. they have a slightly increase of the mean energy) to activate the jump from A to B and, in the stationary regime, an equilibrium state is reached.

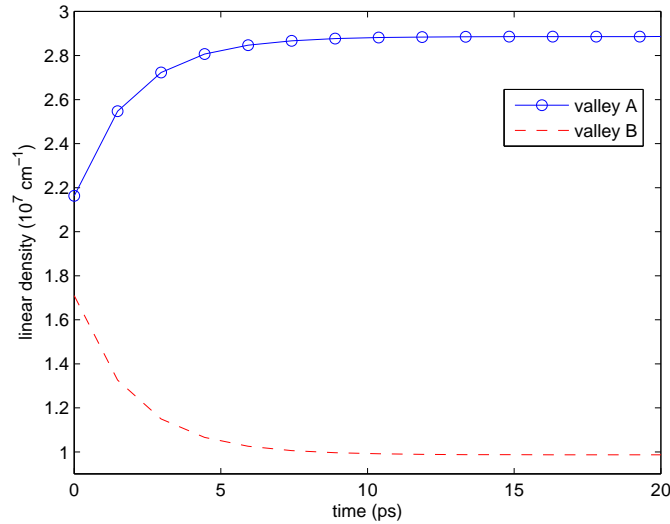


Fig. 6.7 Linear density for the A and B valleys versus the simulation time.

In the figures 6.8-6.9 we show the mean velocity, energy and energy-flux respectively versus the simulation time, obtained with and without SRS mechanism by fixing $V_g = 1$ V. One observes that the stationary regime is reached in a few picoseconds for the velocity and energy-flux, in about ten picoseconds for the energy. The dependence on the SRS mechanism is clearly understood.

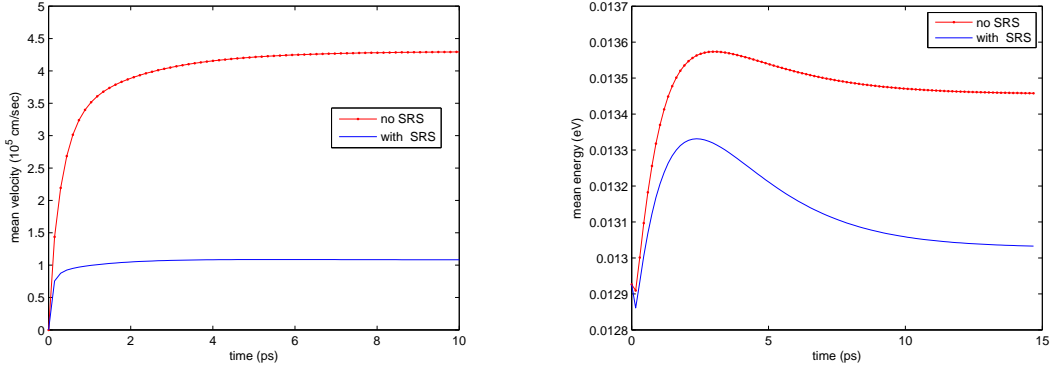


Fig. 6.8 The mean velocity and energy versus the simulation time, obtained with and without SRS mechanism.

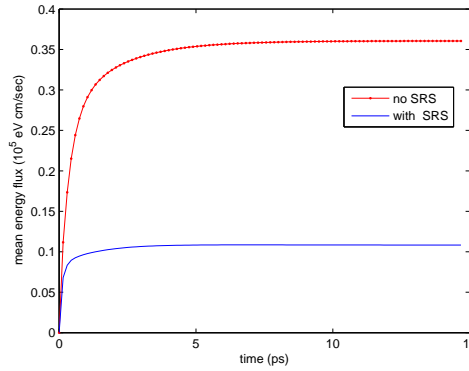


Fig. 6.9 The mean energy flux versus the simulation time, obtained with and without Surface Roughness Scattering mechanism.

6.3.1 Low-field mobility

Finally, we have investigated the low-field mobility which, as measured in long-channel devices at low fields, has a surprisingly strong influence on the performance of short-channel devices [69]. For this reason, it is still used as a figure of merit for benchmarking different technology options and device architectures.

In particular we analyze the effects of phonons and SR scattering on the mobility. After an uniform electric field along the channel of 1 kV/cm is fixed, we compute the mobility as ratio between the average electron velocity, evaluated in the stationary regime, and the driving field, i.e.

$$\mu_{low} = \frac{\mu^A \rho^A + \mu^B \rho^B}{\rho^A + \rho^B} \quad , \quad \mu^A = \frac{\sum_l V_l^A}{E_x} \quad , \quad \mu^B = \frac{\sum_l V_l^B}{E_x} \quad (6.31)$$

where μ^A, μ^B are the mobilities in the respective valleys.

The average electron velocity has been obtained with the following steps: a) we fix V_g and solve the Schrödinger-Poisson system (6.1); b) once this solution has been obtained, the energies ε_i^μ and wave functions χ_i^μ for each subband are exported into the hydrodynamic model, and the linear density ρ_i^μ is used as initial condition; c) the hydrodynamic model 4.8-4.11 is solved and, in the stationary regime, the average velocity has been calculated.

In table 6.1 results for the A and B valley mobility, obtained with and without the SRS mechanism, are presented. The difference between these values proves that the SRS is a key mechanism in the SiNW device performance. In the above table we can notice that mobility in the A -valley is bigger with respect to that obtained in the B -valley.

Table 6.1 low-field mobility (in $\text{cm}^2 / \text{V s}$)

	μ^A	μ^B	μ_{low}
no SRS	556	62	430
with SRS	131	42	108

Since the mobility depends (inversely) on the effective mass, the valley splitting reduces the mobility along the axis of the wire (in the B -valley where the effective mass is 0.94), but quantum confinement increases mobility in the transverse direction (in the A -valley where the effective mass is 0.27).

In figure 6.10 we show the low-field mobility as function of the gate voltage V_g , obtained by including/excluding the SRS mechanism.

As one can note, the inclusion of SR scattering has a strong effect on the mobility. For high gate values, the mobility is strongly reduced than the mobility evaluated taking into account only phonons (acoustic and non-polar) scattering. In fact, surface roughness scattering is the most important cause of mobility degradation in conventional MOSFETs at high transverse fields.

These results are in agreement with those obtained using the more expensive Monte Carlo methods or deterministic schemes for solving the transport part [24–28].

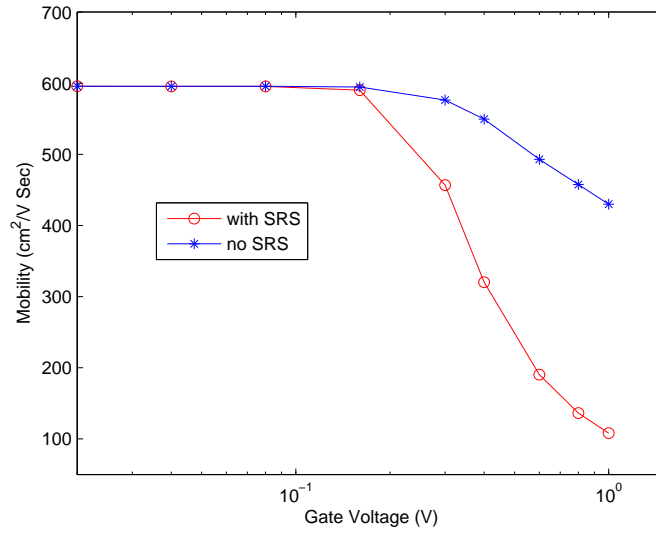


Fig. 6.10 Low-field mobility versus gate voltage, obtained with/without Surface Roughness Scattering mechanism.

Table 6.2 Simulation parameters for two valley model

Quantity	Symbol	Value
effective mass $A = \Delta_4$ valley [11]	m_A^*	$0.27 m_e$
effective mass $B = \Delta_2$ valley [11]	m_B^*	$0.94 m_e$
average sound speed	v_s	$9 \cdot 10^5$ cm/sec
acoustic-phonon deformation potential	D_{ac}	9 eV
intravalley deformation potential g-scat [27]	D_0	$1.1 \cdot 10^9$ eV/cm
intravalley phonon energy [27]	$\hbar\omega_0$	63.3 meV
number equivalent valleys [27]	Z_0	1
intervalley deformation potential f-scat [27]	D_{iv}	$2 \cdot 10^8$ eV/cm
intervalley phonon energy [27]	$\hbar\omega_{iv}$	47.48 meV
number equivalent valleys [27]	Z_{iv}	2
A valley energy minimum [11]	ϵ_A^0	0
B valley energy minimum [11]	ϵ_B^0	117 meV
rms height [27]	Δ_{sr}	0.3 nm
correlation length [27]	λ_{sr}	1.5 nm

Chapter 7

Conclusions

The main goal of this dissertation involves the study of electron transport phenomena in silicon quantum wires by using a hydrodynamic approach to describe the transport along the free motion direction of the wire, coupled with the Schrödinger-Poisson system, governing the spatial confinement. In this hydrodynamic model, macroscopic balance equations are obtained as moment equations of the BTE for electrons in semiconductors. The constitutive relations needed to have a closed system of balance laws are deduced by resorting to MEP. In this method the distribution function used to close the system is assumed to be that which maximizes the entropy under the constraints of the given set of moments. By using the maximum entropy distribution one obtains explicit constitutive relations for the higher-order fluxes and the production terms with the advantage that all transport coefficients are completely determined without any fitting procedure.

In our research activity, we were interested in employing in the model the exact nanowire band structure, which is altered from that of bulk silicon due to the Brillouin zone folding, and in including into the transport model the main scattering mechanisms in SiNWs, such as scattering with intravalley acoustic and intervalley optical phonons and with surface roughness.

The first stage of the work focused on simulations of infinitely deep SiNWs having different cross sections, in the case of bulk silicon and by assuming a non-parabolic approximation for the conduction band. In particular, the results for the electron mobility are in agreement with MC simulation ones.

The second part of the work was devoted to simulate gated SiNW transistors by using a coupled Poisson-Schrödinger-hydrodynamic solver. For this purpose an adaptive iterative method which self-consistently solves the coupled system of Schrödinger and Poisson equations has been developed, by choosing as numerical solution approach a finite difference scheme.

By means of this self-consistent simulator, important transport properties, such as the low-field mobility, have been investigated and effects of SRS on the mobility have been discussed. The obtained results are in good agreement with the other numerical simulations known in literature.

In conclusion, this extended hydrodynamic model is a promising tool for modeling transport phenomena in SiNWs.

Appendix A

Evaluation of the transition rate

We want to evaluate the transition rate (3.6) according to the Fermi's golden rule. If we substitute eqs. (3.5), (3.1) into (3.2) we obtain

$$\begin{aligned}
 \langle \psi' | H_p | \psi \rangle &= \sum_{\mathbf{q}} \int (\chi_{l'}^{\mu})^* \chi_l^{\mu} e^{i(k_x - k'_x \pm q_x)x} \frac{K_q}{L_x} e^{\pm i(q_y y + q_z z)} \sqrt{\frac{\hbar}{2\rho V_c \omega_{\mathbf{q}}}} \left[g(\mathbf{q}) + \frac{1}{2} \mp \frac{1}{2} \right] dx = \\
 \sum_{\mathbf{q}} \int (\chi_{l'}^{\mu})^*(y, z) \chi_l^{\mu}(y, z) e^{\pm i(q_y y + q_z z)} dy dz \int e^{i(k_x - k'_x \pm q_x)x} \frac{K_q}{L_x} \sqrt{\frac{\hbar}{2\rho V_c \omega_{\mathbf{q}}}} \left[g(\mathbf{q}) + \frac{1}{2} \mp \frac{1}{2} \right] dx = \\
 \sum_{q_y, q_z} \int (\chi_{l'}^{\mu})^*(y, z) \chi_l^{\mu}(y, z) e^{\pm i(q_y y + q_z z)} dy dz \sum_{q_x} K_q \sqrt{\frac{\hbar}{2\rho V_c \omega_{\mathbf{q}}}} \left[g(\mathbf{q}) + \frac{1}{2} \mp \frac{1}{2} \right] \frac{1}{L_x} \int e^{i(k_x - k'_x \pm q_x)x} dx.
 \end{aligned} \tag{A.1}$$

The last integral can be solved easily. Since we are considering a long device in the x -direction $L_x \gg L_y, L_z$, then we can perform the limit

$$\lim_{L_x \rightarrow +\infty} \frac{1}{L_x} \int_{-L_x/2}^{L_x/2} e^{ix(k_x - k'_x \pm q_x)} dx = \lim_{L_x \rightarrow +\infty} \frac{\sin \left[\frac{L_x}{2} (k_x - k'_x \pm q_x) \right]}{\frac{L_x}{2} (k_x - k'_x \pm q_x)} = 0 \tag{A.2}$$

and in order the matrix element to be non-vanishing, the exponential argument must be zero, i.e.

$$\frac{1}{L_x} \int_{-L_x/2}^{L_x/2} e^{ix(k_x - k'_x \pm q_x)} dx = \delta_{k'_x \mp k_x, q_x} \tag{A.3}$$

where the previous symbol is the Kronecker delta. Then eq. (A.1) becomes

$$\langle \psi' | H_p | \psi \rangle = \sum_{q_x q_y q_z} \delta_{k'_x \mp k_x, q_x} G_{ll'}^{\mu\mu'\pm}(q_y, q_z) K_q \sqrt{\frac{\hbar}{2\rho V_c \omega_q}} \left[g(q) + \frac{1}{2} \mp \frac{1}{2} \right], \quad (\text{A.4})$$

$$G_{ll'}^{\mu\mu'\pm}(q_y, q_z) = \int (\chi_{l'}^\mu)^*(y, z) \chi_l^\mu(y, z) e^{\pm i(q_y y + q_z z)} dy dz \quad (\text{A.5})$$

where $G_{ll'}^{\mu\mu'\pm}(q_y, q_z) \in \mathbb{C}$ is called *form factor*. Now, we convert the summation into integrals [3]

$$\sum_{q_x} \rightarrow \frac{L_x}{2\pi} \int dq_x$$

$$\begin{aligned} \langle \psi' | H_p | \psi \rangle &= \frac{L_x L_y L_z}{8\pi^3} \int \delta_{k_x \pm q_x, k'_x} G(q_y, q_z) K_q \sqrt{\frac{\hbar}{2\rho V_c \omega_q}} \left[g(q) + \frac{1}{2} \mp \frac{1}{2} \right] dq = \\ & \frac{L_x L_y L_z}{8\pi^3} \int \delta_{k_x \pm q_x, k'_x} G(q_y, q_z) \alpha(q) dq, \quad \alpha(q) = K_q \sqrt{\frac{\hbar}{2\rho V_c \omega_q}} \left[g(q) + \frac{1}{2} \mp \frac{1}{2} \right] \end{aligned}$$

Since $|z|^2 = z^* z, \forall z \in \mathbb{C}$ one has

$$\begin{aligned} |\langle \psi' | H_p | \psi \rangle|^2 &= \left(\frac{L_x L_y L_z}{8\pi^3} \right)^2 \left\{ \int \delta_{k_x \pm q_x, k'_x} G^*(q_y, q_z) \alpha(q) dq \right\} \left\{ \int \delta_{k_x \pm p_x, k'_x} G(p_y, p_z) \alpha(p) dp \right\} = \\ & \left(\frac{L_x L_y L_z}{8\pi^3} \right)^2 \int G^*(q_y, q_z) G(p_y, p_z) \delta_{k_x \pm q_x, k'_x} \delta_{k_x \pm p_x, k'_x} \alpha(q) \alpha(p) dq dp \end{aligned} \quad (\text{A.6})$$

Let us perform the integration over p_x firstly, i.e.

$$\begin{aligned} |\langle \psi' | H_p | \psi \rangle|^2 &= \left(\frac{L_x L_y L_z}{8\pi^3} \right)^2 \int G^*(q_y, q_z) G(p_y, p_z) \delta_{k_x \pm q_x, k'_x} \alpha(q) dq dp_y dp_z \int \delta_{k_x \pm p_x, k'_x} \alpha(p) dp_x = \\ & \left(\frac{L_x L_y L_z}{8\pi^3} \right)^2 \int G^*(q_y, q_z) G(p_y, p_z) \delta_{k_x \pm q_x, k'_x} \alpha(q) dq dp_y dp_z \alpha(p_y, p_z, \pm(k'_x - k_x)) \end{aligned} \quad (\text{A.7})$$

and we suppose [3]

$$G(p_y, p_z) \alpha(p_y, p_z, \pm(k'_x - k_x)) = G(q_y, q_z) \alpha(q_y, q_z, \pm(k'_x - k_x)) \delta(q_z - p_z) \delta(q_x - p_x). \quad (\text{A.8})$$

Eq. (A.7) becomes

$$\begin{aligned}
|\langle \psi' | H_p | \psi \rangle|^2 &= \left(\frac{L_x L_y L_z}{8\pi^3} \right)^2 \times \\
&\int G^*(q_y, q_z) G(q_y, q_z) \delta_{k_x \pm q_x, k'_x} \alpha(q_y, q_z, \pm(k'_x - k_x)) \alpha(\mathbf{q}) \delta(q_z - p_z) \delta(q_z - p_z) dq dp_y dp_z = \\
&\left(\frac{L_x L_y L_z}{8\pi^3} \right)^2 \int G^*(q_y, q_z) G(q_y, q_z) \delta_{k_x \pm q_x, k'_x} \alpha(q_y, q_z, \pm(k'_x - k_x)) \alpha(\mathbf{q}) dq \quad (A.9)
\end{aligned}$$

If we perform an integration over k'_x we get

$$\begin{aligned}
\int |\langle \psi' | H_p | \psi \rangle|^2 dk'_x &= \left(\frac{L_x L_y L_z}{8\pi^3} \right)^2 \int G^*(q_y, q_z) G(q_y, q_z) \alpha(q_y, q_z, q_x) \alpha(\mathbf{q}) dq = \\
&\left(\frac{L_x L_y L_z}{8\pi^3} \right)^2 \int G^*(q_y, q_z) G(q_y, q_z) \alpha^2(\mathbf{q}) dq \quad (A.10)
\end{aligned}$$

and this is the wanted result.

In following we shall use the accepted result in the literature [5], i.e.

$$w(\mathbf{k}, \mathbf{k}') = \frac{2\pi}{\hbar} \sum_{\mathbf{q}} |G_{ll'}^{\mu\mu' \pm}(q_y, q_z)|^2 \frac{\hbar K_q^2}{2\rho V_c \omega_{\mathbf{q}}} \left[g(\mathbf{q}) + \frac{1}{2} \mp \frac{1}{2} \right] \delta_{k'_x \mp k_x, q_x} \delta(E(\psi') - E(\psi) \mp \hbar \omega_{\mathbf{q}}) \quad (A.11)$$

Appendix B

3D Poisson Solver

The equation for the potential $\varphi^{(l+1)}$, in non-dimensional form, is the following:

$$\nabla \cdot \left(\varepsilon_r(x, y, z) \nabla \varphi^{(l+1)} \right) = \beta \left\{ n^{(l)}(x, y, z) \left[\varphi^{(l+1)} - \varphi^{(l)} \right] - N_D(x, y, z) \right\}$$

The potential is assigned on the gate, on the bottom and top surfaces (Dirichlet condition), while on the rest of the boundary we assume that the derivative of $\varphi^{(l+1)}$ along the normal direction of the boundary is zero (Neumann condition). Therefore, the problem for the potential $\varphi^{(l+1)}$ can be written as:

$$-\nabla \cdot \left(\varepsilon_r(x, y, z) \nabla \varphi^{(l+1)} \right) + \lambda \varphi^{(l+1)} = f \quad \text{in } \Omega \quad (\text{B.1})$$

$$\varphi^{(l+1)} = \varphi \quad \text{on } \Gamma_{\text{bottom}} \cup \Gamma_{\text{top}} \cup \Gamma_{\text{gate}} \quad (\text{B.2})$$

$$\frac{\partial \varphi^{(l+1)}}{\partial n} = 0 \quad \text{on } \partial\Omega - (\Gamma_{\text{bottom}} \cup \Gamma_{\text{top}} \cup \Gamma_{\text{gate}}), \quad (\text{B.3})$$

where $\lambda = -\beta n^{(l)}(x, y, z)$, $f = \beta \left\{ n^{(l)}(x, y, z) \varphi^{(l)} + N_D(x, y, z) \right\}$, $\Omega = [a, b] \times [c, d] \times [e, f]$, $\Gamma_{\text{bottom}} = [a, b] \times [c, d] \times \{e\}$, $\Gamma_{\text{top}} = [a, b] \times [c, d] \times \{f\}$, $\Gamma_{\text{gate}} = \{(x, y, z) \in \partial\Omega : z_1 \leq z \leq z_2\}$.

The domain Ω is split into two subdomains Ω_i and Ω_e such that

$$\Omega_i = \{(x, y, z) \in \Omega : x^* \leq x \leq x^{**}, y^* \leq y \leq y^{**}\}$$

(where $a < x^* < x^{**} < b$, $c < y^* < y^{**} < d$) and $\Omega_e = \Omega - \Omega_i$. The coefficient function $\varepsilon_r(x, y, z)$ is discontinuous across $\Gamma = \partial\Omega_i - \partial\Omega$ and therefore the standard central finite-difference method (that is second order accurate on regions with smooth solutions) cannot be used to discretize Eq. (B.1) close to the interface $\partial\Omega_i$, since there is a jump in the derivative

of $\varphi^{(l+1)}$ across the interface that would degrade the order of accuracy. In order to employ a finite-difference method that maintains the second order of accuracy, a proper interface condition must be considered:

$$\lim_{\Omega_i \ni (x,y,z) \rightarrow (\bar{x}, \bar{y}, \bar{z})} \left(\varepsilon_r \frac{\partial \varphi^{(l+1)}}{\partial n} \right) = \lim_{\Omega_e \ni (x,y,z) \rightarrow (\bar{x}, \bar{y}, \bar{z})} \left(\varepsilon_r \frac{\partial \varphi^{(l+1)}}{\partial n} \right), \quad (\text{B.4})$$

where $(\bar{x}, \bar{y}, \bar{z}) \in \Gamma$ and n is the normal direction to Γ .

Finite-Difference discretization of the potential equation

The domain Ω is discretized by a uniform Cartesian grid:

$$(x_i, y_j, z_k), \quad i = 0, \dots, n, \quad j = 0, \dots, m, \quad k = 0, \dots, p, \quad (\text{B.5})$$

where $x_i = a + i\Delta x$, $y_j = c + j\Delta y$ and $z_k = e + k\Delta z$, with $\Delta x = (b - a)/n$, $\Delta y = (d - c)/m$ and $\Delta z = (f - e)/p$. The Cartesian grid is chosen in such a way that $x^* = x_{i^*}$, $x^{**} = x_{i^{**}}$, $y^* = y_{j^*}$, $y^{**} = y_{j^{**}}$ for some integers $2 \leq i^* < i^{**} \leq n - 2$, $2 \leq j^* < j^{**} \leq m - 2$.

The unknown function $\varphi^{(l+1)}$ is therefore represented by a grid function defined over the cartesian grid (B.5), namely by a vector $\vec{v} \in \mathbb{R}^{(n+1)(m+1)(p+1)}$. The approximation of $\varphi^{(l+1)}(x_i, y_j, z_k)$ is represented by the s -th component of the vector \vec{v} , with $s = 1 + i + (n + 1)j + (n + 1)(m + 1)k$. We observe that the relation $s = 1 + i + (n + 1)j + (n + 1)(m + 1)k$ represents a one-to-one map between the grid and the set of the first $(n + 1)(m + 1)(p + 1)$ integers, i.e.:

$$\begin{aligned} \mathcal{M}: \{0, \dots, n\} \times \{0, \dots, m\} \times \{0, \dots, p\} &\longrightarrow \{1, \dots, (n + 1)(m + 1)(p + 1)\}, \\ \text{where } \mathcal{M}(i, j, k) &= 1 + i + (n + 1)j + (n + 1)(m + 1)k. \end{aligned} \quad (\text{B.6})$$

In the following, we can use the notation v_{ijk} to refer to the vector component v_s , with $s = \mathcal{M}(i, j, k)$.

The vector \vec{v} is found by solving a $(n + 1)(m + 1)(p + 1) \times (n + 1)(m + 1)(p + 1)$ linear system obtained as follows. Let s be a generic integer such that $1 \leq s \leq (n + 1)(m + 1)(p + 1)$ and let (x_i, y_j, z_k) be the grid point corresponding to $\mathcal{M}^{-1}(s)$. If $(x_i, y_j, z_k) \in \Gamma_{\text{bottom}} \cup \Gamma_{\text{top}} \cup \Gamma_{\text{gate}}$ the s -th equation of the linear system is obtained from the Dirichlet boundary condition B.2:

$$v_{ijk} = \varphi(x_i, y_j, z_k).$$

If $(x_i, y_j, z_k) \in \partial\Omega - (\Gamma_{\text{bottom}} \cup \Gamma_{\text{top}} \cup \Gamma_{\text{gate}})$ the s -th equation of the linear system is obtained by discretizing the Neumann boundary condition (B.3) on (x_i, y_j, z_k) with second order accuracy as follows (assume that $i = 0$, since the other cases are treated similarly):

$$\frac{3v_{0jk} - 4v_{1jk} + v_{2jk}}{2\Delta x} = 0$$

$$\iff 3v_{0jk} - 4v_{1jk} + v_{2jk} = 0.$$

If $(x_i, y_j, z_k) \in \Gamma$ the s -th equation of the linear system is obtained by discretizing the interface condition (B.4) on (x_i, y_j, z_k) with second order accuracy as follows (assume that $i = i^*$, since the other cases are treated similarly):

$$\frac{3v_{i^*,j,k} - 4v_{i^*+1,j,k} + v_{i^*+2,j,k}}{2\Delta x} - \frac{-3v_{i^*,j,k} + 4v_{i^*-1,j,k} - v_{i^*-2,j,k}}{2\Delta x} = 0.$$

$$\iff 6v_{i^*,j,k} - 4v_{i^*+1,j,k} + v_{i^*+2,j,k} - 4v_{i^*-1,j,k} + v_{i^*-2,j,k} = 0.$$

For all the other grid points, namely (x_i, y_j, z_k) internal to Ω_i or Ω_e , the s -th equation of the linear system is obtained by discretizing (B.1) on (x_i, y_j, z_k) with central second order accuracy as follows:

$$\left(2\varepsilon_{i,j,k} \left(\frac{1}{\Delta x^2} + \frac{1}{\Delta y^2} + \frac{1}{\Delta z^2} \right) + \lambda_{ijk} \right) v_{i,j,k}$$

$$- \frac{\varepsilon_{i-1/2,j,k}}{\Delta x^2} v_{i-1,j,k} - \frac{\varepsilon_{i+1/2,j,k}}{\Delta x^2} v_{i+1,j,k} - \frac{\varepsilon_{i,j-1/2,k}}{\Delta y^2} v_{i,j-1,k} - \frac{\varepsilon_{i,j+1/2,k}}{\Delta y^2} v_{i,j+1,k}$$

$$- \frac{\varepsilon_{i,j,k-1/2}}{\Delta z^2} v_{i,j,k-1} - \frac{\varepsilon_{i,j,k+1/2}}{\Delta z^2} v_{i,j,k+1} = f_{ijk}, \quad (\text{B.7})$$

where $\varepsilon_{ijk} = \varepsilon(x_i, y_j, z_k)$, $\varepsilon_{i+1/2,j,k} = \varepsilon(x_i + \Delta x/2, y_j, z_k)$, $\lambda_{ijk} = \lambda(x_i, y_j, z_k)$, $f_{ijk} = f(x_i, y_j, z_k)$.

References

- [1] D.K. Ferry, S.M. Goodnick, and J. Bird, *Transport in nanostructures*, Cambridge University Press, (2009).
- [2] K. Barnham and D. Vvedensky, *Low-dimensional semiconductor structures*, Cambridge University Press, (2001)
- [3] P. Harrison, *Quantum Wells, Wires and Dots*, Wiley, (2005)
- [4] C. Jacoboni, *Theory of Electron Transport in Semiconductors*, Springer, (2010).
- [5] M. Lundstrom, *Fundamentals of Carrier Transport*, Cambridge University Press, (2000)
- [6] A. Jünger, *Transport Equations for Semiconductors*, Lecture Notes in Physics No. 773. Springer, Berlin, (2009)
- [7] K. Tomizawa, *Numerical Simulation of Submicron Semiconductor Devices*, Artech House, Boston-London, (1993)
- [8] S. Selberherr, *Analysis and Simulation of Semiconductor Devices*, Springer, (1984).
- [9] C. Jacoboni and L. Reggiani, *The Monte Carlo method for the solution of charge transport in semiconductors with applications to covalent materials*, Rev. Mod. Phys., 55 , 645-705, (1983).
- [10] K. Nehari, N. Cavassilas, J.L. Autran, M. Bescond , D. Munteanu , and M. Lannoo, *Influence of band structure on electron ballistic transport in silicon nanowire MOSFETs: An atomistic study*, Solid-State Electronics 50, 716-721, (2006).
- [11] Y. Zheng, C. Rivas, R. Lake, K. Alam, T. B. Boykin, and G. Klimeck, *Electronic Properties of Silicon Nanowires*, IEEE TRANSACTIONS ON ELECTRON DEVICES, 52(6), 1097-1103, (2005).

- [12] J. Wang, A. Rahman, A. Ghosh, G. Klimeck, and M. Lundstrom, *On the Validity of the Parabolic Effective-Mass Approximation for the IV Calculation of Silicon Nanowire Transistors*, IEEE TRANSACTIONS ON ELECTRON DEVICES, 52(7), 1589-1595, (2005).
- [13] N. Neophytou, A. Paul, M. S. Lundstrom, and G. Klimeck, *Bandstructure Effects in Silicon Nanowire Electron Transport*, IEEE TRANSACTIONS ON ELECTRON DEVICES, 55(6), 1286-1297, (2008).
- [14] N. Neophytou, and H. Kosina, *Atomistic simulations of low-field mobility in Si nanowires: Influence of confinement and orientation*, PHYSICAL REVIEW B 84, 085313, (2011).
- [15] E. Gnani, S. Reggiani, A. Gnudi, P. Parruccini, R. Colle, M. Rudan, and G. Baccarani, *Band-Structure Effects in Ultrascaled Silicon Nanowires*, IEEE TRANSACTIONS ON ELECTRON DEVICES, 54(9), 2243-2254, (2007).
- [16] S. Jin, M.V. Fischetti and T.-W. Tang, *Modeling of electron mobility in gated silicon nanowires at room temperature: Surface roughness scattering, dielectric screening, and band nonparabolicity*, JOURNAL OF APPLIED PHYSICS 102, 083715, (2007).
- [17] Y. Suzuki and K. Varga, *Stochastic Variational Approach to Quantum-Mechanical Few Body Problems*, Springer, (1998).
- [18] D. Potter, *Computational Physics*, Wiley, (1972).
- [19] D. Vasileska and S.M. Goodnick, *Computational Electronics*, Morgan & Claypool Publishers, (2006).
- [20] J. Wang, E. Polizzi, M. Lundstrom, *A three-dimensional quantum simulation of silicon nanowire transistors with the effective mass approximation*, J. Appl. Phys. 96(4), 2192-2203, (2004).
- [21] P. Markowich, C.A. Ringhofer, C. Schmeiser, *Semiconductor Equations*, Springer, Wien, (1990).
- [22] S. Jin, T.-W. Tang, M.V. Fischetti, *Simulation of silicon nanowire transistors using Boltzmann Transport equation under the Relaxation time approximation*, IEEE Trans. Electron Devices 55(3), 727-736, (2008).
- [23] J. Wang, M. Lundstrom, *Does source-to-drain tunneling limit the ultimate scaling of MOSFETs?*, IEDM Tech. Dig., San Francisco, CA, pp. 707-710 (2002).

- [24] E.B. Ramayya, D. Vasileska, S.M. Goodnick, and I. Knezevic, *Electron mobility in silicon nanowires*, IEEE Trans. Nanotech., vol. 6, no. 1, pp. 113–117 (2007).
- [25] E.B. Ramayya and I. Knezevic, *Self-consistent Poisson-Schrödinger-Monte Carlo solver: electron mobility in silicon nanowires*, J. Comput. Electr., vol. 9, pp. 206–210 (2010).
- [26] E.B. Ramayya, D. Vasileska, S. Goodnick, and I. Knezevic, *Electron transport in silicon nanowires: The role of acoustic phonon confinement and surface roughness scattering*, J. Appl. Phys., vol. 104, p. 063711 (2008).
- [27] M.L. Lenzi, P. Palestri, E. Gnani, A. Gnudi, D. Esseni, L. Selmi, and G. Baccarani, *Investigation of the transport properties of silicon nanowires using deterministic and Monte Carlo approaches to the solution of the Boltzmann transport equation*, IEEE Trans. Electr. Dev., vol. 55, no. 8, pp. 2086–2096 (2008).
- [28] R. Kotlyar, B. Obradovic, P. Matagne, M. Stettler and M. D. Giles, *Assessment of room-temperature phonon-limited mobility in gated silicon nanowires*, Appl. Phys. Lett. 84, 5270, (2004).
- [29] G. Ossig and F. Schürerer, *Simulation of non-equilibrium electron transport in silicon quantum wires*, J. Comput. Electron., vol. 7, pp. 367–370 (2008).
- [30] T. Grasser, T.-W. Tang, H. Kosina, S. Selberherr, *A review of hydrodynamic and energy-transport models for semiconductor device simulation*, Proc. IEEE 91(2), 251-273, (2003).
- [31] D. Jou, J. Casas-Vázquez, G. Lebon, *Extended irreversible thermodynamics*, Springer-Verlag, Berlin, (2001).
- [32] G. Lebon, D. Jou, J. Casas-Vázquez, *Understanding Non-equilibrium Thermodynamics*, Springer-Verlag, Berlin, (2008).
- [33] I. Müller, T. Ruggeri, *Rational Extended thermodynamics*, Springer-Verlag, Berlin, (1998).
- [34] V.D. Camiola, G. Mascali, V. Romano, *Numerical simulation of a double-gate MOS-FET with a subband model for semiconductors based on the maximum entropy principle*, Cont. Mech. Therm., 24(4), 417-436, (2012).

- [35] V.D. Camiola, G. Mascali, V. Romano, *Simulation of a double-gate MOSFET by a non-parabolic energy-transport subband model for semiconductors based on the maximum entropy principle*, Math. Comp. Mod., 58(1), 321-343, (2013).
- [36] O. Muscato, R.M. Pidotella, M.V. Fischetti, *Monte Carlo and hydrodynamic simulation of a one dimensional $n^+ - n - n^+$ silicon diode*, VLSI DESIGN, 6, 247-250, (1998).
- [37] A.M. Anile, O. Muscato, V. Romano, *Moment equations with Maximum Entropy closure for carrier transport in semiconductor devices: validation in bulk silicon*, VLSI DESIGN, 10, 335-354, (2000).
- [38] O. Muscato, V. Di Stefano, *Local equilibrium and off-equilibrium thermoelectric effects in silicon semiconductors*, J. Appl. Phys., 110(9), 093706, (2011).
- [39] V. Di Stefano, O. Muscato, *Seebeck Effect in Silicon Semiconductors*, Acta Appl Math., 122(1), 225-238, (2012)
- [40] O. Muscato V. Di Stefano, *An Energy Transport Model describing heat generation and conduction in silicon semiconductors*, J. Stat. Phys., 144, 171-197, (2011).
- [41] O. Muscato, V. Di Stefano, *Hydrodynamic modeling of the electro-thermal transport in silicon semiconductors*, J. Phys. A:Math. Theor., 44, 105501, (2011).
- [42] O. Muscato, V. Di Stefano, *Electrothermal transport in silicon carbide semiconductors via a hydrodynamic model*, SIAM J. APPL. MATH., 75(4), 1941-1964, (2015).
- [43] G. Mascali, *A hydrodynamic model for silicon semiconductors including crystal heating*, Eur. J. Appl. Math., 26(4), 477-496, (2015).
- [44] O. Muscato and V. Di Stefano, *Hydrodynamic modeling of silicon quantum wires*, J. Comput. Electron., vol. 11, no. 1, pp. 45-55 (2012).
- [45] O. Muscato and V. Di Stefano, *Hydrodynamic simulation of a $n^+ - n - n^+$ silicon nanowire*, Contin. Mech. Thermodyn., vol. 26, pp. 197-205 (2014).
- [46] O. Muscato and V. Di Stefano, *Coupled quantum-classical transport in silicon nanowires*, Computational Methods for Coupled Problems in Science and Engineering, pp. 1109-1119, Barcelona: CIMNE (2013).
- [47] T. Kuykendall, P. Pauzauskie, S. Lee, Y. Zhang, J. Goldberger, and P. Yang, *Metallorganic chemical vapor deposition route to GaN nanowires with triangular cross sections*, Nano Letters, vol. 3, no. 8, pp. 1063-1066 (2003).

- [48] G. Liang, W. Huang, C. S. Koong, J.-S. Wang, and J. Lan, *Geometry effects on thermoelectric properties of silicon nanowires based on electronic band structures*, J. Appl. Phys., vol. 107, p. 014317, (2010).
- [49] R. Khordad and H. Bahramiyan, *Electron-phonon interaction effect on the energy levels and diamagnetic susceptibility of quantum wires: Parallelogram and triangle cross section*, J. Appl. Phys., vol. 115, p. 124314, (2014).
- [50] G. Pennelli and M. Piotto, *Fabrication and characterization of silicon nanowires with triangular cross section*, J. Appl. Phys., vol. 100, p. 054507 (2006).
- [51] G. Pennelli, *Top down fabrication of long silicon nanowire devices by means of lateral oxidation*, Microelec. Engineer., vol. 86, pp. 2139–2143 (2009).
- [52] O. Muscato, T. Castiglione, C. Cavallaro, *Ballistic charge transport in a triple-gate silicon nanowire transistor*. In: B. Schrefler, E. Onate and M. Papadrakakis, Computational Methods for Coupled Problems in Science and Engineering, pp. 666-676, Barcelona: CIMNE (International Center for numerical Methods), ISBN: 978-84-943928-3-2, Venice, Italy, May 18-20, (2015).
- [53] O. Muscato and T. Castiglione, *Electron transport in silicon nanowires having different cross-sections*, Comm. Appl. Industr. Math., 7(2), 8-25, (2016).
- [54] T. Castiglione and O. Muscato, *Non-parabolic band hydrodynamic model for silicon quantum wires*, to appear in J. Computat. Theor. Transport., (2016).
- [55] A.M. Anile, V. Romano, *Nonparabolic band transport in semiconductors: closure of the moment equations*, Contin.Mech. Thermodyn. **11**, 307–325 (1999)
- [56] V. Romano, *Non parabolic band transport in semiconductors: closure of the production terms in the moment equations*, Contin.Mech. Thermodyn. **12**, 31–51 (2000)
- [57] G. Mascali and V. Romano, *A non parabolic hydrodynamical subband model for semiconductors based on the maximum entropy principle*, Math. Comp. Model., vol. 55, no. 3-4, pp. 1003-1020, (2012).
- [58] W.-K. Li and S. Blinder, *Solution of the Schrödinger equation for a particle in an equilateral triangle*, J. Math. Phys., vol. 26, no. 11, pp. 2784–2786 (1985).
- [59] E. T. Jaynes, *Information theory and Statistical Mechanics*, Phys. Rev. 106, 620 (1957).

- [60] N. Wu, *The Maximum Entropy Method*, Springer, Berlin, (1997)
- [61] A. Trellakis, A.T.Galik, A. Pacelli, U. Ravaioli, *Iteration scheme for the solution of the two-dimensional Schrödinger-Poisson equations in quantum structures*, J. Appl. Phys., 81(12), 7880-7884 (1997).
- [62] Y. Yamada, H. Tsuchiya, M. Ogawa, *Quantum transport simulation of silicon-nanowire transistors based on direct solution approach of the Wigner transport equation*, IEEE Transactions on electron devices, vol.56, no.7, (2009).
- [63] G. Fiori, G. Iannaccone, *Three-Dimensional Simulation of One-Dimensional Transport in Silicon Nanowire Transistors*, IEEE Transactions on nanotechnology, vol. 6, no.5, (2007).
- [64] N. Singh, A. Agarwal, L.K. Bera, T.Y. Liow, R. Yang, S.C. Rustagi, C.H. Tung, R. Kumar, G.Q. Lo, N. Balasubramanian, D.-L. Kwong, *High-performance fully depleted silicon nanowire (diameter ≤ 5 nm) gate-all-around CMOS devices*, IEEE Electron Device Lett. , 27(5), 383-386, (2006).
- [65] Y. Guerfi, G. Larrieu, *Vertical Silicon Nanowire Field Effect Transistors with Nanoscale Gate-All-Around*, *Nanoscale Res. Lett.*, 11, 210, (2016).
- [66] A. Lochtefeld and D.A. Antoniadis, *On Experimental Determination of Carrier Velocity in Deeply Scaled NMOS: How Close to the Thermal Limit?*, IEEE ELEC. DEV. LETTERS 22(2): 95-97, (2001).
- [67] K. Natori, *Ballistic metal-oxide-semiconductor field effect transistor*, J. Appl. Phys. 76(8):4879-4890, (1994).
- [68] O. Muscato, T. Castiglione, *A hydrodynamic model for silicon nanowires based on the maximum entropy principle*, submitted to Entropy.
- [69] O. Muscato, T. Castiglione, A. Coco, *Low-field electron mobility in silicon nanowires*, submitted proceedings ECMI, (2016).
- [70] O. Muscato, T. Castiglione, A. Coco *Hydrodynamic modeling of electron transport in gated Silicon Nanowire Transistors*, submitted in Atti Accademia Peloritana dei Pericolanti, (2016).
- [71] F. Karimi, M. Fathipour, H. Ghanatian and V. Fathipour, *A Comparison Study of Electrical Characteristics in Conventional Multiple-gate Silicon Nanowire Transistors*, Int. Journal Electrical. and Comm. Engineer., 4(9), (2010).